POLYMER DERIVED CERAMICS: PROCESSING

–STRUCTURE–PROPERTY RELATIONSHIPS

By

SURAJ C. ZUNJARRAO

Bachelor of Engineering in Mechanical Engineering
University of Pune
Pune, Maharashtra, India
2001

Master of Science in Mechanical Engineering
State University of New York at Stony Brook
Stony Brook, NY, USA
2005

Submitted to the Faculty of the
Graduate College of
Oklahoma State University
in partial fulfillment of
the requirements for
the Degree of
DOCTOR OF PHILOSOPHY
May, 2008

POLYMER DERIVED CERAMICS: PROCESSING –STRUCTURE–PROPERTY RELATIONSHIPS

Dissertation Approved:

Dr. Raman P. Singh
_____
Dissertation Advisor

Dr. Hongbing Lu
_____

Dr. Jay Hanan
_____

Dr. Jim Puckette
_____

Dr. A. Gordon Emslie
_____
Dean of the Graduate College

ACKNOWLEDGMENTS

As I sit down to write this page, I am filled with a great sense of gratitude towards so many who have made this journey possible, but above all, towards my advisor Prof. Raman P. Singh, for taking me under his wing and guiding me with such kindness throughout my life as a graduate student. He has been an incredible mentor and his superlative expertise in this field of research has kept me firmly rooted on the right track. Dr. Singh's clarity of thought, ability to see the big picture and optimism has pulled me out of despair so many times, when I saw no light at the end of the tunnel. He kept faith in me and provided encouragement as I stumbled during those early stages of PhD qualifiers, and I am immensely grateful for that. All these years, it has been a delight to stop by his office for a chit-chat on anything from current events in the science and politics to computer games and movies. His humility, attitude of fairness, believing in and extracting the best out of others and yearning for giving back to the society are truly inspiring.

I wish to thank Dr. Jay Hanan, Dr. Hongbing Lu, Dr. Jim Smay and Dr. Jim Puckette for being on my dissertation committee. Special thanks to Dr. Puckette for filling in for Dr. Jim Smay at such a short notice. I am sure Dr. Puckette will remember me as the MAE student annoyingly showing up at his office door every other day to enquire about the XRD machine. I am thankful for his kindness and tolerance. During the course of my work, I found myself seeking Dr. Hanan's help every time I was stuck analyzing my XRD data and I am thankful for his willingness to help every time. I am very thankful to Dr. Hongbing Lu for his guidance in the finite element modeling work. Discussions with him helped me avoid going astray in

TABLE OF CONTENTS

LIST OF TABLES

CHAPTER 1

Introduction

1.1 Processing of Ceramics

1.1.1 Powder Sintering

To this day, traditional, powder–processing based methods continue to be the most common ways for preparing ceramic materials. The several steps typically involved in conventional powder processing route are outlined in figure 1.1 [1]. These steps include powder preparation, powder processing, powder consolidation, and sintering.

The first step in conventional powder processing of ceramics is the preparation of the basic feed-stock powders. While chemical processing procedures are most common and well established for oxide materials, most non-oxide materials are made by carbothermal reduction. For example, the formation of silicon carbide (SiC), by the Acheson process, is achieved by mixing and reacting a mixture of silicon dioxide (SiO_2) and carbon (C), along with a small amount of sawdust and common salt, at temperatures up to $2700\,°C$ at atmospheric pressure. In this context, liquid chemical approaches are being explored so as to have a better control over the particle sizes [2]. Other approaches of powder preparation involve sol-gel techniques, especially for preparing oxides [3, 4] and vapor phase processing for producing powders and whiskers [5, 6].

Powder processing is an important second step in fabricating ceramics by powder–processing routes. This typically involves the adjustment of particle size, mixing of ceramic constituents, and improving handleability. It is desired to have relatively fine
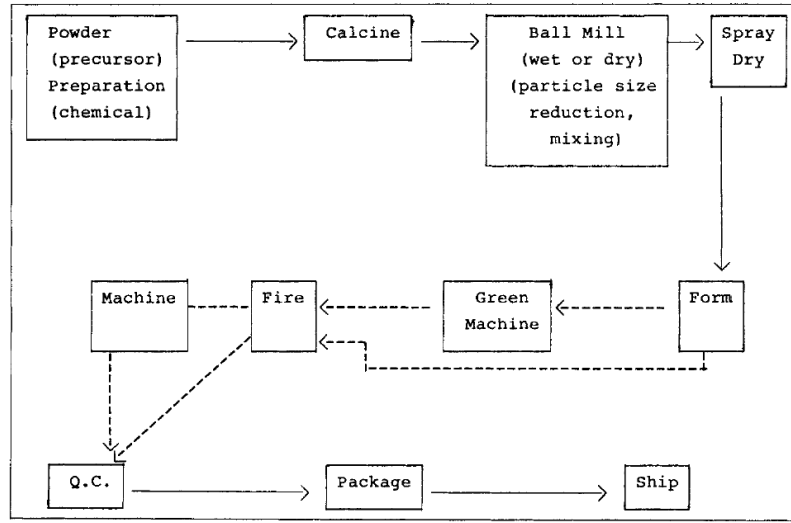
Figure 1.1: Steps typically involved in making ceramics using conventional powder processing route. [1].

particle sizes to achieve good sinterablility and at the same time form agglomerates that will improve integrity for handling and forming [1].

Once the constituent powders have been prepared and processed, the next step is to consolidate these powders into a shaped 'green' body. For powder consolidation the commonly used techniques are tape casting, slip casting, pressure casting, and isostatic pressing. Tape casting is typically used for making thin components such as substrates and capacitors used for electronic ceramic applications. Isostatic pressing is more common for smaller to intermediate part sizes and less complex shapes. Compression and injection molding can also be used for powder consolidation. In this method, a mixture of a polymer carrier and the ceramic powder of interest is forced into a mold cavity. The use of substantial amount of polymer is required to achieve the plasticity desired from the mixture and this limits the ceramic green density. Furthermore, severe defects in the parts could result from inhomogenous mixing of the polymer–ceramic powder slurry. The 'green body' thus formed at the end of the powder consolidation phase is often machined to obtain greater intricacy of shape and to get more accurate dimensioning.

2

The final processing step involves organic burnout, firing, and sintering of the consolidated green body to form the final, fully dense ceramic. Burnout of organic constituents is preferably achieved by thermal processes, also termed as binder burnout. A homogenous burnout is desirable to avoid distortion and cracking. Finally, during firing and sintering of the ceramics, the powders are caused to coalesce into a near-theoretically dense body due to surface tension forces. This requires heating the compacts to very high temperatures, as much as two-third of the absolute melting temperature, as in the case of solid-state sintering.

Sintering is the final step and and plays a central role in determining the final microstructure and dimensional tolerance of the ceramic component. Challenges toward achieving good sintering involve the ability to accommodate for the shrinkage during densification. Failure to shrink uniformly could result in cracking in parts. In general, oxide ceramics sinter more readily as compared to nonoxide ceramics. Therefore, in the latter case, sintering aids are commonly used to enhance solid-state sintering and also retard grain growth. In fact, commonly used ceramics such and silicon carbide (SiC) and silicon nitride (Si_3N_4) cannot be sintered without additives. Use of sintering aids such as C, B, Y_2O_3, Al_2O_3 and MgO, which help in achieving higher densities is quite common in fabrication of ceramics through powder processing routes.

The type and amount of sintering aids used have a strong influence on the final material properties. These sintering aids are necessary to reduce surface tension, required for achieving near-theoretical densities and for limiting grain growth. On the other hand, these additives often segregate at grain boundaries in the form of a 'glassy' layer. The presence of this amorphous layer can severely impair mechanical properties, especially at high temperatures. Minimizing the addition of sintering aids can then lead to significant improvement in properties such as high-temperature creep resistance. Nonetheless, the fabrication of materials without sintering aids, such as stoichiometric, ultra-high purity SiC, is extremely challenging with traditional powder

processing techniques. Finally, it should be noted that despite of their well-known importance and widespread use, the identification of sintering aids has been mostly empirical, and often accidental.

The use of high pressure and/or high temperature processing is a basic requirement for traditional powder–based fabrication of ceramic components. These processing conditions not only increase the energetic requirements but also places limits on the types of materials that can be produced. For example, SiC fibers degrade at temperatures above 1200 °C [7]. Therefore, the fabrication of SiC-fiber–reinforced ceramic matrix composites is extremely difficult using conventional power-based processing.

1.1.2 Reaction Processing

Reaction processing is an important alternative to sintering and is widely used to make silicon carbide [8]. This method involves a liquid-solid reaction process for the synthesis of the ceramic compound, and offers the capability to fabricate refractory ceramics at lower cost compared to conventional sintering. There are different methods that can be categorized as reaction processing based on the intrinsic rate of reaction, as illustrated in figure 1.2 [9].
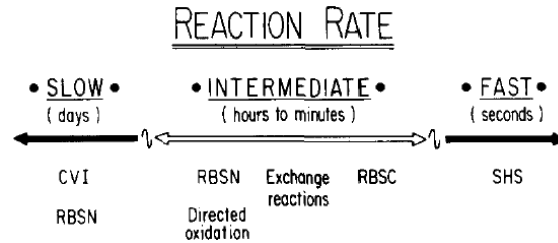
Figure 1.2: Different methods categorized as reaction processing along with their relative rate of reaction. [9].

The control of the reaction rate is a key issue in reaction processing. While chemical vapor infiltration (CVI) is at the slow end of the spectrum with typical processing rate of several hundred hours, self-propagating high temperature synthesis

(SHS) reactions are the fastest but place limitations on size and complexity. The methods that are in the intermediate range offer fast yet controllable reaction forming.

In reaction bonded processing of silicon carbide, a 'green body' preform of silicon carbide and carbon is infiltrated with molten silicon at temperatures of about 1450 °– 1650 °C. The result is a reaction bonded SiC (RBSC) mainly consisting of SiC with 5–15 % vol. residual Si. Reaction process of SiC is a low cost technique and produces minimal shrinkage during the infiltration process. Therefore this technique allows for near net shape manufacturing of intricate components, and also allows the fabrication of very large parts that are ~1 m in dimension. This method, first developed in 1960 by Popper [10], is being widely used today for commercial fabrication of ceramics. Engineers at General Electric Company [11,12] used this method to fabricate SiC fiber composites with a silicon matrix by reacting molten Si with a carbon fiber preform. In addition, this process has also been extended to other ceramics, and particularly to ceramic composites such as Si_3N_4– SiC composites and B_4C–SiC–Si–C composites.

Reaction bonded SiC finds extensive use in general high-temperature and creep applications, wear resistant parts, ceramic armor, and components required to withstand thermal shock. However, the presence of residual, free silicon limits the maximum use temperature to below 1400 °C. Furthermore, this free silicon can also limit the corrosion and oxidation resistance as compared to stoichiometric silicon carbide.

1.1.3 Non-powder–based Processing

In the last two decades, there has been considerable research interest in the development of alternative, powder-free, chemical methods for the preparation of ceramics. Non-powder based ceramic processing and coating methods that have been developed include melt casting, chemical vapor deposition, sol–gel processing, and polymer pyrolysis [13]. The development of these ceramic fabrication techniques has been driven by several factors such as homogenous dispersion of phases, denser ceramics, incor-

poration of fillers such as fibers and whiskers, etc.

For melt casting, arc melting using graphite electrodes is often employed and parts are usually cast in graphite molds. Melt casting generally yields much larger grains and more porosity as compared to sintering. Further, grain sizes are nonuniform during different cooling rates on surface and interiors.

Chemical vapor deposition (CVD) involves the deposition of a solid material on to an activated or heated surface by reaction with a gaseous phase. Besides being used for making ceramic coatings, CVD can also be used to produce ceramic powders and free standing parts [14]. Usually, inorganic precursors in form of halides and metal carbonyls are used as a source of vapor [15–17]. Advantages of the CVD technique include lower costs, good densification, and the fabrication of ceramics without additives [1]. Control over the processing temperature is critical for CVD as this regulates the process thermodynamics and kinetics [18]. Challenges in CVD include gas phase nucleation and homogenous reaction occurring due to supersaturation of the reactive species in the gaseous phase. Also control of microstructure and residual stresses is a matter of concern in the CVD process. The resulting microstructure can have substantial grain sizes; large grains result in weaker mechanical properties.

A variant of CVD is the chemical vapor infiltration (CVI) process. In CVI, inorganic vapors are used to infiltrate porous structures or preforms where they deposit, react, and form part of the composite. It is a very effective technique for forming composites such as fiber reinforced ceramics and other unique structures that are difficult or impossible to fabricate by using CVD alone. Chemical vapor infiltration is widely used for fabrication of silicon carbide matrix composites reinforced by continuous silicon carbide fibers. However, the CVI processing is usually very slow due to low diffusion rates.

Sol–gel processing involves precipitation of ceramic particles from aqueous media. The precursors are in form of inorganic salts or metal alkoxide solutions that

are processed to form hydrous metal oxides or hydroxides. The sol-gel method is generally confined to hydrolysable metal-ion species that produce aqueous sols, such as SiO_2, Al_2O_3, ZrO_2, TiO_2, CeO_2, etc [19]. Advantages of the sol-gel technique are lowering sintering temperature, lower energy cost and higher purity of resulting material. Although more commonly used for making ceramic coatings, this technique can produce bulk pieces of limited sizes [20, 21]. This technique can also be adapted to produce ceramic composites by dispersion of powders, fibers or whiskers as reinforcement phase into sols [22, 23]. However, control over porosity and low densities are the major challenges for the sol-gel technique.

1.1.4 Polymers Derived Ceramics

Another non–powder based method of preparing ceramics, and which is potentially promising, is pyrolysis based processing of polymer–derived ceramics. This method is considerably simple and involves condensation of organometallic compounds into inorgranic materials by proper thermal treatment under controlled atmosphere.

Polymer precursors (also known as preceramic polymers) are organo–element polymers that undergo a polymer–to–ceramic conversion when heated at temperatures above $800\,°C$. They generally contain silicon, and in some cases boron, and are typically used to obtain non–oxide ceramics such as SiC, SiNC, Si_3N_4, and BN [24]. Preceramic polymers can be envisioned as long chain molecules with the chain composed of main–group inorganic elements and with organic branches. Upon heating to a sufficient temperature, the organic branches are shed, leaving behind an amorphous network of inorganic elements which crystallizes on further heating [25]. A typical flow diagram of the overall process of formation of polymer–derived ceramics is shown in figure 1.3 [26].

Fabrication of ceramics by pyrolysis of preceramic polymers has several clear advantages. Preceramic polymers can be processed and shaped using conventional poly-
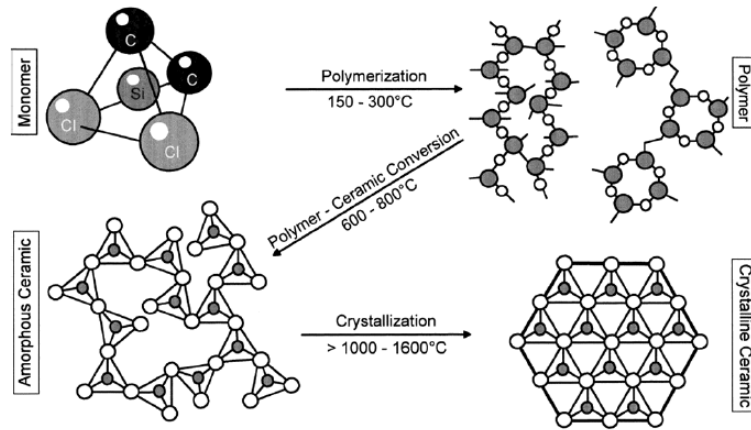
Figure 1.3: Schematic representation of molecular and microstructural transitions during ceramic manufacturing from preceramic polymers. [26].

mer forming techniques such as polymer infiltration and pyrolysis (PIP), injection molding, coating from solvent, extrusion, or resin transfer molding (RTM) [27]. This allows for fabrication of highly three–dimensional covalent refractory components (fibers, films, membranes, foams monolithic bodies, ceramic matrix composites) that are difficult to fabricate via the traditional powder–processing route [28], and also allows for the incorporation of reinforcements. Fabrication by pyrolysis also provides the ease of processibility familiar to polymer and sol–gel science and relatively low processing temperatures (<1200 °C) [29–31]. Lowered processing temperatures reduce the incidence of fiber damage in reinforced ceramic matrix composites, and as a result the pyrolysis route has been touted as being suitable for fabrication of continuous fiber–reinforced ceramic composites (CFCCs) [32]. In this manner polymer precursor processing can offer several of the advantages for carbide- or nitride-based ceramics that are found for oxide-based ceramics fabricated using sol-gel processing.

Typically, the ceramic yield is much higher in polymer derived processing as compared to other non-powder chemical routes. In some cases, ceramic yield as high as 85% has been reported [33]. Nonetheless, the main challenge of polymer precursor based methods is the increase in density observed upon conversion from the polymer

8

(mass density of ∼1 g/cc) to ceramic (mass density of ∼3 g/cc). This results in volumetric shrinkage, which coupled with <100 % ceramic yield, leads to the formation of porosity in the form of open pores and cracks. Accordingly, several polymer infiltration and pyrolysis (PIP) cycles are required to densify the ceramic component.

1.2   Silicon Carbide

The focus of this investigation is on silicon carbide (SiC) for application in nuclear reactor based advanced energy systems. This is one the most commonly used ceramics owing to its excellent properties such as high strength, modulus, and creep resistance [34], and retention of properties at high temperatures. Silicon carbide resists oxidation upto a high temperature of about 1600 °C has a very high disassociation temperature of 2830 °C [35]. Silicon carbide also exhibits a very high hardness of 32 GPa [36]. It has excellent thermal conductivity, 31 W/m °C, and a very low coefficient of thermal expansion, $4.7 \times 10^{-6}/$ °C at 1200 °C [36]. These properties are summarized for sintered alpha-SiC by Munro [36].

Silicon carbide's superior characteristics as a structural material from the viewpoint of its thermal shock resistance, chemical stability, and low radioactivation have attracted attention to its potential use in advanced energy systems [37–39]. In a study of the effect of cyclic thermal shock on candidate nuclear matrix materials, Lee *et al.* [39] observed no change in the hardness and even an increased fracture toughness for SiC as compared to the other ceramics that were considered. SiC has also attracted a lot of attention for applications in joining of ceramic parts for both nuclear and non-nuclear applications [38,40]. Joining of parts using polymer pyrolysis derived SiC was found to provide considerable strength in SiC composites [40].

High temperature and irradiation effects on swelling and mechanical properties of silicon carbide have been evaluated by several researchers [38, 41, 42]. In general it has been found that the best performance is for silicon carbide that is of high-purity,

9

stoichiometric composition, and has a crystalline microstructure [37, 41–46]. For example, Hinoki *et al.* [37] observed excellent high temperature irradiation resistance for high purity SiC/SiC composites. These properties make SiC a promising candidate for use in nuclear applications in structural parts as well as an inert matrix for ceramic based fuel elements.

For the successful application of silicon carbide based materials to nuclear applications, the fabrication process needs to satisfy several requirements. Firstly, the fabrication process must allow control over microstructure and material purity to ensure mechanical performance under high temperature and irradiation environments. Secondly, the processing technique should allow for facile incorporation of reinforcements and net shape manufacturing. Finally, a non-powder based method would be preferable for handling of highly pyrophoric/radiotoxic materials that could be used for nuclear applications [47]. The polymer infiltration and pyrolysis route to precursor derived ceramics satisfies these and has added advantages of low temperature and pressure-less processing.

1.3   Nanocrystalline Ceramics

Polymer pyrolysis based processing allows for a greater control over the reaction kinetics and microstructure evolution that can be tailored to yield a amorphous/nanocrystalline ceramic material [48–50]. Such nano-crystalline ceramics are the focus of intense research as they have the potential for unique properties such as "super hardness" and significantly high toughness [51–54].

Nanocrystalline SiC has being pursued for its mechanical properties, and also for its superior electrical and optical properties [55]. Vassen *et al.* [56] reported hardness of up to 27 GPa for bulk–sintered SiC materials with grain sizes as small as 70 nm. Tymiak *et al.* [57] have reported hardness value of about 37 GPa with grain sizes around 20 nm, for SiC films deposited by hypersonic plasma particle deposition.

Recently, Liao *et al.* [54] have reported hardness as high as 50 GPa for nanocrystalline SiC films with grain sizes of 10–20 nm, deposited by thermal plasma CVD.

The superior properties of nanocrystalline ceramics are governed primarily by the crystal structure [52, 54, 58]. There have been attempts to simulate the atomic structure and understand the materials properties of PDCs at fundamental level by modeling and computational studies [59–62], but these studies have not addressed the unique properties that are sometimes observed in these materials. Besides the effect of grain size, other factors, such as the presence of hydrogen as in the case of SiC, can also contribute to the hardness [60]. Currently, the effect of grain size on the mechanical properties of nanocrystalline ceramics is not as well characterized or understood as that for metals.

Considerable work, experimental as well as computational, has been done to characterize hardness in nanocrystalline metals. It was first observed by Hall [63] and Petch [64] that the crystal size in metals had a direct effect on their mechanical properties. Around the year 1951–53, Hall and Petch, while working at the Cavendish Laboratory in Cambridge, United Kingdom, independently came up with the same empirical relationship describing the effect of grain size on the yield strength of metals. This relationship is given by equation 1.1 [63, 64] and is famously known as the "Hall–Petch equation".

$$\sigma_y = \sigma_0 + \frac{K}{\sqrt{d}} \tag{1.1}$$

where, σ_y is the yield stress, d is the mean grain size, and K and σ_0 are constants; σ_0 being the starting stress for dislocation movement.

The increase in yield strength with decreasing grain size, as predicted by equation 1.1, is attributed to the presence of grain boundaries, which act as barriers to the motion of dislocations. The smaller the grain size, the greater the pile-up of dislocations at grain boundaries, and thus greater the barrier to deformation. In this manner, decreased grain size leads to an increase in the yield strength or the hardness.

Hall's and Petch's observations and the Hall–Petch equation have been experimentally corroborated several times over [65]. However, when the grain sizes decreases below a certain value, the strength and hardness start to degrease. This phenomenon is termed as the 'reverse' Hall–Petch effect and the first experimental evidence of this was observed by Chokshi *et al.* [66] for copper and palladium nanocrystals. Later this phenomena was subjected to several computational [67,68] as well as experimental [69–72] investigations.

Mechanisms proposed for the reverse Hall–Petch effect include increased porosity, suppression of dislocation pile–up, dislocation motion through multiple grains and sliding in grain boundaries [73]. It is now speculated that there exists a characteristic grain size, where a crossover occurs from Hall–Petch to reverse Hall–Petch as the grain size becomes smaller and smaller [74].

In contrast to metals, a fundamental mechanistic understanding of hardness in nano-crystalline ceramics is lacking. Veprek *et al.* [75] attempted to explain superior properties of nanocrystalline ceramics based on conventional fracture mechanics. They ascribe the extremely high values of fracture toughness observed to a low concentration of flaws. Liao *et al.* [54] experimentally investigated hardness, crystal size, and crystallinity as a function of the substrate temperature for nanocrystalline β–SiC films deposited by thermal plasma chemical vapor decomposition, and observed increase in all three, with increase in the substrate temperature. Recently, Szlufarska *et al.* [51] studied atomistic processes occurring during nanoindentation of amorphous silicon carbide (a–SiC) by molecular dynamic simulations and found onset of plasticity at different indentation depths. They observed that load drops occurred during the simulated indentation of a–SiC, similar to the case of single crystal SiC. According to the authors, their observations point towards a crossover from inter-granular continuous deformation to intra-granular discrete deformation which is governed by indentation depth.

Since polymer-derived ceramics allow for the fabrication of microstructures with significant control over the grain size, they offer an ideal system for understanding the effect of crystallinity on the yield strength and other mechanical properties. There have been recent efforts to characterize the overall structure of polymer–derved ceramics by means of molecular dynamic simulations [59, 61, 76–78]. Kroll [59] studied the structure, energy and bulk modulus of amorphous silicon nitride and its ternary derivatives using molecular dynamic (MD) simulations and found that hydrogen plays a vital role in the kinetic and thermodynamic stability of these materials. Modulus was found to scale with the density. Atomic models by Amkreutz *et al.* [61] predict phase separation to occur between amorphous phases of SiC, Si_3N_4 and carbon which is also observed experimentally. These MD simulations focus mainly on understanding the structure of polymer derived ceramics at the atomic scale and investigate the mechanical properties as influenced by atomistic phenomena. These models do not consider mesoscale phenomena that seem to govern the bulk mechanical properties that can, and are being, experimentally investigated.

1.4   Objective of this Investigation

The focus of this work is to characterize and understand the processing–structure–property relationships of polymer precursor derived silicon carbide. This particular investigation is part of an ongoing study to develop precursor derived SiC for application in advanced energy systems such as nuclear reactors.

Ceramics derived from preceramic polymers are a fast growing class of advanced materials due to the various advantages they offer, such as low processing temperatures, near net shape fabrication, and high ceramic yield. Owing to this, they are being researched for varied applications from disc brakes to nuclear reactor fuels. Furthermore, nanocrystalline ceramics can be prepared from polymer precursor routes with relative ease. Nanocrystalline ceramics are touted to be the key to new super

hard and ultra stiff materials. Since the microstructure is one of the more important factors governing the properties, appropriate tailoring can lead to significant improvement in various properties. Significant work has focused on the improved properties of nanocrystalline metals; however, in the realm of ceramics, most of the existing research has looked only at ceramics formed by conventional sintering techniques or, among new techniques, by chemical vapor deposition. Thus there is a need to characterize the nanocrystalline ceramics derived from polymer precursors.

Of the several non-oxide ceramics, those based on SiC, Si_3N_4 or general Si/C/N systems are of particular interest since their exceptional structural stability at very high temperatures, and low density, makes them ideal materials for application in adverse environments. Pioneering work in the development of polymer precursor for Si/C/N materials was done by Verbeek [79, 80] and Yajima *et al.* [81]. Out of the aforementioned ceramics, SiC is of particular interest because it has proven to be a promising candidate for use in nuclear applications owing to its low radioactivation [37, 82].

Various polycarbosilanes are available for use as precursors to prepare silicon carbide. This research has focussed on one such precursor, allylhydridopolycarbosilane (AHPCS), due to its purity, commercial availability, and the ability to yield near-stoichiometric silicon carbide. There is very limited data in literature on mechanical characterization of nanocrystalline SiC derived from AHPCS, especially as a function of the microstructure. Therefore, this study focusses on three aspects. First, silicon carbide processing is conducted under controlled conditions by the pyrolysis of AHPCS under an inert atmosphere and at ambient pressure. The processing itself is characterized in detail by tracking the chemical changes, phase transformations, and microstructural changes that are occurring as a function of the pyrolysis conditions. Subsequently, the mechanical property characterization of AHPCS–derived SiC, in terms of hardness and modulus, is carried out using instrumented nanoindentation, to

access the local properties and establish the processing–property–structure relationships. The results of mechanical testing are understood in terms of the microstructure (characterized using X-ray diffraction and transmission electron microscopy), for materials processed under different conditions. Finally, the results are analyzed using simple computational models to understand the role of grain size and crystal volume fraction on the mechanical properties.

CHAPTER 2

Background and Literature Survey

2.1   Processing of preceramic polymer

The processing of polymer–derived ceramics begins with the preparation of suitable monomers, consequently, a lot of research has focused on development of these. Over the past few decades, a variety of preceramic organosilicon polymers have been developed as precursors to ceramics with a wide range of compositions in the Si–B–C–N–O system, and in addition also yield metallic constituents, such as Ti, Al and Zr [27,83,84]. Considerable research has focused especially on preparation of precursors to SiC, Si_3N_4, and Si/C/N–based materials, since their exceptional structural stability at very high temperatures makes them ideal thermomechanical materials. Pioneering work in the development of polymer precursor for Si/C/N materials was done by Verbeek [79,80] and Yajima *et al.* [81]. The latter also intensively investigated the modern utilization of preceramic polymers to yield mainly SiC; his approach to synthesis of SiC materials by thermolysis of polycarbosilane is commonly known as 'The Yajima Process'.

Yajima *et al.*'s work stirred up the interest in synthesis of polycarbosilanes and since then a number of different ways to prepare polycarbosilanes have been devised [85–87]. Birot *et al.* [88] have provided an excellent and comprehensive account of polycarbosilanes, polysilazanes and polycarbosilazanes as precursors to SiC, Si_3N_4 and Si/C/N materials. Figure 2.1 shows examples of the polymers that have been synthesized for the preparation of silicon carbide and silicon nitride–based ceramics [89]. By far, the most common approaches for synthesizing SiC by polymer precursor route
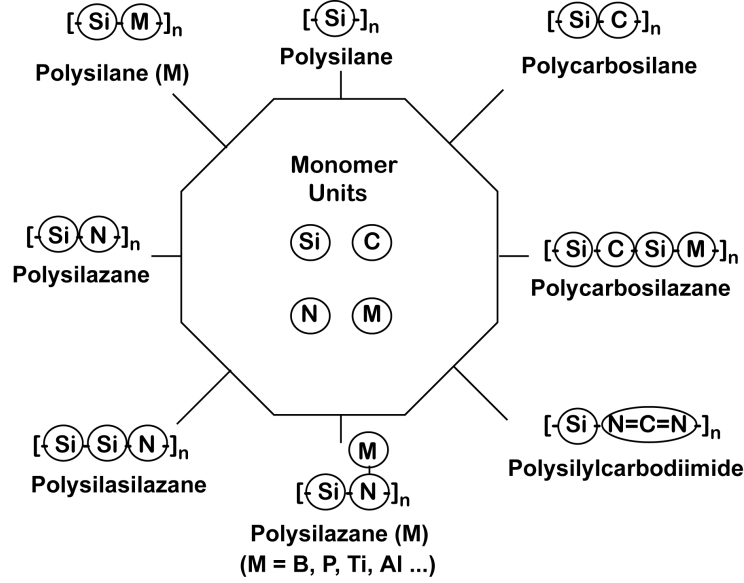
Figure 2.1: Examples of the polymers as precursors to Si-C-N based ceramics [89].

are through polysilanes, polycarbosilanes and polysilazanes, which are basically polymeric organosilanes with Si, Si–C and Si–C–N polymer backbones, respectively.

Perhaps the first attempt at synthesizing of polymeric silicon molecules was exhibited by Kipping [90] in, as early as, the year 1924. He successfully synthesized polydiorganylsilane, which had a polymeric backbone comprised entirely of silicon atoms. Later in 1949, Burkhard [91] synthesized poly(dimethylsilane), the first alkyl–substituted polysilane. Some examples of polymers, other than polycarbosilane, demonstrated as precursors to SiC, are poly(methylsilane) [92], polymetalloxoorganosiloxanes [93], poly(silaethylene) [87], polysilastyrene [94], and poly(cyclomethylsilazane) [95].

2.2   Allylhydridopolycarbosilane (AHPCS), as a precursor for SiC

The high temperature ceramic of particular interest to this study is silicon carbide. And, of the several available SiC polymer precursors, allylhydridopolycarbosilane (AHPCS) is the polymer of our choice for the current study. It is an ultra high purity precursor that yields a near stoichiometric ratio on complete pyrolysis [96]. Its high
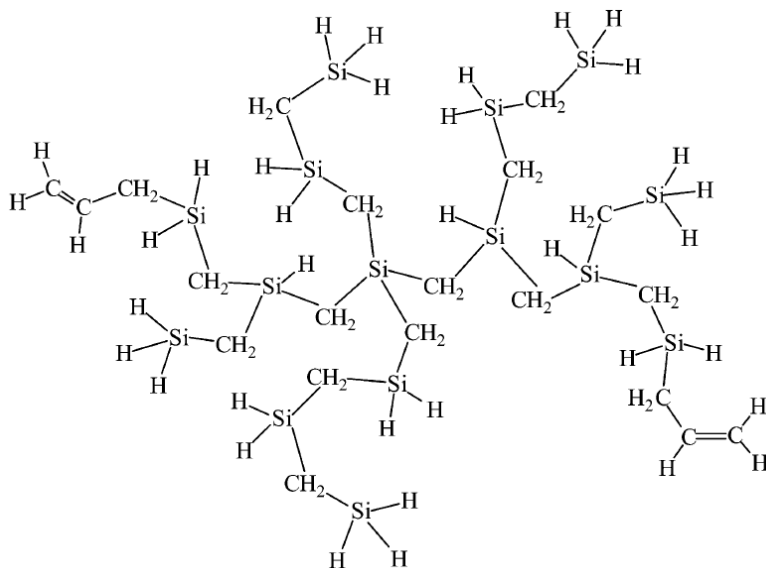
Figure 2.2: Diagrammatic representation of AHPCS structure [103].

ceramic yield, relatively low shrinkage, and ability to be handled and processed in ambient conditions have attracted wide attention, especially as precursor to SiC fibers and more recently as a matrix material [97–100].

Whitmarsh *et al.* [86, 101] first reported the synthesis of allylhydridopolycarbosilane (AHPCS) by Grignard coupling of (chloromethyl)trichlorosilane, followed by reduction with lithium aluminum hydride. AHPCS has a nominal structure of $[Si(CH_2CH=CH_2)_2CH_2]_{0.1}[SiH_2CH_2]_{0.9}$ [86, 100–102], diagrammatically described as show in figure 2.2 [103]. Thus it has a Si:C ratio that is close to 1:1 and yields a near stoichiometric SiC upon pyrolysis. AHPCS is commercially available through Starfire Systems Co. (Malta, New York, USA) and is being widely researched as a binder for ceramic powders and matrix source for polymer–derived ceramic matrix composites [96, 97, 99]. It has also been used to produce SiC coatings and join monolithic and composite ceramic parts [40, 104]. Furthermore, Solomon *et al.* [105] have used AHPCS in developing a light water reactor (LWR) fuel by impregnation of uranium oxide matrix with AHPCS as a SiC precursor. Previously, Singh and coworkers have researched ceramic foams based on AHPCS–derived SiC and hollow alumino–silicate

spheres [106], and currently are pursuing AHPCS–derived SiC as a potential matrix material for the fabrication of ceramic composite fuels for gas cooled fast reactors (GCFR) [107] .

2.2.1 Mechanical properties of AHPCS derived SiC

It is evident that AHPCS is gaining great interest for potential use in wide ranging, technologically advanced, and, in some instances, critical applications. However, not much mechanical-property data is available for AHPCS-derived SiC. Ceramics derived from preceramic polymers are often prone to develop cracks and porosity, especially at higher processing temperatures, due to volume shrinkage and evolution of hydrogen gas during pyrolysis [40, 97, 100, 104]. Such inherent porosity influences the bulk properties of these composites and the measurement of "true" or mesoscale properties becomes difficult by bulk measurement techniques. Since AHPCS is largely used as a source of SiC matrix in SiC/SiC composites, its fracture toughness is particularly important. Fracture toughness of the matrix would have a significant effect on the fracture toughness of the overall composite since the cracks could initiate and propagate in the ceramic matrix which will inherently contain pores. Another property of great interest when it comes to AHPCS-derived SiC is the hardness. For applications such as ceramic brakes, the hardness would determine the wear rate.

There are very limited measurements of mechanical properties of SiC derived from any polymer precursor, perhaps partly due to the difficulty in fabricating monolithic specimens. Bulk characterization of AHPCS–derived SiC sample, prepared by PIP process, has reported by Mores *et al.* [100]. The materials were characterized in terms of density (by immersion method), fracture toughness (by bulk V–notched beam method) and hardness (by bulk Vickers indentation test). The highest values for fracture toughness and hardness were found to be about 167 MPa.m$^{1/2}$ and 13 GPa, respectively. Porosity was found to adversely affect the properties. Thus, there

arises the need to characterize the properties of these materials in the monolithic domain. In this context, nanoindentation, which is widely used to characterize the mechanical properties at the nano–scale [108], is particularly helpful in determining the true or mesoscale properties of ceramics that have inherent micropores. In a recent study, Liao *et al.* [54] successfully used nanoindentation to determine hardness of superhard SiC films deposited by thermal plasma chemical vapor deposition. They found that a higher hydrogen flow rate during the deposition process resulted in greater crystallinity, bigger crystals sizes (27 nm) and lower hardness (30 GPa). Conversely, at lower hydrogen flow rates, the crystalline fractions and grain sizes were smaller and the hardness was higher. With an average grain size of 10–20 nm and crystalline fractions of 80-85% they got film hardness of up to 50 GPa.

Processing parameters such as temperature and time have a direct bearing on the microstructure of ceramic formed. For example, silicon carbide formed from polymer precursor generally exhibits an amorphous structure at 1000 °C and is crystalline beyond 1600 °C. The mechanical properties can be expected to vary greatly between these processing temperatures. Hence, information on how the mechanical properties change with processing parameters will be of great value, and aid not only in design of parts using these ceramics but also in optimization of processing parameters and constituents (in composites) to fabricate materials with desired mechanical properties.

2.2.2 Microstructure Characterization of AHPCS–derived SiC

Material microstructure largely governs the final properties of ceramics, and hence microstructure characterization, as well as the study of nucleation and crystallization, are vital for understanding structure–property relationships. While very limited literature, if any, exists on microstructural characterization of AHPCS–derived SiC there is some data on Si–C systems derived from other chemical methods. Mitchell *et al.* [50] examined the nucleation and crystallization process in Si–C and Si–N–C

systems produced by the pyrolysis of granulated polymethylsilane and found that processing temperature and time both influence the crystal size. Nanocrystalline β–SiC derived from chlorine containing polysilanes/polycarbosilane prepared from poly(chloromethylsilane–co–styrene) was characterized by DTA, TGA, XRD, TEM, mass spectroscopy and infrared spectroscopy, by Mitchell *et al.* [50]. Grain sizes were calculated to be 5–20 nm. Nechanicky *et al.* [109] reported TGA, FTIR, TEM and XRD studies on alpha–SiC/beta–SiC particulate reinforced composites prepared by PIP using a hyper–branched polymethylsilane (mPMS). Kerdiles *et al.* [110] used FTIR and HREM to study nano–crystalline SiC thin films grown by reactive magnetron co–sputtering of SiC and C targets. Zhang *et al.* [111] characterized crystal structure of nanocrystalline SiC by TEM, and Raman Spectroscopy in SiC thin films deposited by a plasma–enhanced CVD process. Ying *et al.* [112] used XRD, TEM and SAED to study the microstructure of nanocrystalline SiC prepared by reacting magnesium silicide (Mg_2Si) and carbon tetra fluoride (CCl_4) in an autoclave and reported crystal sizes of 30–80 nm.

Work of characterizing the crystal structure of AHPCS derived SiC and probing its structure–property relations as a function of processing parameters is required as it will help in fundamental understanding of these materials, and is necessary for the use of AHPCS derived SiC as an effective matrix material or for joining applications.

2.2.3   Structure–Property relationships for AHPCS derived SiC

Currently AHPCS is preferred more as a matrix source for SiC-fiber/SiC-matix or particulate-SiC composites than as a source of monolithic unreinforced SiC components. Perhaps this is the reason why reports of property-structure characterization are limited to AHPCS derived composites. While characterizing C/SiC composites fabricated by infiltrating a woven carbon fiber fabric with a slurry of SiC powder and AHPCS, Berbon *et al.* [97] found improved thermal conductivity and diffusivity with

crystallization in the polymer derived phase. Dong *et al.* [98] studied microstructural evolution and mechanical performance of SiC/SiC composites fabricated by polymer infiltration process (PIP). They used AHPCS derived SiC as a matrix along with uncoated and carbon coated Tyranno SA fibers and pyrolysis was performed using microwave radiations. Mechanical strength results showed improved flexural strength, with a strong dependence on the quality of matrix–fiber interface. Zheng *et al.* [104] examined the thermal decomposition behavior of AHPCS (Nippon Carbon Co, Tokyo, Japan) while developing a method of joining SiC ceramics in green state without applied pressure. Using XRD, they observed the formation of amorphous SiC (a–SiC) at about 850 °C, which completely crystallized at 1600 °C. A mixture of SiC particles and AHPCS, used as a joining paste was found to produce good crack–free joints. Kotani *et al.* [113] studied the effect of filler dispersion on the mechanical properties of unidirectional composites with SiC fibers and SiC matrix prepared using PIP technique. The polymer precursors they investigated included polyvinylsilane (PVS) and polycarbosilane (PCS). In another study involving AHPCS, Lewinsohn *et al.* [40] found that, when using AHPCS derived SiC in joining SiC composites, higher processing temperatures increased the strength of joints, possibly due to extensive crystallization. But there is still a need to realize the processing–microstructure–property–application relationships for this organic polycarbosilane which will aid in the characterization of composites derived from AHPCS.

CHAPTER 3

Experimental Procedure

The preceramic polymer precursor chosen for this study is allylhydridopolycarbosilane (AHPCS). Selection of this particular preceramic polymer is favored due to the fact that it is an ultra high purity precursor, yields a near stoichiometric Si:C ratio on complete pyrolysis, has a high ceramic yield, exhibits relatively low shrinkage, and is widely used as precursor to SiC fibers. The polymer, designated as SMP–10, is acquired from Starfire Systems (Malta, New York, USA). At room temperature, it is in the form of a clear, amber-colored, viscous liquid and has properties as listed in table 3.1. The polymer was stored under $0\,^{\circ}\text{C}$ at all times and handled at room temperature. All processing during pyrolysis was done under an inert atmosphere, as specified.

According to Starfire Systems product data sheet on SMP-10, the polymer undergoes a low temperature curing to form a green body between 180 and $400\,^{\circ}\text{C}$ and forms a fully ceramic amorphous SiC between 850 to $1200\,^{\circ}\text{C}$ with 80-82% ceramic yield.

3.1 Material Fabrication

3.1.1 Preliminary Experiments and Setup

One of the main advantages of precursor polymer route to ceramics is the ease of fabrication. Preparing SiC from AHPCS simply requires heating the polymer to temperature of above $900\,^{\circ}\text{C}$ in a oxygen free atmosphere. When the precursor is heated from room temperature, cross–linking starts at about $100\,^{\circ}\text{C}$ and a cured green body

Property	SMP–10 (AHPCS)
Density	0.998
Appearance	Clear, Amber liquid
Viscosity	45 to 120 cps at 25 °C
Solubility	Hexanes, Toulene, Insoluble in water
Flash Point	89 °C (192 °F)
Moisture Absorbtion	< 0.1% in 24 hrs at room temperature
Nominal Cure Temperature	250 to 400 °F
Surface Tension	30 dynes/sq.cm

Table 3.1: Properties of STARFIRE SMP–10 as obtained from Starfire Systems Co., Malta, New York, USA .

is formed. To track the polymer–to–ceramic conversion as a function of temperature, carefully weighed quantities of liquid AHPCS were heated, under argon atmosphere, from room temperature up to 300°, 500°, 700°, and 900 °C, respectively. Samples were held at final temperatures for 30 min to ensure thermal equilibrium. Figure 3.1 shows the setup of the box furnace, fitted with a retort and modified for inert gas pyrolysis up to 900 °C. Pyrolysis beyond 900 °C was performed in a specially modified high temperature furnace (Model no. F46248, Barnstead International, Dubuque, Iowa, USA). During the initial stages of heating, cross–linking in the polymer is accompanied by loss of volatile components in the precursor which were observed to form yellowish–white deposits on the inner walls of the furnace up to about 700 °C. Hence, the heating was controlled at the slow rate of 5 °C/min, for samples heated up to 700 °C, to ensure minimal loss of polymer due to volatilization prior to cross–linking. There is no fear of losing the volatile components beyond this temperature and hence higher heating rates can be safely employed beyond 700 °C. Small quantities of amorphous SiC derived from AHPCS pyrolyzed at 900 °C were loaded in
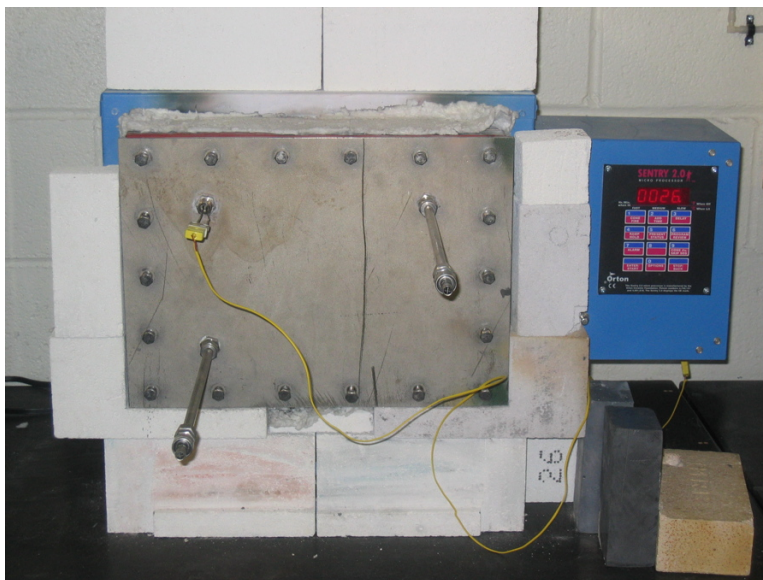
Figure 3.1: Setup used for inert gas pyrolysis up to 900 °C

alumina crucibles and heated to different temperatures of 1150°, 1400° and 1650 °C starting from room temperature at 5 °C/min and held at final temperature for 30 min, in the high temperature oven under a constant flow of argon.

Since moving to Oklahoma State University in July 2006, a new setup consisting of argon purged tube furnace was configured as shown in figure 3.2. At the inlet, ultra high purity argon gas is passed through a combination of moisture and oxygen traps to ensure zero-oxidation due to impurities that may be present in the tanked gas. Also, steel tubing is used at the inlet to avoid contamination by air diffusion into the tubes. After initial runs of the tube furnace with the polymer precursor yielding slightly oxidized silicon carbide, traps were set up for purifying the argon gas fed to the tube furnace. The traps used were a high capacity gas purification system (Agilent Technologies) that consisted of three cartridges: one cartridge removing moisture and organics, second cartridge removing oxygen and third indicator cartridge to warn of system saturation; and an indicating moisture removal trap. The setup of these traps is shown in figure 3.3.
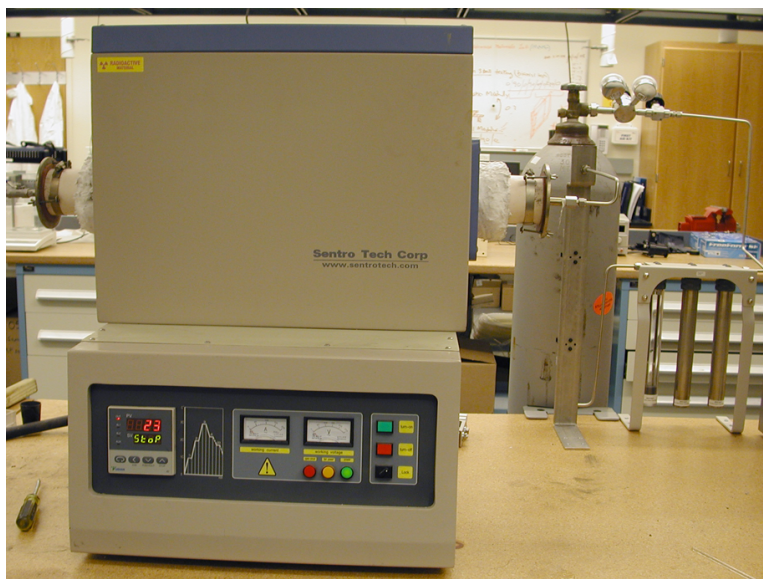
Figure 3.2: New tube furnace setup used for inert gas pyrolysis up to 1650 °C

Figure 3.3: Setup of traps to purify argon fed to the tube furnace. These include: a cartridge removing moisture and organics, a cartridge removing oxygen and a third indicator cartridge to warn of system saturation. Finally there is an indicating moisture removal trap.

3.1.2 Effect of Processing Parameters

To study the effect of processing parameters on the structure of SiC formed and its mechanical properties, SiC samples were made by pyrolysis of precursor, starting with the liquid form, heated to $900\,^\circ$, $1150\,^\circ$, $1400\,^\circ$, and $1650\,^\circ$C in a single runs at $4\,^\circ$C/min. To study the effect of holding the material at the final temperature for different durations, the aforementioned materials being processed were held at the final temperatures (i.e. $900\,^\circ$, $1150\,^\circ$, $1400\,^\circ$, and $1650\,^\circ$C) for time durations of 2 minutes, 60 minutes, and 4 hours in different experiments. The resulting material was in the form of chunks of SiC. Samples for nanoindentation were prepared by embedding part of the chunk in epoxy, which was then polished. Samples for x-ray diffraction and TEM were prepared by crushing part of the chunk; by hand using mortar and pestle for XRD, and using a ball-mill for TEM.

3.1.3 Fabrication for Bulk Testing

Other than mesoscale characterization using nanoindentation, bulk characterization was done using ring-on-ring (ROR) biaxial flexure test. Due to the severe shrinkage in the precursor during transition from polymer liquid to ceramic SiC, fabricating a bulk sample purely of SiC derived from AHPCS is a tricky and lengthy process. The use of reinforcing agents in the form of SiC powders, fibers or whiskers, which is common in the use of AHPCS, greatly helps since it substitutes a considerable volume of the composites with these fillers that do not change in volume significantly. Thus the shrinkage occurs only in the matrix phase which is formed by pyrolysis of the precursor. Since the aim of this investigation is to characterize the SiC derived from AHPCS alone, use of reinforcing agents such as SiC fibers or whiskers was avoided. However, a similar fabrication approach of polymer infiltration and pyrolysis (PIP) used for fabrication polymer derived ceramic composites was adopted.

First, SiC powder was prepared by pyrolysis of AHPCS to $900\,^\circ$, $1150\,^\circ$, $1400\,^\circ$, and

1650 °C in a single runs at 4 °C/min. The samples were held at the final temperature for 60 minutes to ensure thermal equilibrium. The resulting material acquired the shape of the crucible and contained large voids generated by the release of hydrogen gas. These were crushed into powder using a planetary ball mill (PM-100, Retsch GmbH, Haan, Germany) in a tungsten carbide bowl (WC) with 10 mm WC balls for 12 min at 300 rpm. These powders in turn form the reinforcing fillers in the next step of fabricating composites using PIP process. Thus by using SiC powder derived from AHPCS, we could make bulk samples made of SiC purely derived from AHPCS alone.

The powders obtained from the initial pyrolysis of the precursor were then mixed with a small amounts of polymer precursor (3% by weight of the milled powder). These mixtures were compacted into short cylinders, 25.4×15 mm, using a simple steel ram-cylinder setup. Thin discs cut from a graphite sheet (Grafoil) were used at the bottom and top of material being compressed. This prevented the material being compressed from sticking to the mold or the ram. Hand compaction with a load of $\sim$445 N ($\sim$100 lb) was sufficient to form plugs that could be easily handled. The resulting compacts were then heated to the final temperature (900°, 1150°, 1400°, or 1650 °C). The resulting samples had a good dispersion of SiC particles in a-SiC matrix. However, pores were present at this stage resulting from the release of hydrogen during the polymer pyrolysis. To minimize the pores and increase the material density, the samples were subjected to multiple polymer infiltration cycles. Figure 3.4 shows the schematics of the complete PIP processing used in the current study. The infiltration of the cylindrical plugs was carried out under vacuum, with repeated 1 hour cycles for 4 hours with intermediate 1 min purges. After the 3rd infiltration and pyrolysis cycle, the cylindrical specimens were cut to obtain discs of 1 mm thickness using a precision sectioning saw (Isomet 1000, Buehler, Lake Bluff, Illinois, USA). Further infiltration and pyrolysis, in the aforementioned way, was carried out on the discs up to a total of 8 cycles. Work by Ozcivici *et al.* [106] with polymer derived ceramic composites

using this polymer system has showed that 8 infiltration cycles are sufficient to obtain the maximum achievable density. These discs were tested for biaxial flexure modulus and strength using ring-on-ring test.

3.2 Physical Characterization

To determine the mass loss during polymer-to-ceramic conversion as a function of temperature, samples prepared, as described earlier by heating polymer precursor to temperature of $300\,°$, $500\,°$, $700\,°$, $900\,°$, $1150\,°$, $1400\,°$, and $1650\,°$C, were carefully weighed before and after pyrolysis. All weights were measured using a high-resolution analytical balance (Model BP-301S, Sartorius, Edgewood, NY). Bulk density and porosity of the ceramic composite discs fabricated by PIP process using AHPCS-derived SiC powder and AHPCS-SiC matrix were determined using the buoyancy method [114] using a density determination kit in conjunction with the high-resolution analytical balance. First the specimen was dried in a drying oven at $120\,°$C until it reached a constant mass and then cooled to room temperate in a desiccator. The dry mass of the sample, m_1, was recorded. The sample was then evacuated and saturated (under vacuum) using ultra high purity distilled water until the open pores were filled with the saturation liquid. A four-hour evacuation cycle was employed with intermittent purges at every thirty minutes to release trapped air. The apparent mass of the saturated sample, m_2, was then determined using the density determination kit. The temperature of the saturation liquid was also recorded to correct for the variation of the density of water, as a function of temperature. Finally, the mass of the saturated sample was determined by weighing in air, m_3. Before weighing any liquid that remained on the surface of the sample was removed with a damp sponge and the operation was performed quickly, to avoid loss of mass due to evaporation.The density of the saturation liquid (water), ρ_{fl} was taken from a given table of density
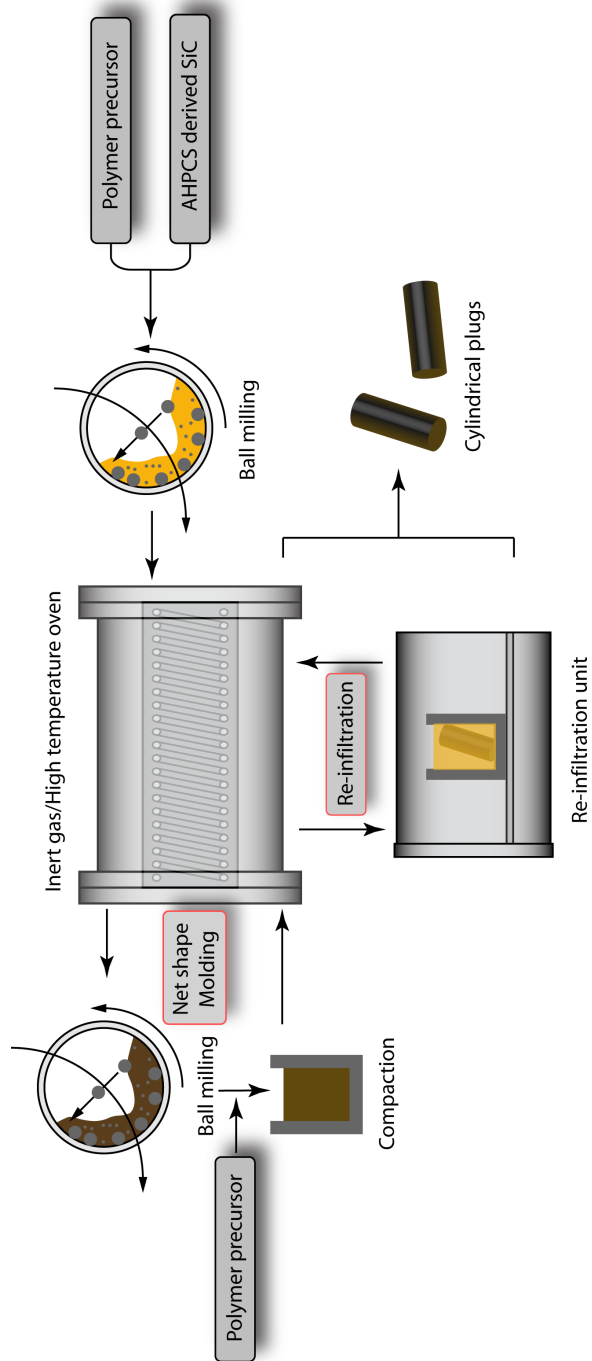
Figure 3.4: Schematic of PIP process for fabrication of bulk samples for bulk charac-terization

values at defined temperatures, and the bulk density, ρ_b, was determined by,

$$\rho_b = \frac{m_1}{m_3 - m_2} \times \rho_{fl} \tag{3.1}$$

where, m_1 is the dry mass of the sample, m_2 is the mass of the saturated sample in water, m_3 is the mass of the saturated sample in air and ρ_{fl} is density of the medium used (water) at the measuring temperature. The open porosity, π_a, in vol. % was calculated as,

$$\pi_a = \frac{m_3 - m_1}{m_3 - m_2} \times 100 \tag{3.2}$$

Density measurements were also performed on finely crushed powders of SiC derived from AHPCS heated to $300\,°$, $500\,°$, $700\,°$, $900\,°$, $1150\,°$, $1400\,°$, and $1650\,°$ using helium pycnometry (Ultrapycnometer 1000, Quantachrome, Boynton Beach, FL). Powders were dried for 23 h at $60\,°C$ in a drying oven prior to these measurements. This method yields mesoscale density of inherently porous materials, which cannot be accessed by bulk density measurements.

Fourier transform infrared spectroscopy (FTIR) analysis performed on polymer precursor material heated from room temperature to final temperatures of $300\,°$, $500\,°$, $700\,°$, $900\,°$, $1150\,°$, $1400\,°$, and $1650\,°$ using a Nicolet Model Magna 760 FTIR spectrometer with ZnSe ATR crystal with $4\mathrm{cm}^{-1}$ resolution and average over 256 scans. The crushed powders were used as-is and analyzed in a microscope using reflectance mode. These measurements were performed with the help of Environmental Nanotechnology Research Group directed by Dr. Gary P. Halada in the department of Materials Science and Engineering at Stony Brook University.

Simultaneous differential thermal analysis (DTA) and thermogravimetric analysis (TGA) was performed to study the conversion of amorphous SiC to nanocrystalline SiC. A small amount of SiC derived from polymer precursor pyrolyzed at $900\,°C$ was heated to $1300\,°C$ at a rate of $5\,°C/min$ under nitrogen atmosphere (STA 449 C Jupiter, NETZSCH, Selb/Bavaria, Germany). These measurements were done at

the Center for Thermal Spray Research, in the department of Materials Science and Engineering at Stony Brook University, NY, directed by Dr. Sanjay Sampath.

X–ray diffraction studies were also performed on SiC powders pyrolyzed at 900 °, 1150 °, 1400 °, and 1650 °C. Powder samples were prepared by wet milling in a planetary ball mill (PM–100, Retsch GmbH, Haan, Germany) for 4h in ethanol and then mounted on glass slide. Powder diffraction patterns were collected using Scintag PAD–X automated diffractometer with a CuK_α radiation ($\lambda = 0.1540$ nm) using a scanning rate of 0.5 ° per min and operating at 45 kV and 25 mA.

To characterize the microstructure of SiC formed at different processing temperatures, transmission electron microscopy (TEM) was performed on powders crushed using a ball-mill as described before. TEM studies were performed using a JEOL JEM-2100 Scanning Transmission Electron Microscope System equipped with an EDAX Genesis 2000 EDS system. TEM studies were performed with the help of Dr. Susheng Tan at the Oklahoma State University Microscopy Laboratory.

3.3 Mechanical Characterization

Chunks of SiC material from the pyrolysis products, at different processing temperature and different hold times, were mounted in epoxy (Epoxicure, Buehler, Lake Bluff, Illinois, USA) and polished to a mirror finish using Ecomet 3 polisher (Buehler, USA). Samples were then indented using a sharp Berkovich diamond indenter (NanoIndenter XP, MTS, Oak Ridge, TN) to a peak load of 10, 25, 50 and 100 mN for each material. A total of 10 indentations were performed for every sample. Nanoindentation was performed in the Polymer Mechanics Lab, which is directed by Dr. Hongbing Lu, in the Mechanical and Aerospace Engineering department at Oklahoma State University.

Bulk mechanical characterization was done using ring-on-ring (RoR) biaxial tests. The RoR is an axisymmetric test, where the disc is supported by a ring and loaded

from the opposite side by another smaller concentric ring, as shown in Fig. 3.5. The concentric rings were made up of stainless steel and had bullnose edges with a radius of 0.3125 mm towards the loading side. This configuration led to a support ring of ϕ19.05 mm and the loading ring as ϕ6.35 mm. The specimens were loaded in the
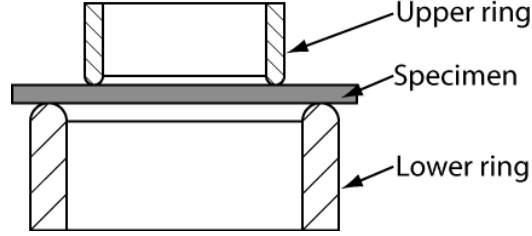
Figure 3.5: Schematic of fixture for testing biaxial flexure properties using RoR.

RoR fixture using a standard mechanical testing frame. In the area underneath the smaller ring there exists an equibiaxial tensile stress state where the initialization of fracture is expected. The flexure strength can then be determined from the peak load at failure Eqn. 3.3 as [115],

$$\sigma_{\text{RoR}} = \frac{3P}{2\pi t^2} \left[\frac{(1-\nu)(a^2 - r^2)}{2R^2} + (1+\nu)\ln\frac{a}{r} \right] \tag{3.3}$$

where ν is the Poisson ratio of the specimen and assumed to be 0.20 for SiC, a is the radius of the support ring, r is the radius of the load ring, and R and t are the radius and thickness of the disc specimen, respectively.

The RoR configuration is preferred over the other equibiaxial tests since it subjects a greater portion of the specimen to an equibiaxial stress state and distributes the applied contact load over a larger area. This lessens the applied stress concentration at the contact locations between the fixture and specimen and lowers the likelihood of fixture-induced specimen failure (invalid test data).

CHAPTER 4

Results and Discussion

4.1 Polymer–to–Ceramic Conversion

Fourier transform infrared spectroscopy (FTIR) analysis performed on polymer precursor material heated from room temperature to final temperatures of $300\,°$, $500\,°$, $700\,°$, $900\,°$, and $1150\,°C$, respectively, greatly aided the study of polymer to ceramic conversion. Figure 4.1 shows IR spectra obtained for products at different temperatures; data is offset to aid comparison. Peaks attributed to C–H (stretching), Si–H (stretching) and Si–C (rocking) bonds were clearly observed in the ranges of 2800–3000 cm^{-1}, 2000–2140 cm^{-1}, and 870–1070 cm^{-1} [96, 116, 117], respectively. It can be seen that the relative intensity of all the peaks initially increases with increasing temperature, which is a result of the increase in crosslink density as the polymer cures to form a network structure. A gradual shift in the Si–H peak towards lower wave numbers, with increasing temperatures, suggests conversion of silicon–hydrogen bonding from Si–H$_3$ to Si–H$_2$ to Si–H, as hydrogen is expelled from the system. The broad peak attributed to several C–H bonds reduces, and eventually disappears, along with the Si–H peak at $1150\,°C$ as hydrogen is completely removed. Small peaks resulting from the presence of mono–substituted alkenes in the polymer appear around 900 cm^{-1}(d) at $300\,°$ and $500\,°C$ and soon disappear at higher temperatures. Peaks attributed to CH$_3$ (bending) (a and b) and SiCH$_2$Si bonding (c) are also identified in the IR spectra. A small amount of hydrogen appears to be present in the system even at $900\,°C$, whereas at $1150\,°C$ the presence of only an SiC peak shows compete conversion of polymer into SiC.
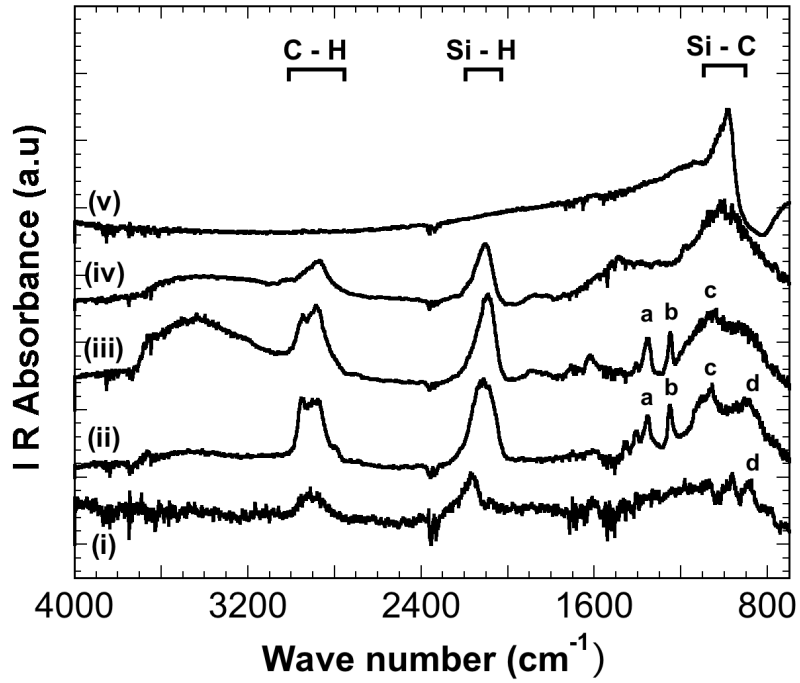
Figure 4.1: IR Spectra for AHPCS heated to 300 °C (i), 500 °C (ii), 700 °C (iii), 900 °C (iv) and 1150 °C (v).

Figure 4.2 shows the ceramic yield obtained as a function of decomposition temperature. The loss in weight is attributed to the loss of low–molecular weight oligomers and hydrogen gas [96]. It should be noted that in our case, volatilization driven mass loss was not limited even with very slow heating rates. Marginal loss in mass was observed beyond 700 °C and about 72–74% ceramic yield in the form of amorphous SiC was obtained in the range 900 °–1650 °C. In a separate study [118] on reaction kinetics during the pyrolysis of AHPCS, the polymer pyrolysis was characterized as a three–step process consisting of volatilization, cross–linking and crystallization; and activation energies for the volatilization and cross–linking were determined as 83.1 kJ/mol and 149.7 kJ/mol, respectively, using the mass loss data discussed above.

Conversion of the polymer precursor into ceramic material was also tracked in terms of density (shown in fig. 4.2 along with sample mass variation) of pyrolysis products at different stages of heating. Density measurements were performed using

35
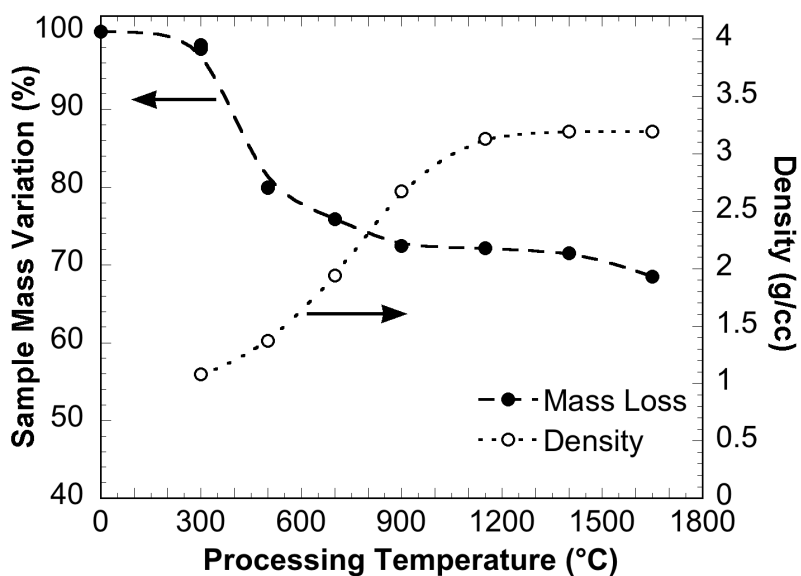
Figure 4.2: Mass loss and density variation as a function of temperature for AHPCS pyrolyzed to different temperatures.

helium pycnometry on finely crushed powders, dried for 2–3 h at 60 °C in a drying oven. This method yields true density of inherently porous materials, which cannot be accessed by bulk density measurements. Starting with a liquid AHPCS having a density of 0.997 g/cc (as mentioned by Starfire Systems Inc., USA), a dry and partially crosslinked solid with a density about 1.07 g/cc is obtained at 300 °C. Further heating results in more crosslinking accompanied by the loss of low molecular weight oligomers and release of hydrogen gas. As the processing temperatures increase further, density is observed to rise steadily until it reaches values that are close to the theoretical density for SiC at 1150 °C. It is worthwhile to note that SiC obtained at 900 °C exhibited a density of only 2.67 g/cc (as compared to 3.2 g/cc expected for sintered SiC), which could be due the presence of residual hydrogen as was observed during FTIR analysis.
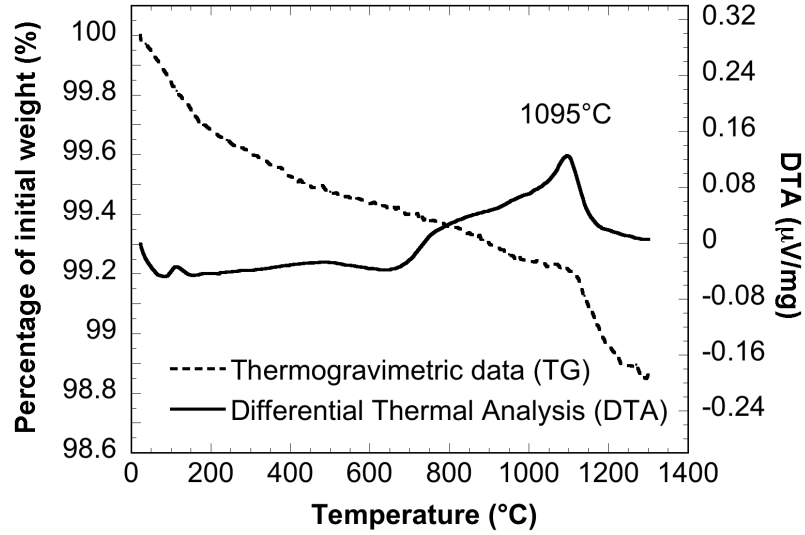
Figure 4.3: DTA and TG curves for AHPCS heated to 1300 °C at a rate of 5 °C/min.

4.2   Amorphous to Amorphous/Nano–crystalline Conversion

Evidence of crystallization in our SiC samples derived from AHPCS was first seen in differential thermal analysis (DTA) experiments. Figure 4.3 shows the DTA and TG curves obtained. A distinct peak is seen in the DTA curve around 1100 °C which is attributed to the initiation of crystallization in the material. The occurrence of this peak coincides with the change in slope in the TG curve. Further evidence of on–set of crystallization at this temperature was seen in the X–ray diffraction (XRD) and electron diffraction patterns obtained for the pyrolyzed products.

Figure 4.4 shows the XRD patterns obtained for various samples; data is offset to aid comparison. Amorphous SiC that was formed at 900 °C shows a greatly diffused peak whereas the peak intensity increases as the processing temperatures increase. Gradual growth of SiC peaks at 2θ values of 35.7 °, 60.2 ° and 72.0 ° suggests increasing ordering as nano–crystalline domains form and grow in amorphous SiC. It is noted that small peaks for residual tungsten carbide (WC), from the grinding media, are seen in the patterns. Also, even though a peak for WC lies very close to the SiC peak at 35.7 °, the prominent peaks at this 2θ are attributed to SiC since the WC peak

37
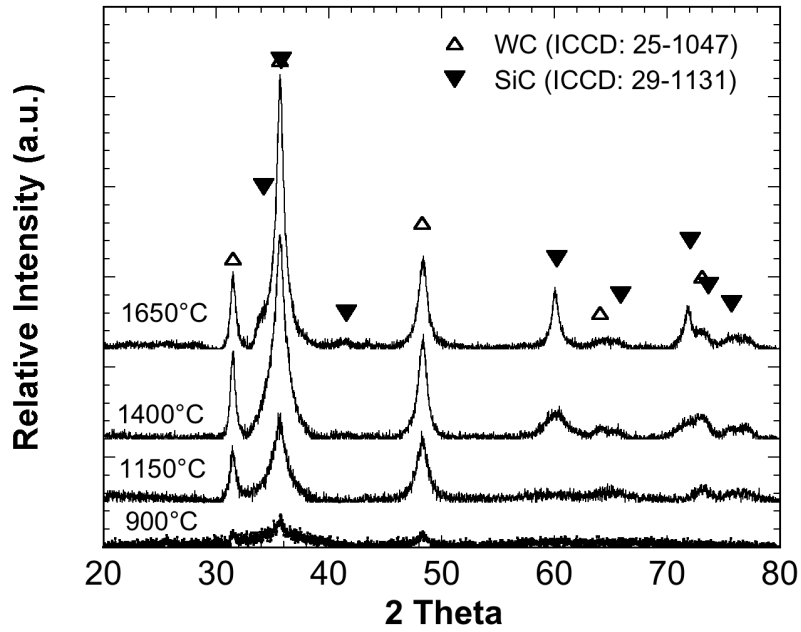
Figure 4.4: Powder diffraction patterns of SiC derived from AHPCS heated to 900°, 1150°, 1400° and 1650°C.

at 35.6° and 48.3° are expected to be of same intensity according to JCPDS (ICCD 29–1131). An estimate of the crystallite size was obtained from peak broadening using the Debye–Scherrer equation [119]. Peak broadening, in terms of full width at half–maximum (FHWM), was determined by fitting the obtained pattern using the XFIT program, which uses the pseudo Voigt (PV) and split Pearson (PVII) functions along with a fundamental parameters (FP) convolution approach [120]. Instrument broadening, determined by using NIST–traceable line–width standard LaB_6 sample (SRM 696), was accounted for, while determining the crystallite sizes at different temperatures. The crystallite sizes were found to be about 3.65 nm, 5.02 nm, and 11.03 nm at 1150°, 1400°, and 1650°C, respectively. Samples sent to a commercial laboratory (XRD.US) for determination of crystal sizes gave similar results of 3.83 nm, 6.50 nm and 11.07 nm for SiC fabricated at 1150°, 1400°, and 1650°, respectively. Figure 4.5 shows the powder diffraction plots obtained from XRD.US. The sharp peaks near 2 theta values of 28°, 47°, and 56° are from pure Si powder that was
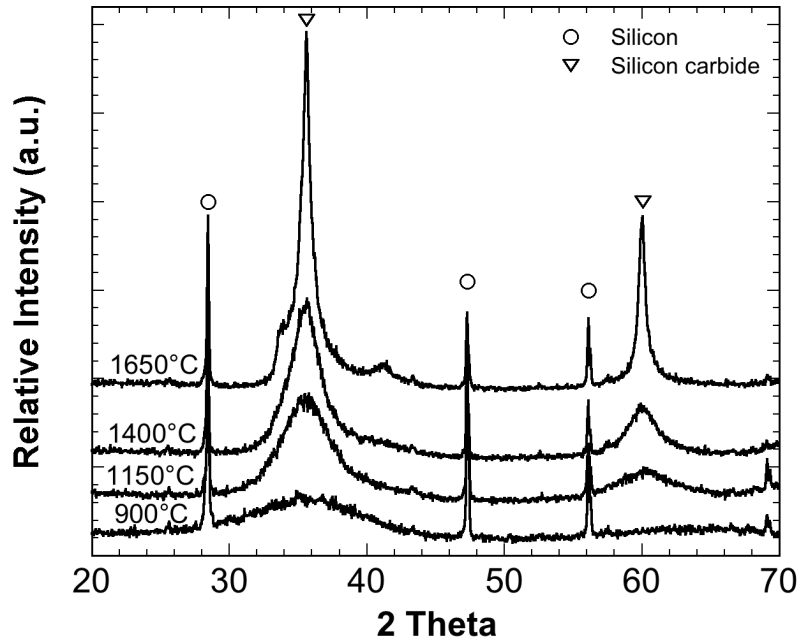
Figure 4.5: Powder diffraction patterns of SiC derived from AHPCS heated to 900°, 1150°, 1400° and 1650°C, from a professional laboratory (XRD.US).

added to the SiC sample powders. Similar observations, for this material system, have been reported in literature [97].

Further evidence of the presence of amorphous SiC at 900°C and its polycrystalline nature at higher temperature was seen from transmission electron microscopy. Figures 4.6–4.9 shows TEM micrographs obtained for SiC processed at 900°, 1150°, 1400°, and 1650°C, and held at the final temperature for 4h. While at 900°C, SiC is mostly seen in amorphous form, small domains of ordered regions are seen at some places. This is due to the long hold duration at this temperature. A lot of small crytalline regions are seen in SiC processed to 1150°C. Similar, but larger domains are seen at 1400°C. These domains appear to be surrounded by an amorphous phase as the one seen at 900°C. The TEM micrograph for 1650°C processing clearly shows large domains of well ordered material. All these domains are showing nanocrystalline SiC. A rough estimate of the size from TEM micrographs supports the crystal sizes determined by powder diffraction.
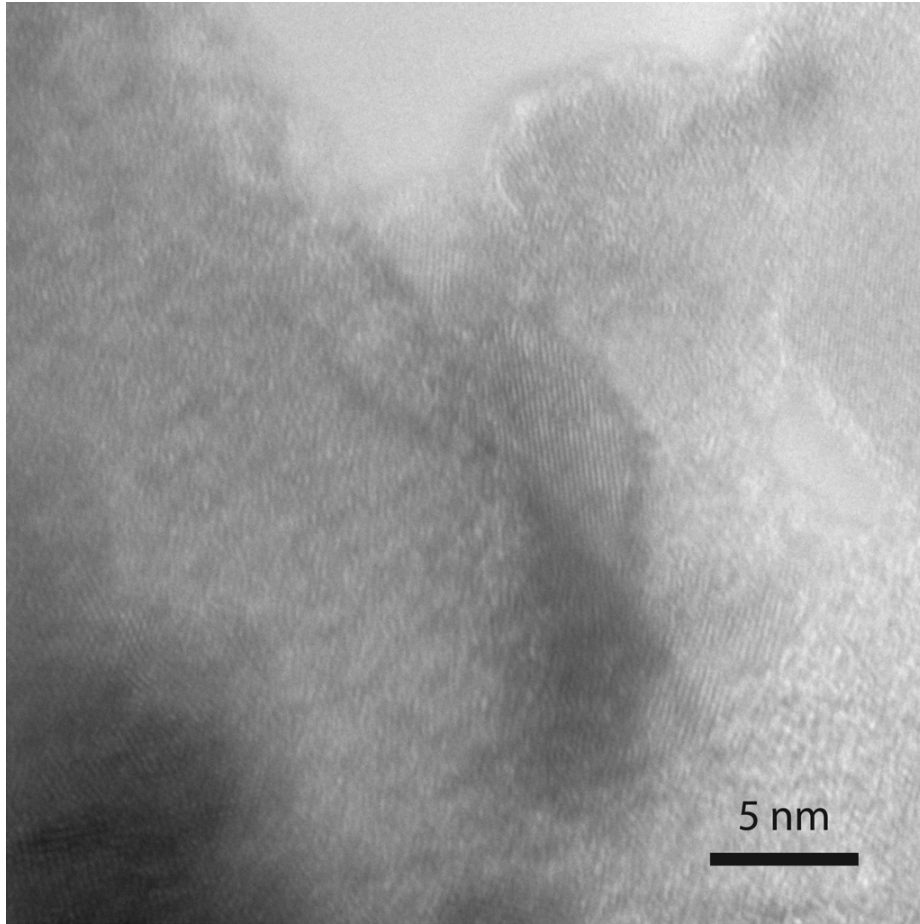
Figure 4.6: TEM micrographs for SiC derived from AHPCS heated to 900 °C and hold duration of 4h. While the microstructure is mostly amorphous, some areas of crystalline regions are seen.
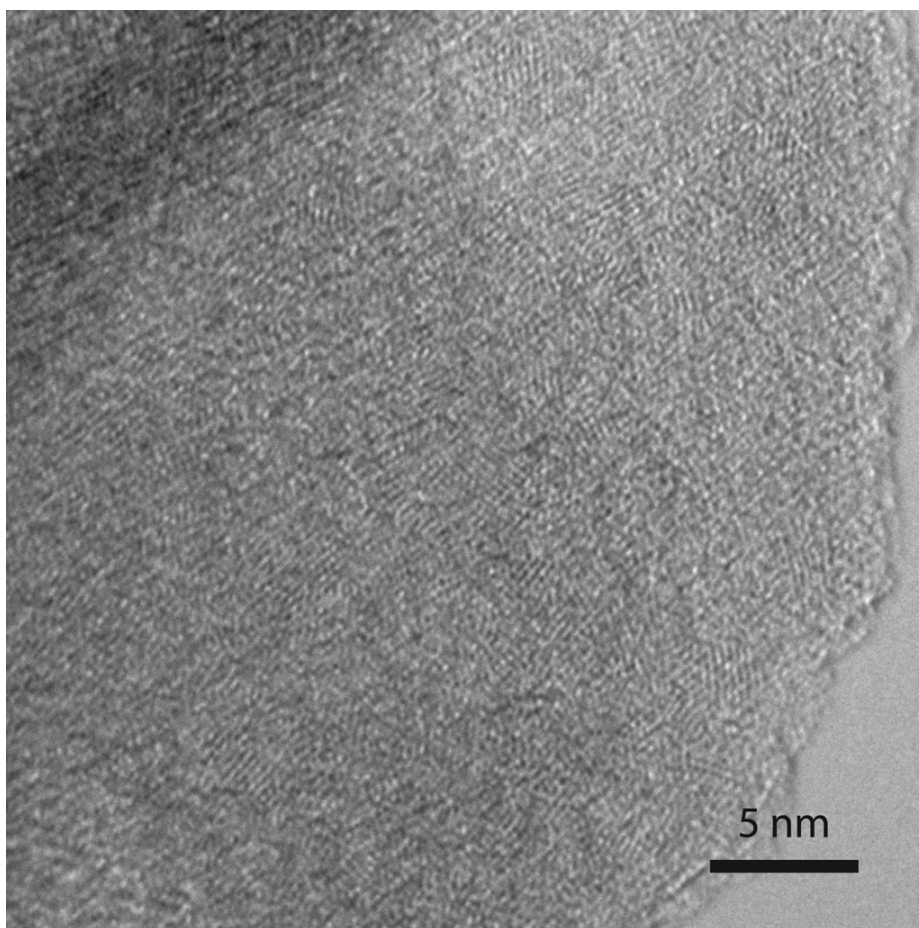
Figure 4.7: TEM micrographs for SiC derived from AHPCS heated to 1150 °C and hold duration of 4h. Large number of crystalline area with average size of 2-3 nm can be seen.
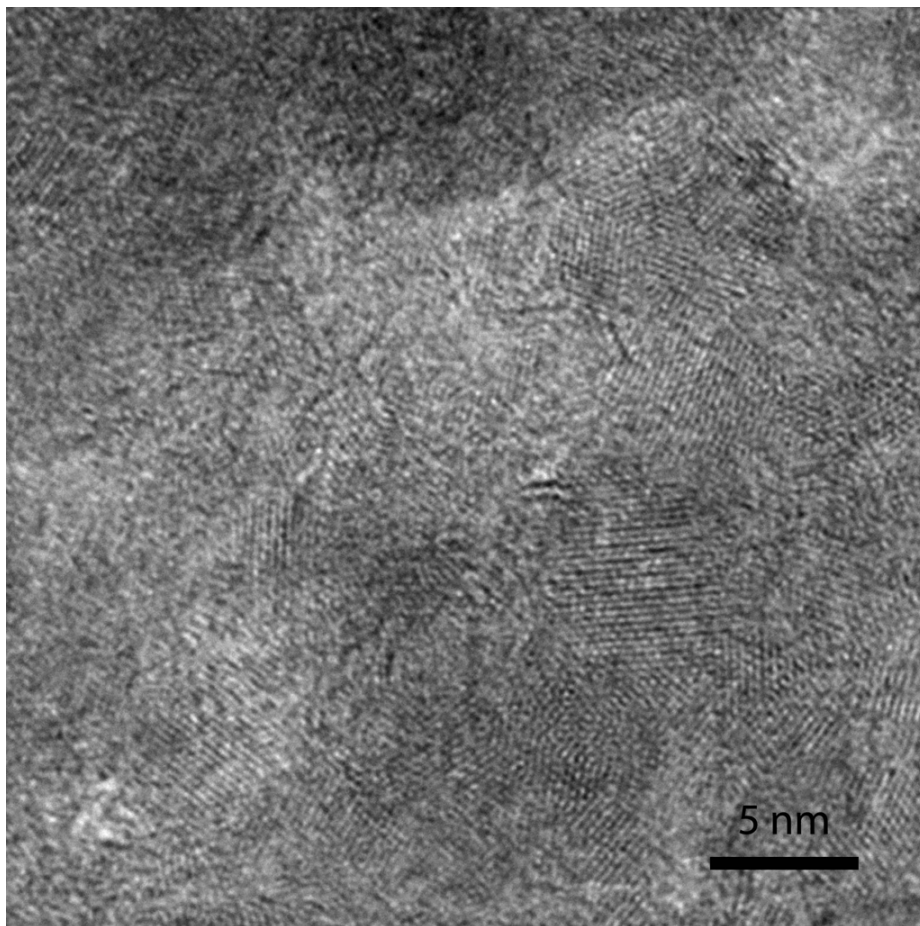
Figure 4.8: TEM micrographs for SiC derived from AHPCS heated to 1400 °C and hold duration of 4h. Crystalline regions of average size of 5-6 nm are seen.
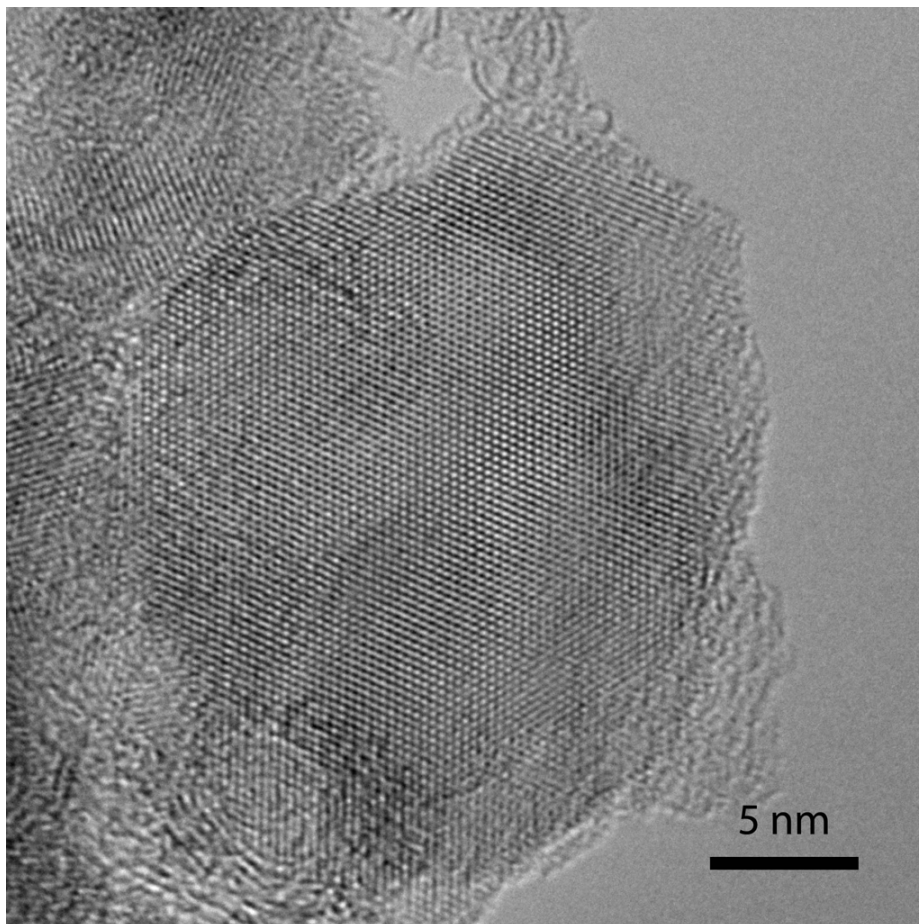
Figure 4.9: TEM micrographs for SiC derived from AHPCS heated to 1650 °C and hold duration of 4h. Large and distinct crystalline regions of 10–15 nm are seen.
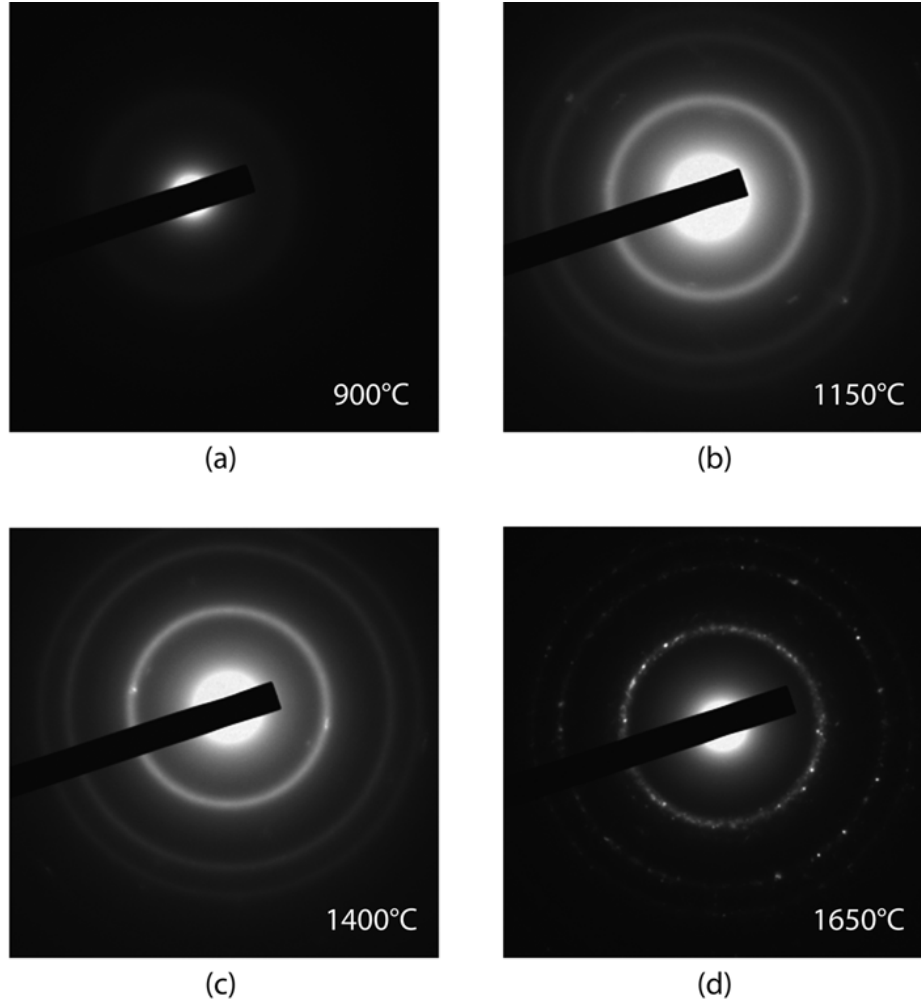
Figure 4.10: SAED patterns for SiC derived from AHPCS heated to (a) 900 °C, (b) 1150 °C, (c) 1400 °C and (d) 1650 °C.

Further, selected area electron diffraction (SAED) patterns were obtained during transmission electron microscopy (TEM) studies on these SiC samples and are shown in figure 4.10. As seen in the figure, greatly diffused concentric rings for SiC processed at 900 °C (a) suggests a largely amorphous structure. These rings are seen to gradually become distinct and sharp for SiC processed at higher temperatures (b–d), which is suggestive of growing crystallite size. SAED patterns obtained for SiC processed at 1650 °C (d) shows tiny bright specks intermittently along the rings. These are typically observed for nano–sized polycrystalline materials [121].

4.3 Mechanical Property Characterization

Mechanical properties of SiC derived from AHPCS pyrolyzed to $900°$, $1150°$, $1400°$, and $1650°C$ and held at the final temperature of 2 min, 60 min, and 4h were characterized in terms of hardness and elastic modulus using instrumented nanoindentation. Nanoindentation was performed using a Berkovich tip using various peak loads of 10, 25, 50, 75, and 100 mN. Indentations with multiple loads was performed to determine the loads required to obtain sufficient displacements, so as to obtain reliable results. Very low indentation loads would result in insufficient displacements that are influenced by surface effects and indenter tip radius, which would lead to inconsistent results. At the same time, very high loads would lead to large depths and results could be affected by porosity or substrate effects. Figure 4.11 show the values of hardness obtained for SiC processed at $900°C$ along with the error bars showing the standard variation. Large variation in data was observed at the low load of 10mN. At 25mN, data was consistent over multiple tests and a good nanoindentation depth of 250–300 nm was observed. Hence indentation data being discussed further is from experiments performed with peak indentation load of 25 mN.

Figures 4.12 and 4.13 show load-displacement plots typically obtained for these materials. A quick comparison of those obtained for materials processed at different temperatures with the same hold time of 1h (fig 4.12) suggests that the SiC obtained at $900°C$ is the most compliant amongst all, showing the highest deformation, and the materials processed to higher temperatures are less compliant. It is interesting to note that the depth of indentation does not decrease directly with increasing processing temperature. Material processed at $1150°C$ typically shows the lowest indentation depth followed by material processed at $1400°C$ and then that processed at $1650°C$. This suggest that during the processing of SiC, the materials undergoes change in mechanical properties, becoming harder at $1150°C$ and then softening when processed beyond this temperature. Similarly, a comparison of load-displacement plots for SiC
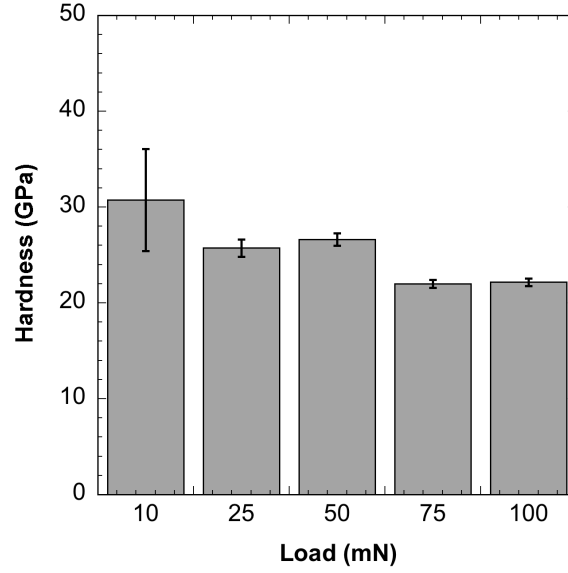
Figure 4.11: Modulus obtained with different indentation loads for SiC processed to 900 °C. Large error bar shows that lower load of 10 mN gave inconsistent results due to surface effects and low indentation depth.

processed to the same final temperature (1150 °C) and different hold times, as shown in fig 4.13, suggest a softer SiC when processed for 2 min hold time becoming hard when processed to 1h hold time and then softening again when processed further to 4h hold time. These trends differ greatly for different combinations of processing temperatures and hold times and can be better tracked in terms of the modulus and hardness.

Figures 4.15 and 4.14 show the hardness and modulus as a function of processing temperature. Error bars show standard deviation. Nominal values of hardness and modulus were obtained for SiC that was pyrolyzed at 900 °C with a hold time of 1h and 4h. For the 25 mN peak load, these values were about 160 GPa for modulus and about 23 GPa for hardness, which are typical for a–SiC. Material processed at 900 °C with a hold time of 4h showed higher values of about 197 GPa for modulus and about 25 GPa for hardness. There is considerable variation seen in hardness and modulus as a function of temperature and these variations are also dependent on the hold time
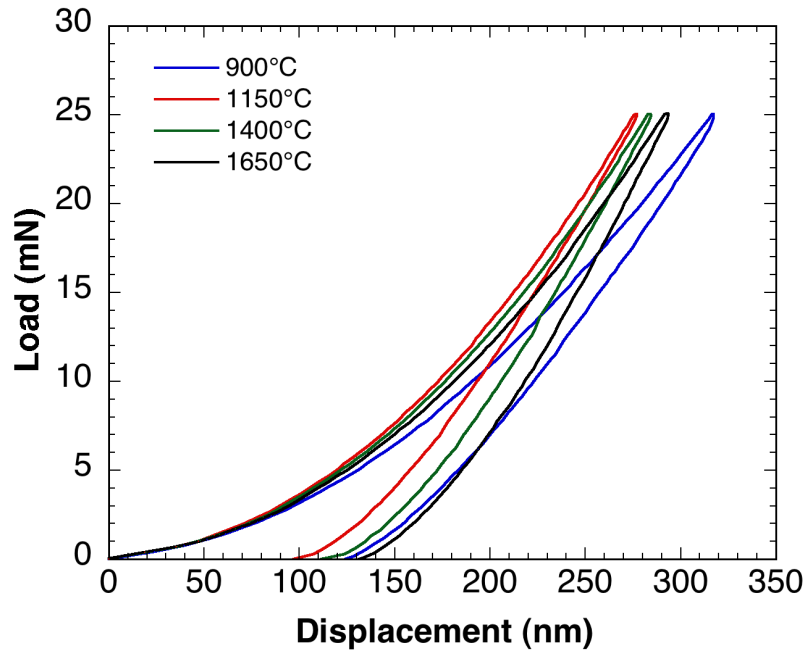
Figure 4.12: Load displacement plots obtained during indentation of SiC processed at different temperatures and for a hold time of 1h. Peak indentation load of 25 mN.
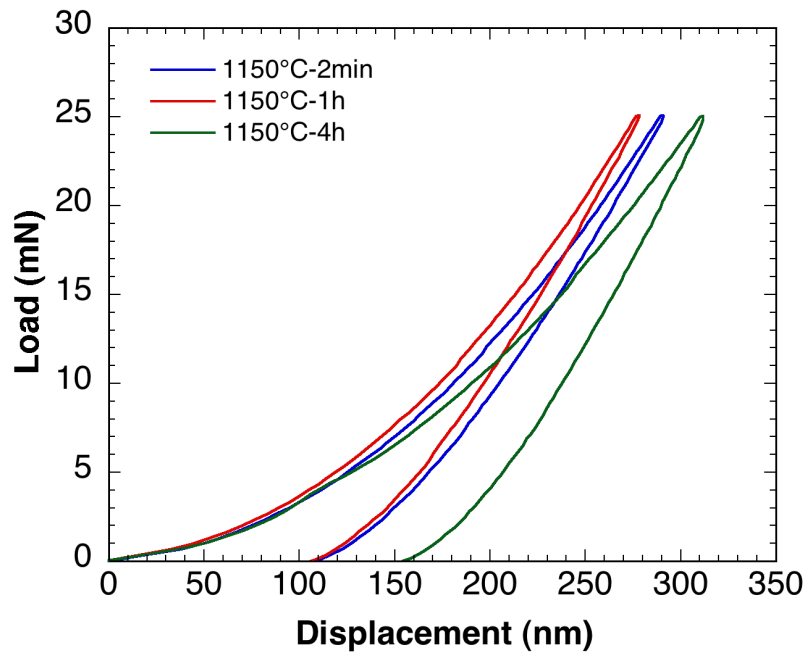
Figure 4.13: Load displacement plots obtained during indentation of SiC processed at 1150 °C and for different hold times. Peak indentation load of 25 mN.

at final temperatures. Figure 4.15 shows three curves for three different trends seen in the hardness values, as a function of processing temperature, for materials held for three different time durations at the final temperature. Materials held for 2 min and 1 h hold durations show a similar trend of an initial increase in the hardness values for materials processed at 1150 °C and then a drop in hardness progressively as material was processed to higher temperatures of 1400 °C and 1650 °C. Whereas materials held for 4h shows a progressive decrease in hardness with increasing processing temperatures. It is also interesting to note that the hardness values are very close for materials held for 2 min and 1 h hold durations at the lowest and highest processing temperatures being considered, i.e. at 900 °C and 1650 °C. The highest values for hardness of around 30 GPa were seen for the material processed at 1150 °C for a hold time of 1 h. This is about 52% higher than the lowest value, which is seen for material processed at 1650 °C and a hold time of 4 h. Similarly, figure 4.14 shows three curves for three different trends seen in the modulus values, as a function of processing temperature, for materials held for three different time durations at the final temperature. While values for modulus were very close for material processed for 2 min and 1h hold durations at temperatures of 900 °C and 1650 °C, the values peaked at 1150 °C for 1h hold samples and at 1400 °C for those held for 2 min. In both these cases, higher modulus values were seen at intermediate processing temperatures of 1150 °C and 1450 °C as compared to 900 °C and 1650 °C. Samples held for 4h at the final temperature show lowest values of about 197 GPa, which increases with processing temperature to about 205 GPa at 1650 °C. Just like in the case of hardness, highest values of modulus were observed for materials processed at 1150 °C for a hold time of 1 h. Highest modulus values were about 218 GPa, which is 37% higher than the lowest value which is seen for material processed with 2 min hold time at 900 °C.

Figures 4.16 and 4.17 show the hardness and modulus as a function of the hold
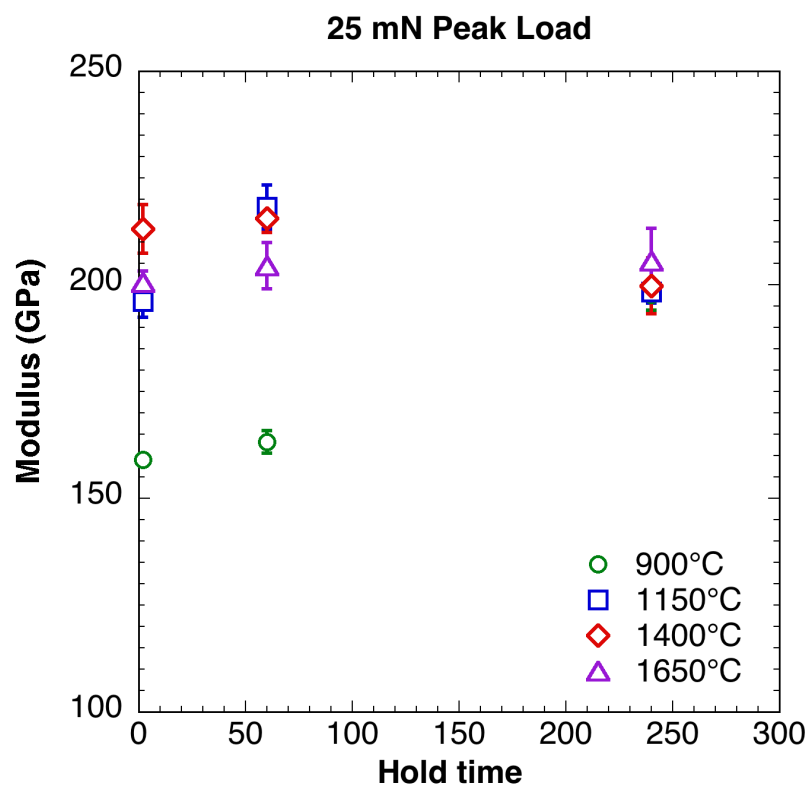
Figure 4.14: Hardness determined by nanoindentation for SiC derived from AHPCS heated to $900\,°$, $1150\,°$, $1400\,°$, and $1650\,°\mathrm{C}$, as a function of processing temperature.
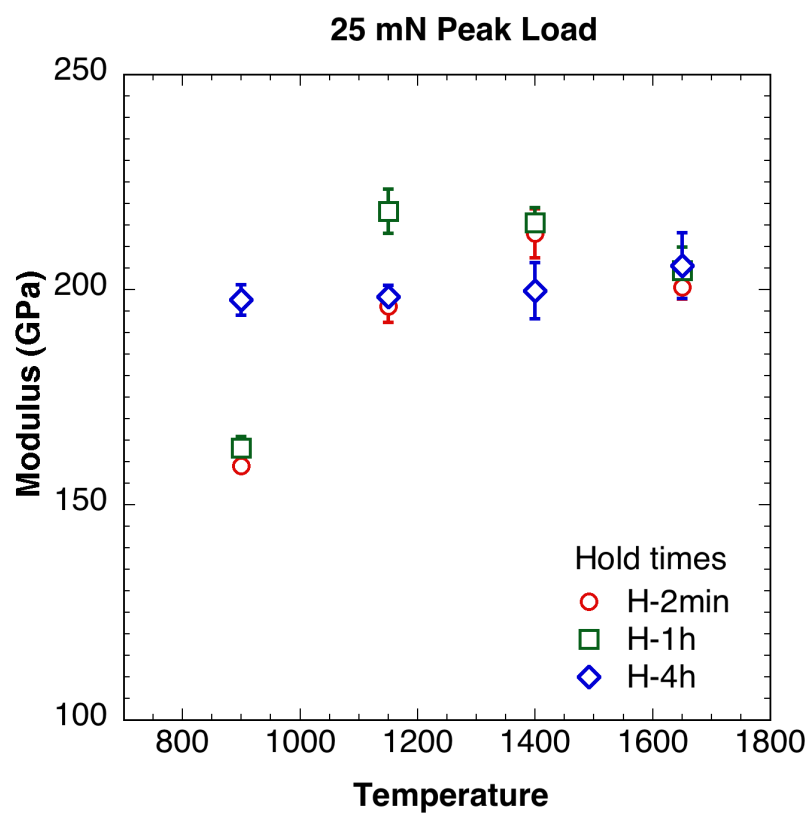
Figure 4.15: Modulus determined by nanoindentation for SiC derived from AHPCS heated to $900\,^\circ$, $1150\,^\circ$, $1400\,^\circ$, and $1650\,^\circ$C, as a function of processing temperature.
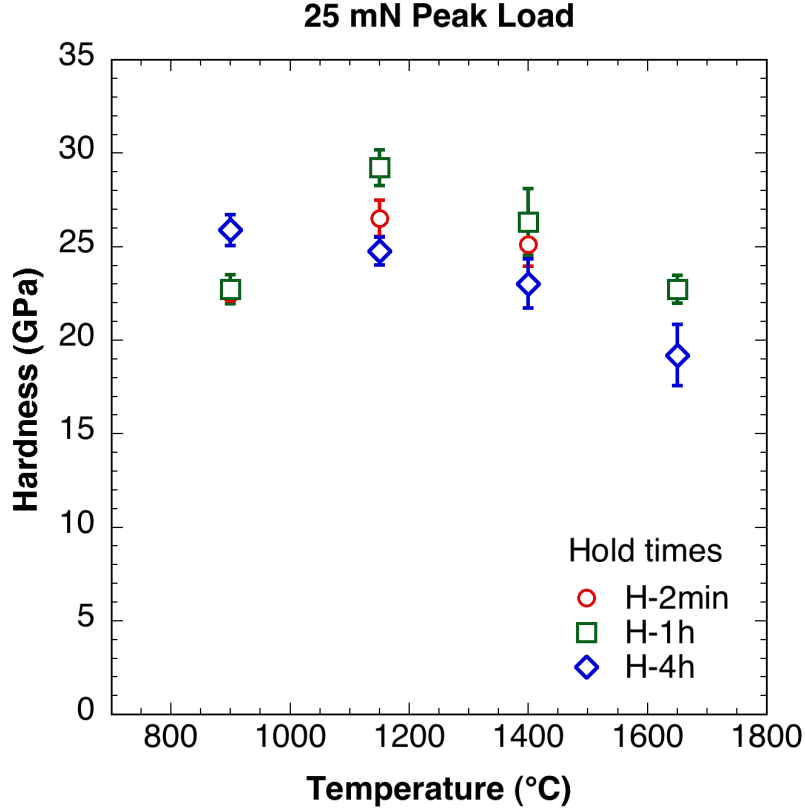
Figure 4.16: Hardness determined by nanoindentation for SiC derived from AHPCS heated to 900°, 1150°, 1400°, and 1650°C, as a function of hold duration at final temperature.

durations at final temperature for SiC processed to different temperatures. In general, for both hardness and modulus, progressive increase is seen for SiC processed to final temperature of 900 °C as the hold time at 900 °C is increased. On the other hand, SiC processed to 1650 °C shows continuous drop in hardness as the hold time is increased from 2 min to 4h. The values of modulus do not change significantly as a function of hold time for SiC processed to 1650 °C. For both, hardness and modulus, material processed to intermediate temperatures of 1150 °C and 1400 °C shows slightly higher values for hold time of 1h as compared to other hold times.

These results, in conjunction with the microstructural information at different temperatures, make for interesting observations. Amorphous SiC is formed at 900 °C

51
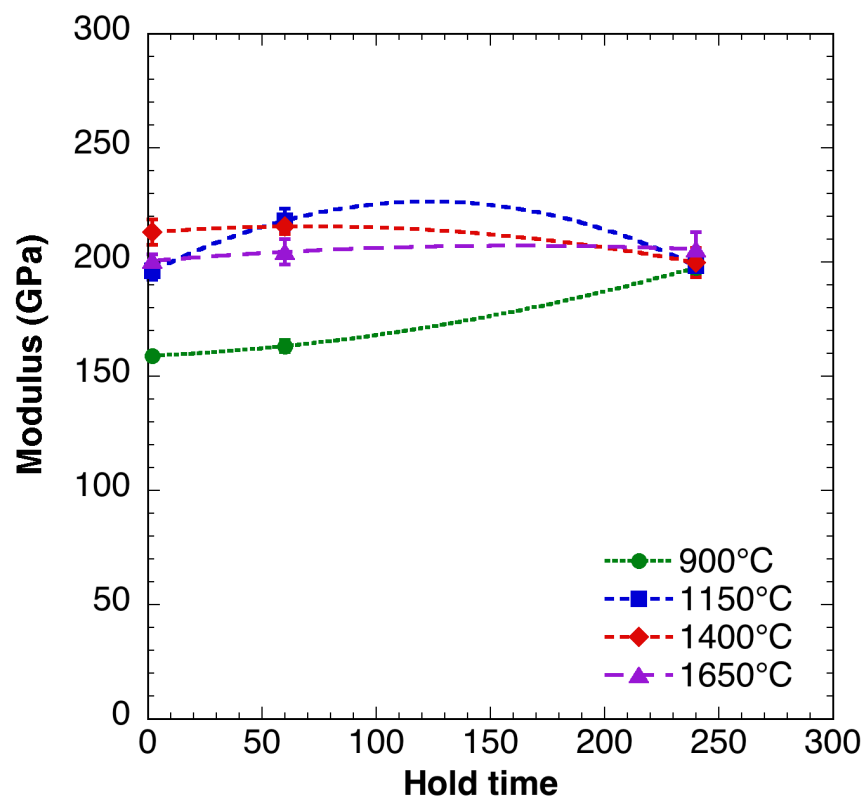
Figure 4.17: Hardness determined by nanoindentation for SiC derived from AHPCS heated to 900°, 1150°, 1400°, and 1650 °C, as a function of hold duration at final temperature.

No.	Material	Biaxial Strength (MPa)	Pyrolysis Temp. (°C)
1	SiC-900	In progress	900
2	SiC-1150	79.58 ± 8.11	1150
3	SiC-1400	85.26 ± 5.28	1400
4	SiC-1650	Oxidized	1650

Table 4.1: Biaxial strength of the SiC–SiC composites fabricated by using PIP route and tested using RoR biaxial flexure test

with 2 min hold time and increasing the hold time further densifies the material resulting in improvements in its mechanical properties. With a hold time of 4h, the microstructure remains mostly amorphous at 900 °C, but there are some crystalline regions formed which explain the small increase in mechanical properties observed for SiC processed at 900 °C for 4h. Nanocrystalline SiC with average crystal size of about 3 nm is formed at 1150 °C and this greatly influences its mechanical properties. SiC formed at higher processing temperatures of 1400 °C and 1650 °C had larger grain sizes but lower mechanical properties. This could be due to the classical Hall-Petch effect which ascribes increasing mechanical properties for smaller grains sizes to dislocation pile-up on grain boundaries. Varying the hold duration at final temperature has a limited effect on the mechanical properties. While hardness and modulus increases for amorphous SiC processed to 900 °C with increasing hold duration, for SiC processed to higher temperatures, these properties generally increased only marginally for 1h hold and generally decreased for 4h hold durations. Thus, there appears to be an optimum processing temperature (possibly about 1150 °C) that results in just the right grain size to achieve higher mechanical properties. Similarly, an optimum hold time of 1h results in better properties as compared to 2 min and 4h hold durations.

Unfortunately crystal size data could not be produced as a function of hold times for different final temperatures due to limited access to XRD facilities. Also, degree

of crystallinity measurements are desirable and would be invaluable in gaining further insight into the variation of microstructure and its influence on the mechanical properties. However, analysis of the powder diffraction data to determine degree of crystallinity for these sample would require detailed Rietveld analysis and was not undertaken in this study. Bulk properties in terms of biaxial strength was performed using RoR as described before. Table 4.1 lists the biaxial flexure strength obtained for the bulk samples composed purely of SiC derived from AHPCS and fabricated using the PIP process.

CHAPTER 5

Finite Element Modeling

5.1   Introduction

The goal of this investigation is to develop a better understanding of the processing – microstructure – property relationships for AHPCS-derived SiC. In order to optimize the overall mechanical properties of composite materials fabricated using AHPCS-derived SiC, it is necessary to systematically examine the influence of material morphology and constituent properties. As the mechanical properties of a material are governed by its microstructure, this implies one needs to be able to model the microstructure and deformation mechanisms that govern the resulting properties.

According to Meyers *et al.* [122], classical analytical solution methods are inadequate to obtain closed form solutions for polycrystalline materials and this necessitates the use of numerical modelling. They provide a comprehensive account of numerical models in literature targeted towards studying polycrystalline materials. Finite element methods (FEM) and molecular dynamics (MD) are the two numerical methods that are most commonly used to model polycrystalline and nanocrystalline materials. Further, irrespective of the method, most work in literature at this scale has focused on nanocrystalline metals, particularly Ni and Cu, and work on modeling of nanocrystalline ceramics has been extremely limited.

Using FEM, Fu *et al.* [123] studied the phenomena of grain boundary strengthening in polycrystalline materials, by idealizing the material as a two-dimensional composite of grain and grain boundaries. Material systems they studied included nanocrystalline iron and copper. They modeled the grain interiors using crystal plas-

ticity and grain boundary region using isotropic plasticity in an attempt to capture the increase in strength with decreasing grain size, which has been established experimentally. While working on FEM modeling of nanocrystalline Ni, Anand *et al.* [124] coupled a crystal-plasticity model for grain interiors with a elastic – plastic grain–boundary interface model. They introduced cohesive elements along the grain boundaries to model grain–boundary slip which account for reversible elastic, as well as irreversible inelastic sliding–separation deformations. According to them, a competition between grain-boundary deformation and grain interior deformation governs the observed macroscopic mechanical response in nanocrystalline materials.

Finite Element Modeling (FEM) has been well established in simulation of structural behaviors of composites owing to its capability to deal with multiple material constituents and flexibility of variation in materials properties parameters and morphology. However, FEM method is continuum based and has no intrinsic length scale associated. At the nanocrystalline level, the validation of a continuum model is a primary issue due to the associated length scales. The dimensions of grains in nanocrystalline materials are so small that classical continuum based theories may not be applicable. Length scale effects must be introduced through material models in the finite element calculation. Molecular dynamics is better equipped to handle such small length scales since it directly models the atoms and thus incorporates the atomic length scales of the crystal directly into the computation. While phenomena such as grain slipping can be easily handled by MD, development of specialized models is required to include these effects in finite element models. For phenomena that exist only at the length scales being investigated, obtaining the material constants and verifying the accuracy of the model independently from the systems being investigated is a major challenge [122].

As compared to FEM, more work has been done in modeling of nanocrystalline materials using MD simulations because of the advantages mentioned above. Exten-

sive MD modeling of nanocrystalline metals has been done by Van Swygenhoven and coworkers [125–128]. They have studied the role of grain-boundary structure using models of polycrystalline nickel and copper with average grain sizes between 5–12 nm. For a uniaxial state of stress they found that there was no damage accumulation during deformation and there was a change in the deformation mechanism which was governed by the grain size. While all deformations were accommodated in the grain boundaries and grain boundary sliding at smallest grain sizes ($\sim$3 nm), a combination of sliding and intra-grain dislocation activity was observed for large grain sizes (10–12 nm).

While most of the simulations of nanocrystalline materials involve uniaxial deformations, other dynamic phenomena have been studied as well. While studying nanoindentation, modeled by defining a moving repulsive potential on gold, Swygenhoven *et al.* [129] found that, for an indenter smaller than the grain, dislocation absorption and emission took place at the grain boundaries. In their study, the MD model contained 15 grains with a mean diameter of 12 nm and was indented with a spherical indenter with a radius of 40 $\mathring{A}$. Molecular dynamic simulations has thus helped understand the deformation processes at the length scales of the nanocrystalline grain size. A summary of the general things learnt from MD simulations is presented in Derlet *et al.* [128].

However MD modeling has several limitations, as pointed out by Meyer *et al.* [122], associated with time scales, length scales, and computational costs. Molecular dynamics calculations occur at extremely high strain rates that cannot be reproduced experimentally. The length scales of MD models has a direct bearing on the computational cost and this has limited the sample size to a great extent. As a result of this, direct comparisons to results of macroscopic experiments are not possible.

Other than FEM and MD models, there have been efforts to describe deformations in nanocrystalline materials using simple mixture based models. Kim *et al.* [130] mod-

eled the plastic deformation of nanocrystalline materials with a constitutive equation based on the evolution of the dislocation density. In their model, the mechanical properties of the crystalline phase were modeled using unified viscoplastic constitutive relations and the deformation mechanism for the grain-boundary phase modeled as a diffusional flow of matter through the grain boundary. They analyzed the overall plastic deformation of the composites as function of grain size by using a simple rule of mixtures approach. According to the authors, their model is able to interpret the breakdown of the Hall–Petch relation with decreasing grain size and the rate dependence of the deformation behavior. In another mixture based model, Zhou *et al.* [131] investigated the effect of grain size and porosity on the elastic modulus and strength of porous and multi-phase nanocrystalline ceramics. The authors developed a mixtures-based model to describe the mechanical behavior of constituent phases and further applied Budiansky's self-consistent method [132] to determine the effective mechanical properties of the composites. However, their model does not look at the deformation mechanisms governing the mechanical properties at small scales and hence the model fails to show any decrease in mechanical properties as a function of grain size that would occur due to grain-boundary activity.

A method that couples atomistic MD approach and continuum approach is the quasicontinuum method (QC) developed by Tadmor *et al.* [133–136]. In this method, MD approach is applied to the areas where critical phenomena occur while the surrounding areas are modeled using FEM. This approach has been successfully applied to look at problems such as interactions of cracks with grain boundaries [135] and dislocation generation at grain boundaries [137].

Another numerical modeling approach which has great potential and gaining attention for modeling deformation in nanocrystalline materials is the generalized interpolation material point method (GIMP) [138–140]. GIMP is an improvement over the material point method (MPM), overcoming its limitations with handling large

scale deformations. Further, GIMP can deal with the multi-scale modeling approach and has the potential to bridge the gap between the atomic level modeling methods (MD) and continuum based methods (FEM). Moreover, there have been successful efforts to couple MD with MPM [139, 141, 142].

However, in the current work, effort is directed towards modeling the polycrystalline material using the simplest approach. Finite element modeling was adopted simply due to the ease of use, relatively short learning curve, and availability of user-friendly commercial code such as ABAQUS.

5.2 Procedure

A two dimensional diagram consisting of randomly distributed crystals was created using a centroidal voronoi tessellation (also called called Dirichlet or Thiessen tessellation). Voronoi tessellation divides a given space into a set of disjoint and convex voronoi polytopes. Given a number of seed points, N, to divide a space R_d into N voronoi polytopes, N nuclei points are randomly generated in the space and the set of points closer to a nucleus P, than the neighbouring nuclei, is assigned to the nucleus P. The points that are equidistant from a pair of seeds lie on the boundary between two adjacent polygons and those equidistant from three points form the vertex of three adjacent polygons. This is typically achieved by introducing planar cell walls as perpendicular bisectors of line connecting neighboring points (seeds). The resulting polygons form a contiguous, space-exhaustive tessellation that is unique for any given distribution of points [143]. A centroidal Voronoi tessellation (CVT) is a Voronoi tessellation of a given set such that the associated generating points are centroids of the corresponding Voronoi regions. Voronoi tessellation has been extensively used in materials science for modeling microstructure of randomly distributed grains in polycrystalline materials [123, 124, 144–146].

From a material science perspective, the Voronoi tesselation can be interpreted

in terms of a simple homogenous crystal growth process with the following assumptions [143, 147]

1. All nuclei appear simultaneously.

2. All nuclei remain fixed in location throughout the growth process.

3. All nuclei are weighted equally.

4. For each nucleus growth occurs at the same rate in all directions.

5. The linear growth rate is the same for each cell associated with a nucleus.

6. Growth ceases for each cell whenever and wherever it comes into contact with a neighboring cell.

A large number of codes, using different algorithms, to generate Voronoi diagrams are freely available. We have used a code for Matlab written by Dr. John Burkardt at the Florida State University [148, 149] that allows for interactive control over the refinement of a Voronoi diagram. The code uses the function voronoi(x,y) available in Matlab which plots the bounded cells of the Voronoi diagram for the points x,y. The relevant code is listed in Appendix A. The output of this code consist of two sets of X, Y coordinates, each for the starting and ending vertices of lines which for the edges of grains and also a set of vertices for the seeding points. The output format looks like the following,

```
vx =

    x1,1   x1,2   x1,3    x1,4    x1,5    ...

    x2,1   x2,2   x2,3    x2,4    x2,5    ...

vy =

    y1,1   y1,2   y1,3    y1,4    y1,5    ...

    y2,1   y2,2   y2,3    y2,4    y2,5    ...
```

```
x1 y1
x2 y2
x3 y3
x4 y4
x5 y5
```

where the the first row in vx and vy are the X,Y coordinates of the staring point of the lines and the second rows in each vx and vy are the X,Y coordinates of the end points of the lines, which form the edges of the Voronoi polygons. The list of coordinates at the end are those for the seeding points generated randomly.

Since the output is a set of lines in no particular order, the next step was to determine the lines that belong to particular individual grains. To do this a program was written in C making use of the fact that all points inside the Voronoi polygons are closer to its seeding point than any other neighboring seeding points. The flow chart for this program in figure 5.1. The source code is listed in Appendix B. The output of is a sets of coordinates for lines corresponding for grain edges grouped together for individual grains.

To incorporate a grain boundary phase around each grain, a small isotropic in-plane compression is applied to each Voronoi grain. When grains are compressed in this fashion, an inter-granular space is created which form the grain boundary phase. For this purpose another code was written in C. The compression is achieved by drawing a vector from each coordinate on the edges of the grain to the centroid and translating the points on the edges towards the centroids by a certain translation factor, r. Area fraction occupied by grains and grain boundary is calculated. The value of r can be set to obtain a desired grain-grain boundary area fraction. Since the model is two dimensional, this area fraction covered by grains becomes the volume fraction of crystalline material in the polycrystalline model. This approach has been
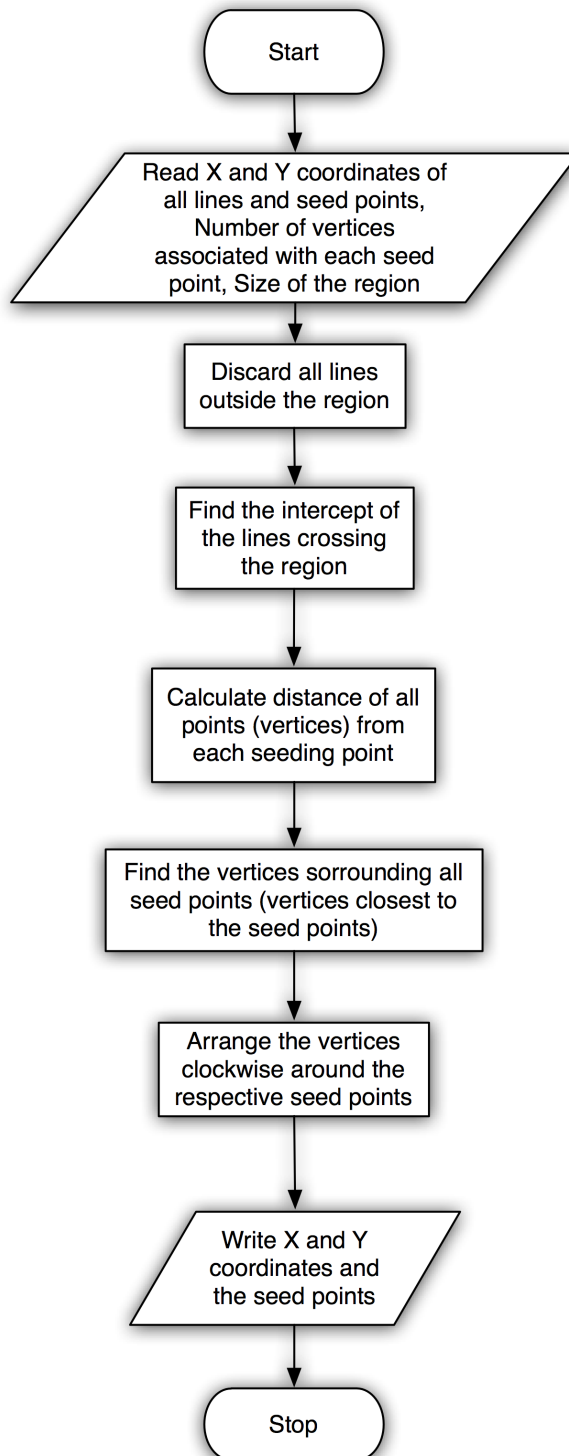
Figure 5.1: Flowchart of code that groups edges forming individual grains when given a Voronoi diagram with edges in no particular order. Code listed in Appendix B.

used by Zhang *et al.* [146] to create grain boundary phase in finite element modeling of polycrystalline silicon carbide.

The flow chart of the program written for compressing the grains and the output of the program is shown in figure 5.2. As an output, this code gives the coordinates that are the points on the edges of the compressed grains grouped together for each grain, with the grains themselves not arranged in any particular order. This became the input for the next step of drawing these grains for finite element modeling. The code for compressing grains and calculating the crystalline fraction is included in Appendix C.

Finite element modeling was done using ABAQUS Standard using two different approaches. To save time and labor, scripts were written in PYTHON for automating the tasks such drawing grains, assigning material properties, etc. In the first approach, each grain and grain boundary surrounding to that grain were formed as individual parts. In this way, for a 25 grain model, the number of parts were 50 (25 grains and 25 grain boundaries), the number of parts for a 100 grain model were 200, and so on. Once all the grains were drawn as individual parts, they were assembled into a single assembly. Following this, the edges of each grain were tied to the corresponding grain boundary edges and the edges of adjacent grain boundaries were tied to each other. Figure 5.3 shows a typical grain and grain boundary modeled as different parts before assembly. All the grains and grain boundaries were then assigned corresponding properties as described later. A sample PYTHON code that generates a 25 grain model by sketching 25 grains and 25 grain boundaries, assembles them into one assembly, and assigns material properties to all grains and grain boundaries is provided in Appendix D. This approach of forming each grain and grain boundary became very laborious for larger number of grains particularly because of the process of tying each as mentioned before. Hence, this approach was quickly discarded in favor of the following alternative approach.
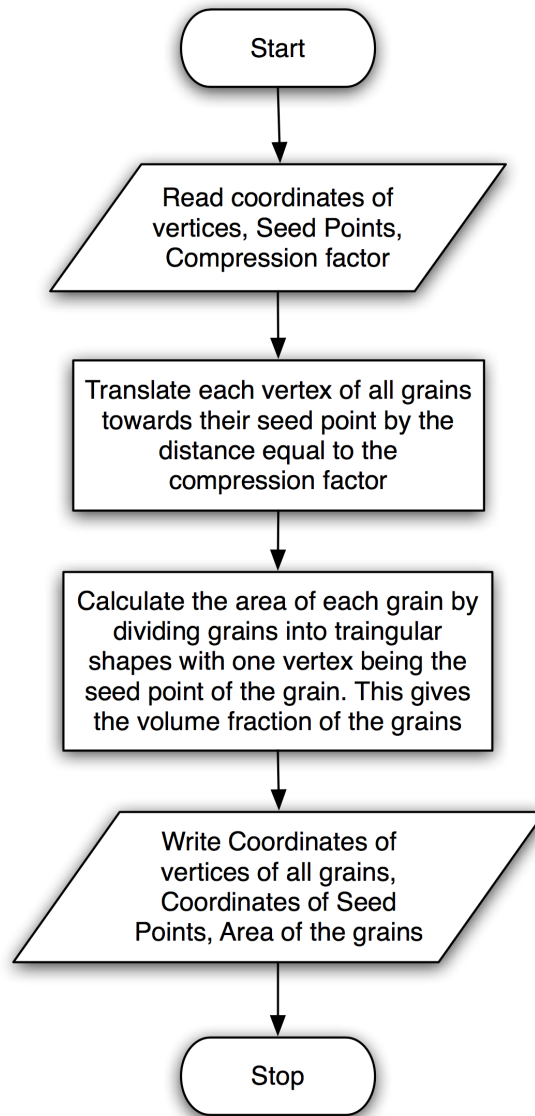
Figure 5.2: Flowchart of code that applies an isotropic compression to Voronoi grains to create an inter-granular region and calculates the area fraction occupied by the grains. Code listed in Appendix C.
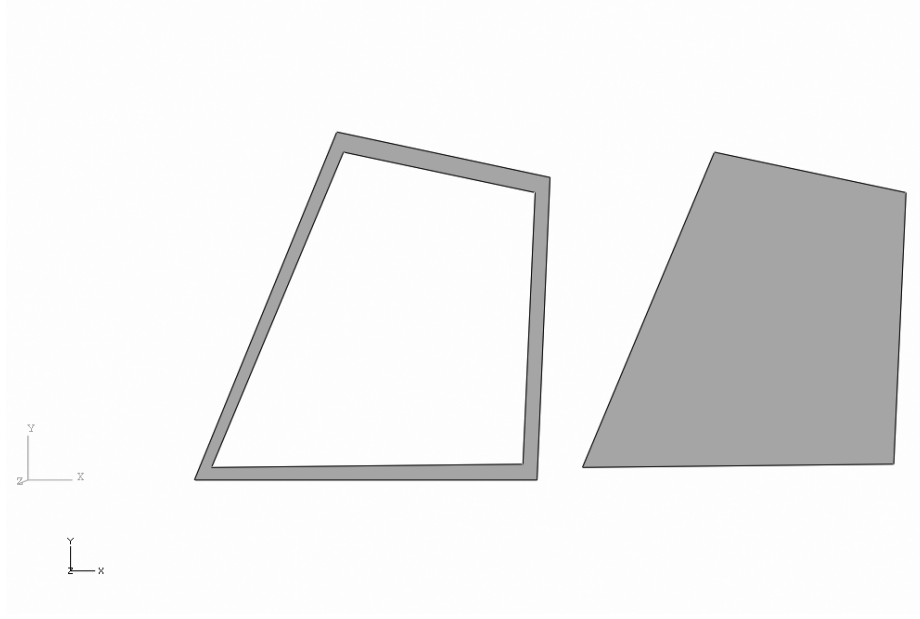
Figure 5.3: Typical grain and grain boundary modeled as different parts.

In the second approach, a single part was formed by drawing grains onto a unit square using the coordinates, obtained after compression of Voronoi grains, as the input vertices for the grain edges. After all the grains were drawn, the section was partitioned using the edges formed by grains. This resulted in a two dimensional model, as shown in figure 5.4, containing grains as obtained from compression of Voronoi polytopes embedded in a unit square domain. The area between the grains forms a continuous two dimensional network of inter-granular region which is assigned the properties of grain boundary phase. The dimension of the square domain was assumed to be 100×100 nm, unless otherwise noted.

Unlike in the earlier approach, tying of edges between grains and grain boundaries is not required in this route and hence saves considerably time and labor; hence this approach was adopted for all further models.
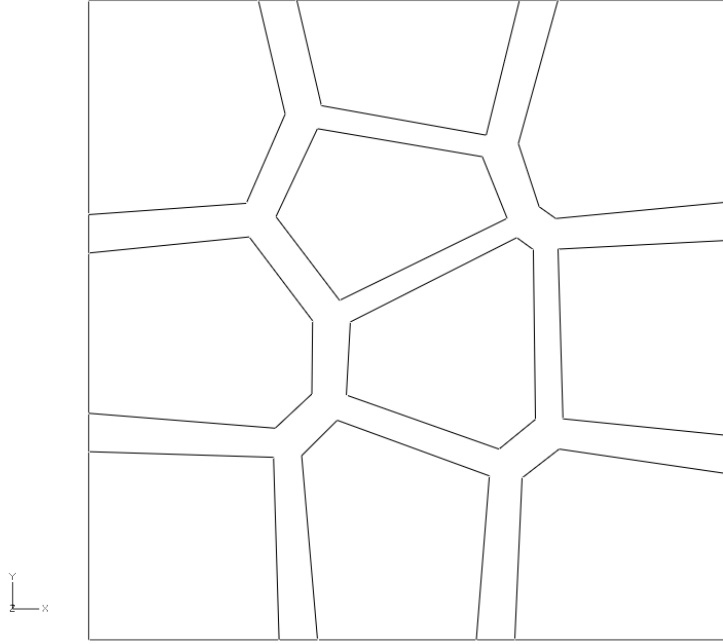
Figure 5.4: A typical two dimensional model generated by drawing and sectioning Voronoi grains on a unit square.

5.3   Polycrystalline Models

The polycrystalline model can be considered to be a composite with purely crystalline grains surrounded by a purely amorphous grain boundary matrix. For all the models described here, the grain and grain boundary material are considered purely elastic with elastic modulus for grains assumed to be equal to that of pure crystalline β–SiC (262 GPa) [150] and that for the grain boundary phase assumed to be equal to that of amorphous SiC (159 GPa) [151]. The assumption of purely elastic property for grain and grain boundary is a simplified approximation and is justified in this case by the purpose of these model, which is to simply determine the effective elastic modulus of the composite polycrystalline materials.

The approach described in the earlier section allows for control over three variables in the models: the number of grains, the average size of grains and the volume fraction occupied by grains. For a given unit square model, there is a degree of freedom of two

No. of grains	Avg. grain size	Crystalline vol (%)
100	5.04 nm	20
100	7.13 nm	40
100	8.74 nm	60
100	10.09 nm	80
100	11.28 nm	100

Table 5.1: Approximate average grain sizes obtained for 100 grain models with given crystalline vol. fraction.

in these variables; any two of these variables could be changed while the third was determined. Using the procedure described in the earlier section, three different sets of models with different morphologies were studied. In the first set, four 100-grain models were generated by varying the volume fraction occupied by the crystalline phase from 80% to 20%. The grain sizes were determined approximately by assuming the grains to be circular in shape and are listed in Table 5.1. The model generated by using Voronoi grains without any compression gives a 100% crystalline model as shown in figure 5.5. The models resulting after compression varied in both volume fraction as well as the grain size. Figure 5.6 shows the models generated for different volume fractions containing 100 grains each.

To determine the effect of changing volume fraction of crystalline phase on the effective elastic modulus, a set of models was created with an average grain size of 10 nm in all models and the crystalline volume fraction was varied from 20% to 80%. The number of grains required to achieve this varied, and are listed in table 5.2; the models are shown in figure 5.7.

In the third set, the attempt was to examine if the model could capture the effect of varying the average grain size alone on the effective modulus, a set of models was created with 80% crystalline volume fraction in each. The number of grains required
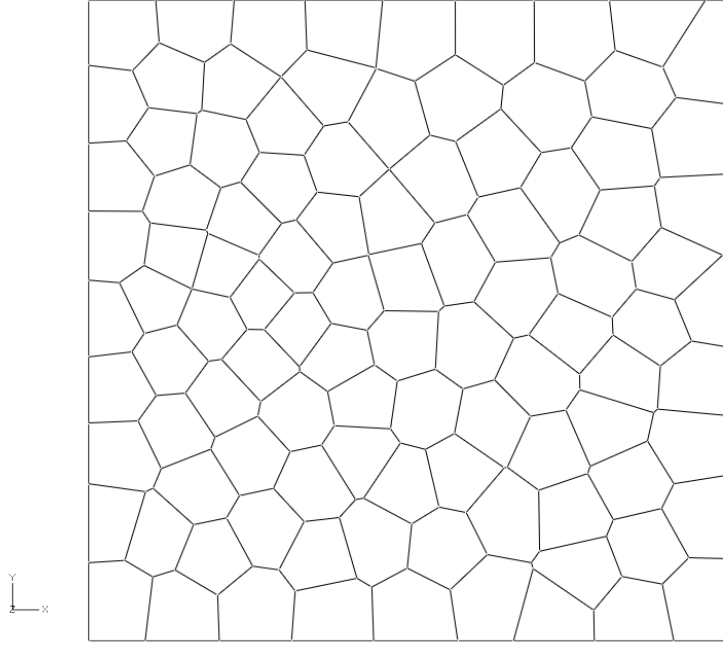
Figure 5.5: A 100 grain model with 100% crystalline volume fraction.

No. of grains	Avg. grain size	Crystalline vol (%)
100	10.09 nm	80
75	10.09 nm	60
50	10.09 nm	40
25	10.09 nm	20

Table 5.2: Number of grains required to achieve models containing grains averaging 10 nm in size, occupying different volume fractions.
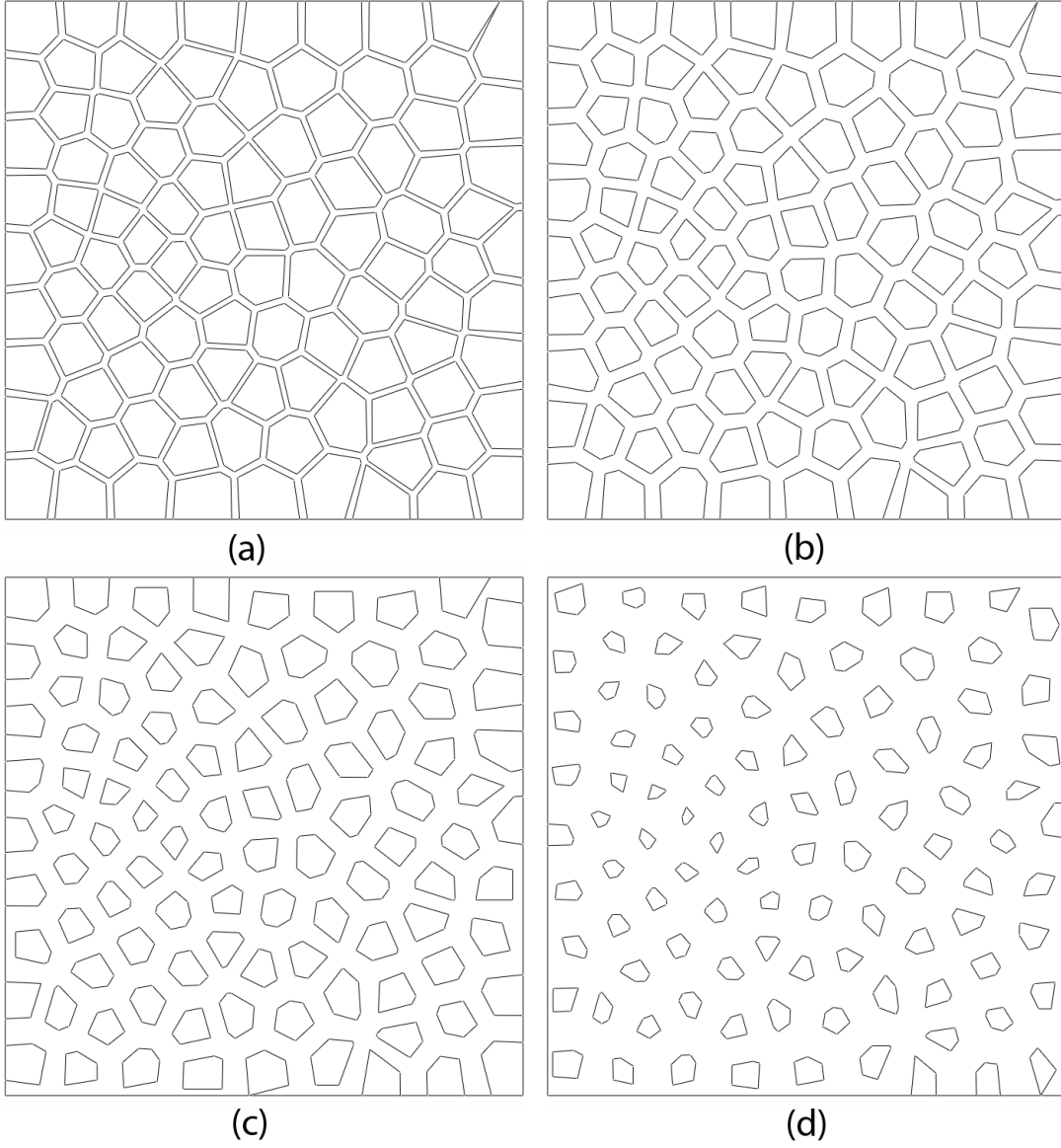
Figure 5.6: 100 grain models with different crystalline volume fractions: (a) 80%, (b) 60%, (c) 40% and (d) 20%. The resulting grain sizes are listed in table 5.1
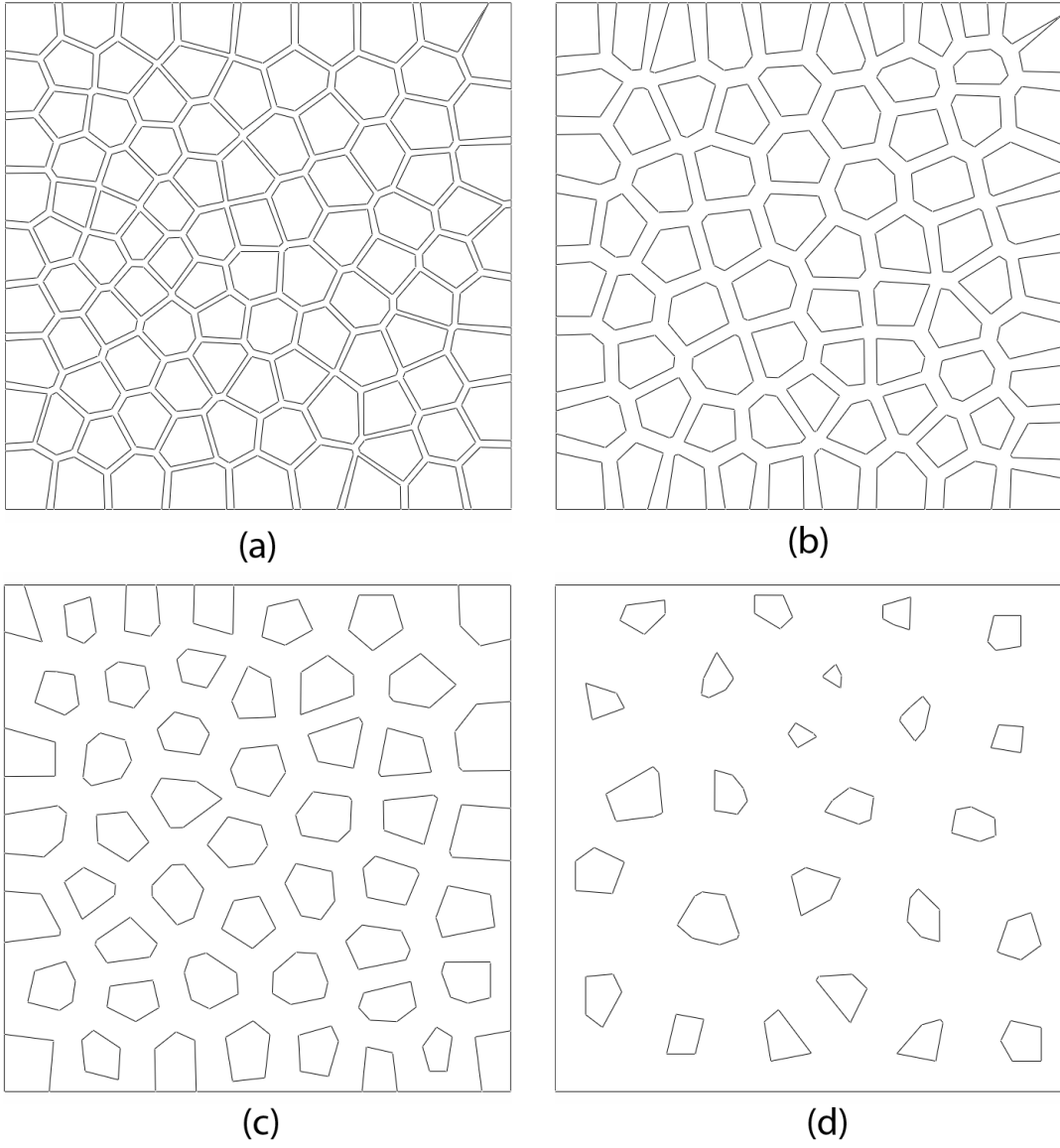
Figure 5.7: Models with different crystalline volume fractions and average grain size of 10 nm in all models; (a) 80%, (b) 60%, (c) 40% and (d) 20%.

No. of grains	Avg. grain size	Crystalline vol (%)
100	5 nm	80
25	10 nm	80
10	15 nm	80

Table 5.3: Number of grains required to achieve 80% crystalline volume fraction with predetermined grain sizes.

to achieve this varied, and are listed in table 5.3. Figure 5.8 show the models. In this case, the global size of the square domain was used at 50 nm × 50 nm so as to achieve the required grain sizes of 5, 10, and 15 nm. These grain sizes were chosen based on earlier experimental results.

The global mesh size for all models was set to 0.01. This mesh size optimizes accuracy and computational cost and was selected after a comparison of modulus values obtained using different mesh sizes. As seen in figure 5.9, reducing the mesh size did not significantly change the modulus values obtained. Figure 5.10 shows a typical model after meshing. Primarily, ABAQUS linear, quadrilateral, plain stress, continuum elements with reduced integration (CPS4R) were used, along with 3-node, linear, plane stress triangular continuum elements (CPS3), wherever required. The total number elements varied between 11500 and 11800.

Since the experimental data in this work was generated by nano-indentation, the boundary conditions and loading conditions were set to simulate loading under an indenter. Although ideally, a three-dimensional model is required to accurately determine the complex stress state under the indenter, a greatly simplified approach of uniform compression on the top surface of the model is used in this work. Motion of a corner node on the bottom edge was constrained in both X and Y directions ($U_1=U_2=0$) and all nodes on bottom edge were constrained in Y direction ($U_2=0$). A uniform strain of 0.05 in the negative Y direction was applied to all nodes on the
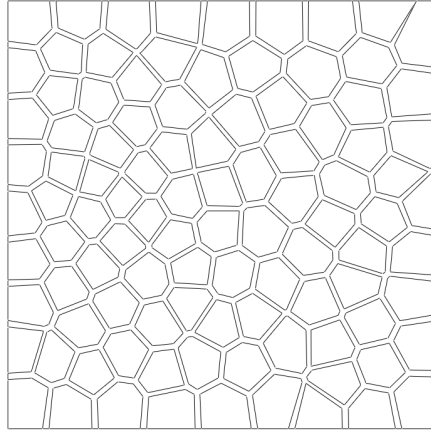
(a)
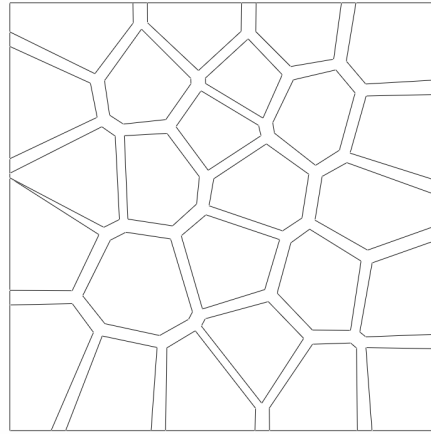
(b)
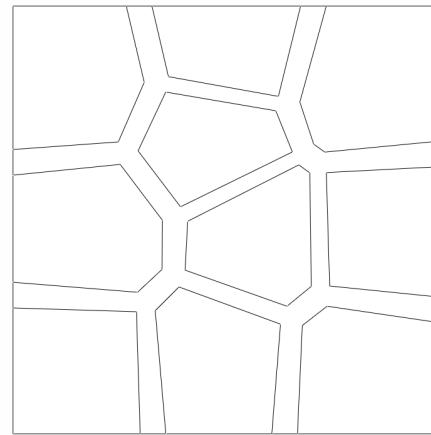
(c)

Figure 5.8: Models with same crystalline volume fraction of 80% and different grain sizes; (a) 5 nm, (b) 10 nm, (c) 15 nm. Note that, in this particular case the unit square represent 50 nm x 50 nm.
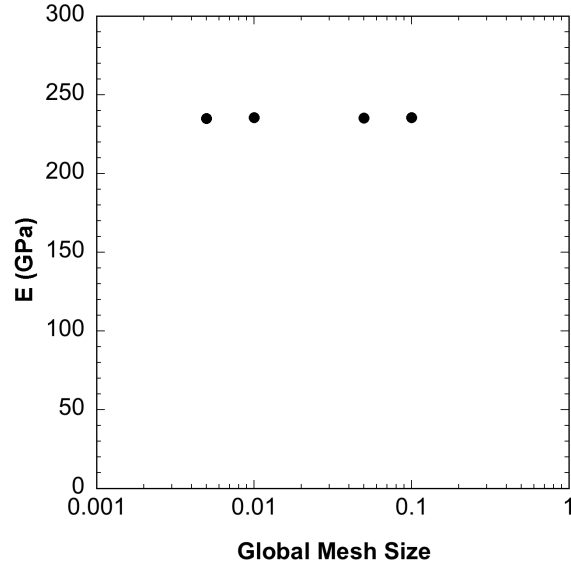
Figure 5.9: Elastic modulus determined with different mesh sizes.
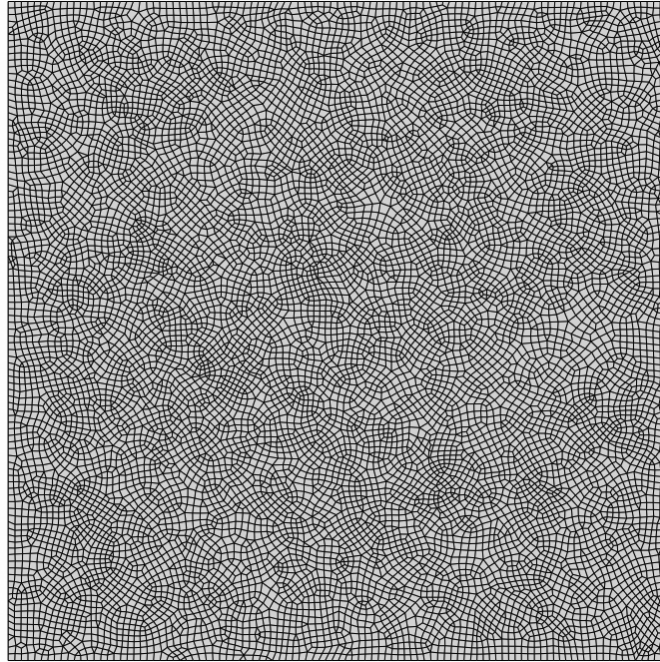
Figure 5.10: A typical polycrystalline model after meshing. Primarily, continuum elements with reduced integration (CPS4R) were used, along with 3-node, linear, plane stress triangular continuum elements (CPS3), wherever required.

73

top surface (U_2=-0.05). Stress-strain curves were plotted using the reaction forces, resulting from the given strain, summed over all the nodes on the top surface. The elastic modulus was determined from the slope of these stress-strains plots.

5.4   Results

Multiple models were generated starting with the Voronoi polycrystals and varying the number of grains, grain sizes and the crystalline volume fraction. These models were elastic–elastic with grain and grain boundaries treated as purely elastic. Elastic modulus of amorphous SiC, determined from experiments, was prescribed to the intergranular regions, while the elastic modulus of β–SiC was prescribed to all the grains. The first set of models contained 100-grains in each case with volume fractions of the crystalline phase between 80–20%. The deformed models after applying a uniform strain (of -0.05) on the top surface are shown in figure 5.11 (a–d). The effective elastic modulus determined from these models is plotted as a function of crystalline volume fraction in figure 5.12. It is important to note that, the modulus here is not simply a function of the crystalline volume fraction but also depends on the grain sizes. Hence, the variation in the grain size for these models, as noted in the earlier section is also show in the gure 5.12. A comparison of the deformed models shows that the higher stresses were generated in the model with higher crystalline volume fraction as compared to those with higher amorphous fractions. This is expected since higher volume fraction of amorphous phase, which has a lower elastic modulus, makes the models more compliant. For the same reason, as seen in figure 5.12, the stresses within the grain were higher compared to those in the intergranular regions.

The second set of deformed models with average grain size of 10 nm in each and crystalline fraction of 20, 40, 60, and 80% is shown in figure 5.13. These models were intended to capture the influence of crystalline volume fraction on the effective elastic modulus, independent of the grain sizes. Figure 5.14 show the effective elastic mod-

S, Mises
(Avg: 75%)
+1.378e-04
+1.330e-04
+1.281e-04
+1.231e-04
+1.182e-04
+1.133e-04
+1.083e-04
+1.034e-04
+9.847e-05
+9.353e-05
+8.860e-05
+8.367e-05
+7.873e-05
+7.380e-05
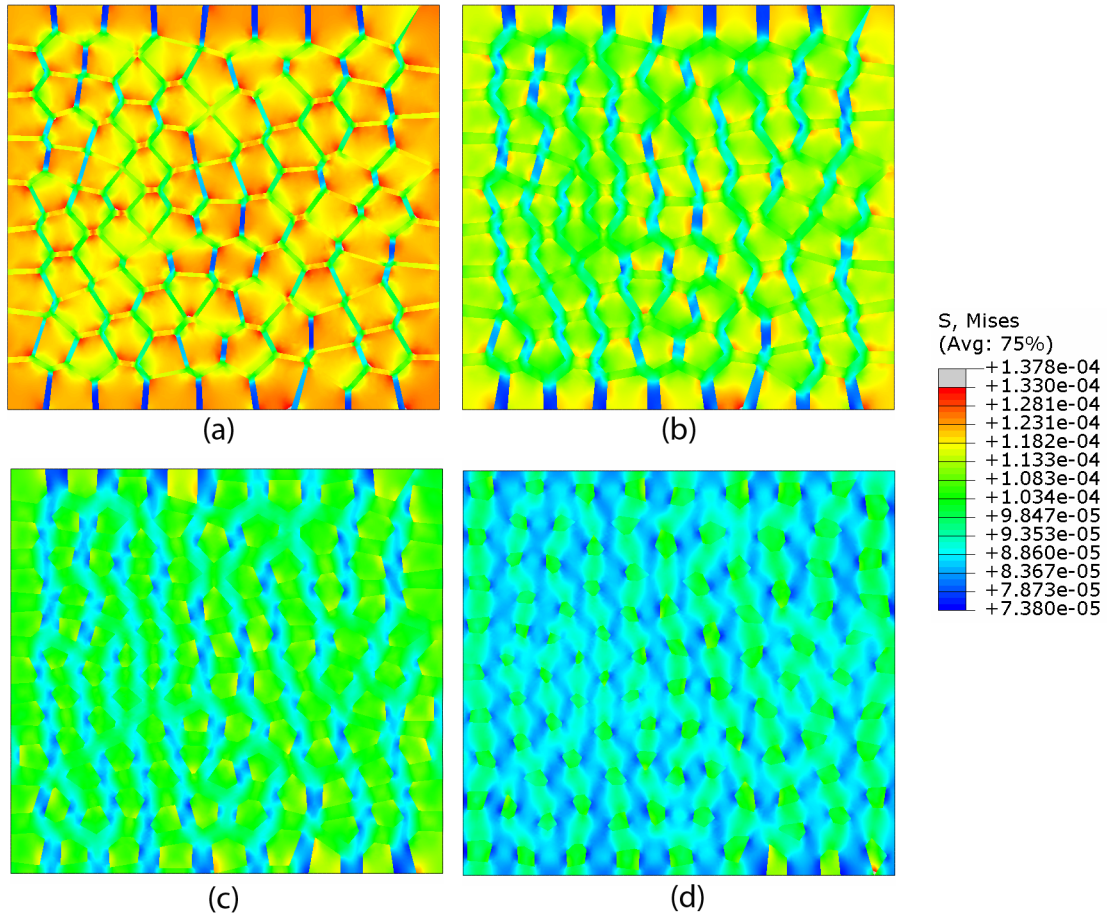
Figure 5.11: Deformed models with 100 grains and varying crystal size and crystalline volume fractions; (a) 80%, (b) 60%, (c) 40% and (d) 20%. The grain sizes are listed in table 5.1
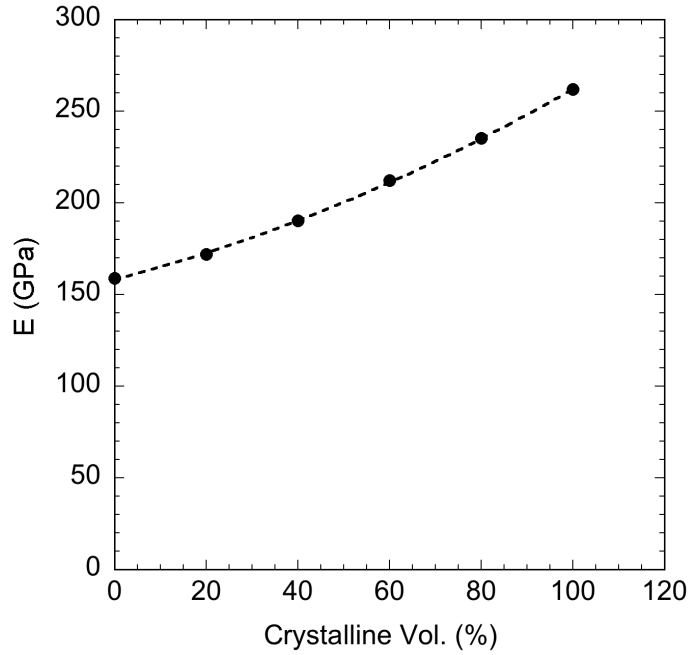
Figure 5.12: Elastic modulus determined for the 100 grain models varying crystal size and crystalline volume fractions, as a function of the crystalline volume fraction.

ulus obtained from these models as a function of crystalline volume fraction. Unlike in the earlier case, here the elastic modulus is truly a function of crystalline volume fraction alone since the grain size in all models was the same. The polycrystalline material can also be considered as a composite with the amorphous region analogous to the matrix and grains being the reinforcing media. In the light of this, a simple estimate of variation of modulus can be determined using rule of mixtures. These estimates typically mark the upper and lower bound for the modulus. The modulus determined by rule-of-mixtures (ROF) and inverse-rule-of-mixtures (IROF) are also shown in Figure 5.14. The effective modulus estimated from the simple FEM models developed here lie within these bounds. Thus these models can capture the effective elastic modulus of a polycrystalline material purely as a function of crystalline volume fraction.

The third set of models was aimed at investigating the effect of grain size alone on the effective modulus of the polycrystalline composite. The deformed models with

76

S, Mises
(Avg: 75%)
+1.378e-04
+1.330e-04
+1.281e-04
+1.231e-04
+1.182e-04
+1.133e-04
+1.083e-04
+1.034e-04
+9.847e-05
+9.353e-05
+8.860e-05
+8.367e-05
+7.873e-05
+7.380e-05
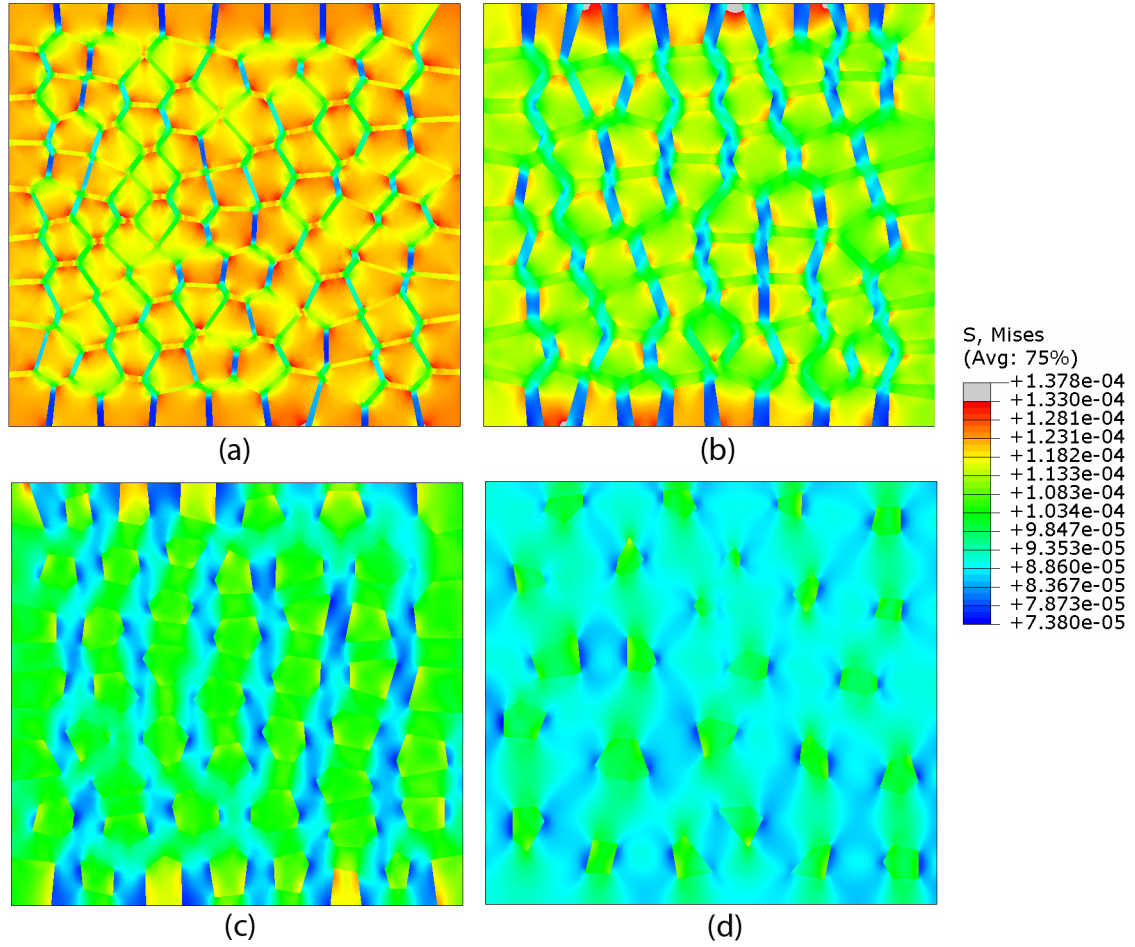
Figure 5.13: Deformed models with grain size of 10 nm in all cases and with different crystalline volume fractions; (a) 80%, (b) 60%, (c) 40% and (d) 20%.
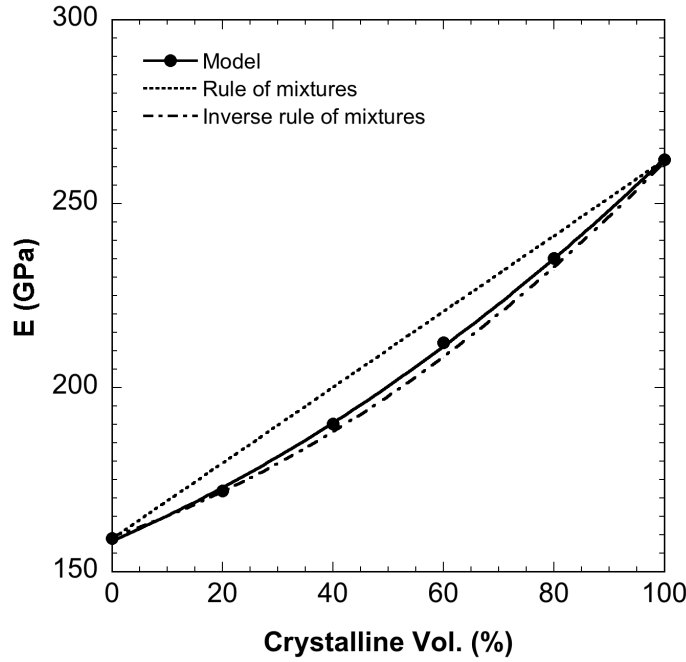
Figure 5.14: Elastic modulus determined for the models with 10 nm, as a function of the crystalline volume fraction.

80% crystalline volume fraction in each and containing grains of average sizes of 5, 10, and 15 nm is shown in figure 5.15. The global size of the square was set to 50 nm × 50 nm in order to achieve 5 nm grains with 100 grains. Table 5.4 lists the effective modulus obtained from these models as a function of grain size.

From the values listed in table 5.4 it is clear that such a simple finite element models fails to capture any effect of grain size on the mechanical properties. Several phenomena such as grain strengthening at smaller grain sizes due to dislocation movement and pile-up, intragranular plasticity, grain boundary slipping, etc need to be accounted for in order to capture any effect of grain size on the mechanical properties. Nevertheless, the simple FEM model developed here provides a frame work and the requisite first step towards such a model.
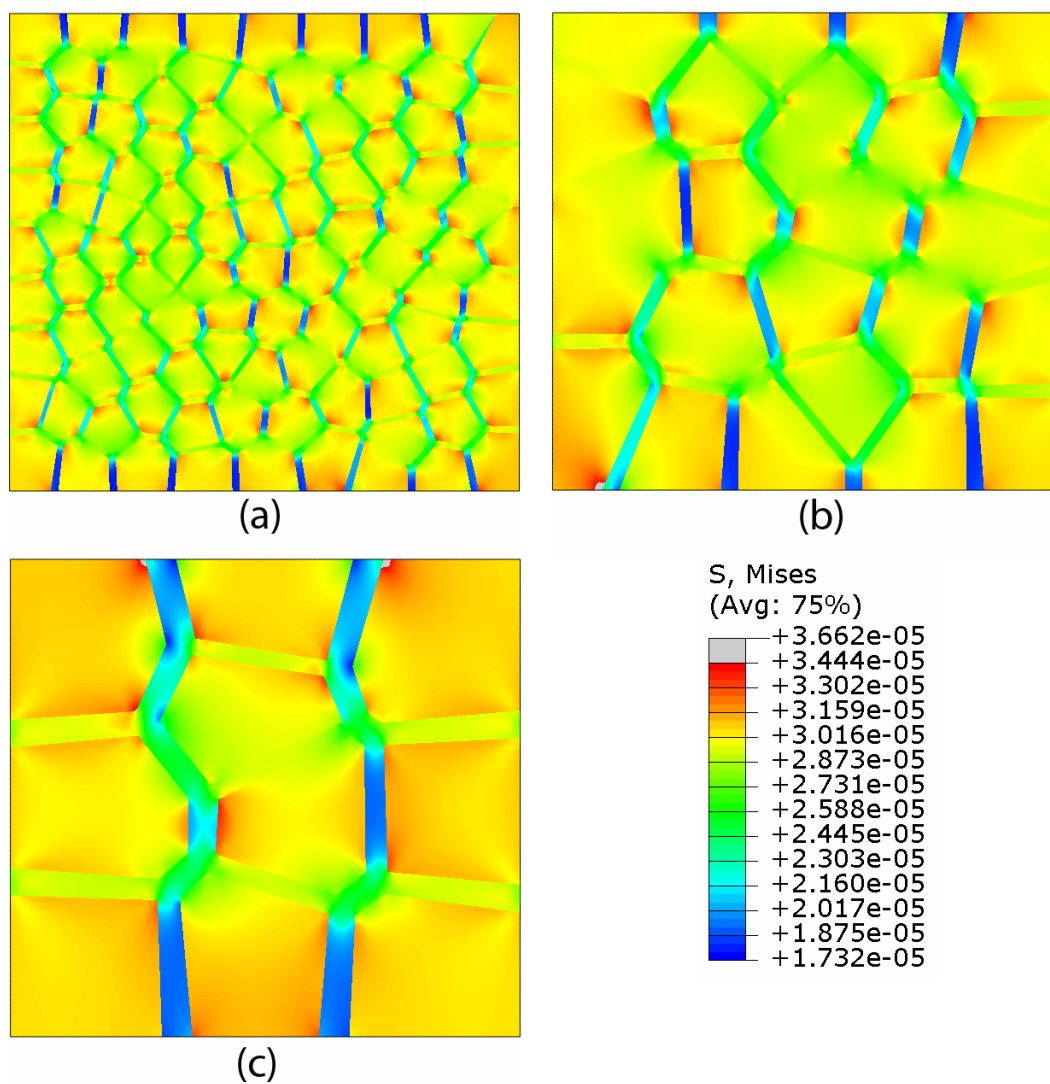
Figure 5.15: Deformed Models, with 80% crystalline volume fractions in each case, and average grain size varying from 5 nm to 15 nm.

No. of grains	Avg. grain size	Crystalline vol (%)	E (GPa)
100	5 nm	80	235.17
25	10 nm	80	234.91
10	15 nm	80	235.83

Table 5.4: Elastic modulus obtained for models with the same crystalline volume fraction of 80% and having different grain sizes.

CHAPTER 6

Conclusions and Future Work

Based on the work reported in this investigation, the following conclusions are drawn:

1. The use of high pressure and/or high temperature processing is a basic requirement for traditional powder-based fabrication of ceramic components. These processing conditions not only increase the energetic requirements but also place limits on the types of materials that can be produced. Despite several different techniques developed to produce ceramics, the search for a technique that offers a combination of advantages such as low temperature processing, low costs, ability to fabricate complex shapes, high density yields, and microstructure control, still continues. Polymer derived ceramics are an attractive alternative because of pressure-less and lower temperature processing and near-net shape fabrication. Control over the microstructure of SiC formed by pyrolysis of pre-ceramic polymer precursor is relatively easy and is presented by fabrication of amorphous and nanocrystalline SiC.

2. The chemical and structural changes during the pyrolysis of allylhydridopolycarbosilane were studied by tracking mass loss, density changes, chemical bonding, and evolution of microstructure up to $1650\,°C$. A hydrogen-free ceramic yield of 72–74% was obtained in the range $900\,°$–$650\,°C$ using very slow heating rate of $4\,°C/min$. IR spectroscopy observations revealed presence of hydrogen in SiC pyrolyzed at $900\,°C$. They also provided insight into the decomposition of polymer precursor by dissociation of Si–H and C–H bonds along with the evolution of a Si–C network.

3. The onset of crystallization was seen to occur close to $1100\,°C$ leading to the formation of amorphous/nanocrystalline SiC. Crystallite size, as estimated from powder diffraction patterns, was found to be in tens of nanometers at $1650\,°C$. Clear evidence of nanocrystalline SiC formed with different crystal sizes at different processing temperatures was seen through transmission electron microscopy along with a study of selected area electron diffraction.

4. Nanocrystalline SiC, like other nanocrystalline ceramics, is expected to have superior properties. Significant improvement in mechanical properties were seen after the onset of crystallization in SiC. Mechanical properties of amorphous and amorphous/nano-crystalline SiC derived from AHPCS, pyrolyzed to different temperatures and different hold times at final temperature, were characterized in terms of elastic modulus and hardness by instrumented nanoindentation. The mechanical properties were influenced by both processing temperature and hold durations. The highest values for hardness, of around 30 GPa, were seen for the material processed at $1150\,°C$ for a hold time of 1 h. These were about 52% higher than the lowest value, which was seen for materials processed at $1650\,°C$ with a hold time of 4 h. Similarly highest modulus values, observed for the same samples, were about 218 GPa, which were 37% higher than the lowest value which were seen for materials processed with 2 min hold time at $900\,°C$. Thus, an optimum processing temperature of $1150\,°C$ and hold duration of 1 hour gave the best values for hardness and modulus. Thus, there is some measure of understanding into the processing–property relationship gained from these observations. However, information on crystal size and degree of crystallinity for SiC processed to different temperatures and hold times is desirable, but could not be acquired during this study. Such information would give further insight into the processing–structure–property relationship.

5. Development of a simple elastic–elastic finite element model was undertaken. Polycrystalline SiC was modeled, using Voronoi tessellation, as a composite with randomly distributed, purely crystalline SiC grains in an amorphous SiC matrix. Both the intra-granular and inter-granular regions were modeled as purely elastic. This is an approximation made to derive the purely elastic response of the polycrystalline model. Models were created with different number of grains (10–100), varying grain sizes (5 nm–15 nm) and different crystalline volume fractions (80–20%). Elastic modulus determined from the model scaled with the crystalline volume fraction, whereas the models failed to capture any influence of the grain size on the modulus.

While a good deal of insight was gained into the polymer–ceramic conversion of AHPCS and further evolution of amorphous and nanocrystalline SiC, there are some aspects of these phenomena that are worth probing further. Studying these processes from the kinetics approach could lead to further understanding of processing–structure relationships and could help in designing a process that could lead to further improved mechanical properties. Study of the kinetics of polymer–ceramic conversion could help gain a better control over the rate of nucleation and grain growth, which could in turn help in fabrication of functionally graded and tailored nanocomposites. There is much room for further investigation into the processing–structure relationship through experimentation. Rietveld analysis of powder diffraction data can provide an in-depth characterization of the crystal structure of SiC formed by the pyrolysis of preceramic polymer. Information on degree of crystallinity and crystal size as a function of processing parameters would also help characterize the processing–structure relationships. In terms of modeling, a model that could capture the mesoscale phenomena such as grain boundary sliding and intergranular plasticity would greatly help in understanding the properties of nanocrystalline ceramics such as n–SiC. Using the simple elastic–elastic polycrystalline model developed in this

work, further effort can be directed towards incorporating more complex constitutive relations, that could lead to better approximation of the properties. In the light of this, another approach that has potential is the material point method. Using the MPM method, phenomena at the scale which is of the order of the grain size can be studied, which would bridge the gap of current level of understanding that has been gained at the atomistic level, by MD studies, and at the continuum level, by finite element method studies.

BIBLIOGRAPHY

[1] Rice, R., 1990. "Ceramic Processing - An Overview". *AICHE Journal,* **36**(4), pp. 481–510.

[2] Matijevic, E., 1986. "Monodispersed Colloids - Art and Science". *Langmuir,* **2**(1), pp. 12–20.

[3] Ring, T., 1988. "Continuous Production of Narrow Size Distribution Sol-gel Ceramic Powders". *Abstracts of Papers of the American Chemical Society,* **195**, pp. 27.

[4] Okamura, H., and Bowen, H., 1986. "Preparation of Alkoxides for the Synthesis of Ceramics". *Ceramics International,* **12**(3), pp. 161–171.

[5] Kaito, C., Fujita, K., and Shiojiri, M., 1976. "Growth of CDS Smole Particles Prepared by Evaporation in Inert-gases". *Journal of Applied Physics,* **47**(12), pp. 5161–5166.

[6] , 1984. Some Common Aspects of the Formation of Nonoxide Powders by the Vapor Reaction Method., Vol. 17, Plenum Press, New York, NY, USA.

[7] Clark, T. J., Arons, R. M., Stamatoff, J. B., and Rabe, J., 1985. "Thermal degradation of Nicalon SiC fibers". *Ceramic Engineering and Science Proceedings,* **6**, pp. 576–588.

[8] Washburn, M., and Coblenz, W., 1988. "Reaction-formed Ceramics". *American Ceramic Society Bulletin,* **67**(2), pp. 356.

[9] Chiang, Y., Messner, R., Terwilliger, C., and Behrendt, D., 1991. "Reaction-formed Silicon Carbide". *Materials Science and Engineering A - Structural Materials - Properties, Microstructure and Processing,* **144**, pp. 63–74.

[10] Popper, P., 1960. "The preparation of dense self-bonded silicon carbide". *Special Ceramics*, p. 209.

[11] Hillig, W. B., Mehan, R. L., Morelock, C. R., DeCarlo, V. J., and Laskow, W., 1975. "Silicon/Silicon Carbide Composites.". *American Ceramic Society Bulletin,* **54**(12), pp. 1054–1056.

[12] Mehan, R. L., 1978. "Effect of SiC Content and Orienctation on Properties of Si/SiC Ceramic Composite.". *Journal of Materials Science,* **13**(2), pp. 358–366.

[13] Binner, J. G. P., ed., 1990. *Advanced Ceramic Processing and Technology,* Vol. 1. Noyes Publications, Park Ridge, New Jersey, USA.

[14] S, Goela, J., and L., Taylor, R., 1988. "Monolithic material fabrication by chemical vapour deposition". *Journal of Materials Science,* **23**(12), pp. 4331 – 4339.

[15] Funk, R., Schachner, H., Triquet, C., Kornmann, M., and Lux, B., 1976. "Coating of Cemented Carbide Cutting Tools with Alumina by Chemical Vapor Deposition". *Journal of the Electrochemical Society,* **123**(2), pp. 285–289.

[16] Lindstrom, J., and Johannesson, R., 1976. "Nucleation of Al-20-3 Layers on Cemented Carbide Tools". *Journal of the Electrochemical Society,* **123**(4), pp. 555–559.

[17] Katto, H., and Koga, Y., 1971. "Preparation and Properties of Aluminum Oxide Films Obtained by Glow Discharge Technique". *Journal of the Electrochemical Society,* **118**(10), pp. 1619–&.

[18] Pierson, H. O., 1999. *Handbook of Chemical Vapor Deposition (CVD): Principles, Technology and Applications.* Noyes Publications.

[19] Yang, Q., 1999. "Composite Sol-Gel Ceramics". PhD thesis, The University of British Columbia, Canada.

[20] F, Becher, P., H, Sommers, J., A, Bender, B., and A., MacFarlane, B., 1978. "Ceramics Sintered Directly froom Sol-gels.". *Materials Science Research,* **11**, pp. 79 – 86.

[21] L, Hench, L., G, O., and L., Nogues, J., 1986. "Role of Chemical Additives in Sol-gel Processing.". *Materials Research Society Symposia Proceedings,* **73**, pp. 35 – 47.

[22] Barrow, D., Petroff, T., and Sayer, M., 1995. "Thick ceramic coatings using a sol gel based ceramic-ceramic 0-3 composite". *Surface & Coatings Technology,* **76**(1-3), pp. 113–118.

[23] Xu, Y., Nakahira, A., and Niihara, K., 1994. "Characteristics of Al2O3-SiC Nanocomposite Prepared by Sol-gel Processing". *Nippon Seramikkusu Kyokai Gakujutsu Ronbunshi - Journal of the Ceramic Society of Japan,* **102**(3), pp. 312–315.

[24] Brook, R., 1995. *Processing of Ceramics, Part II. Materials Science and Technology: A Comprehensive Treatment.*, Vol. 17B. John Wiley & Son: New York.

[25] A., P. R. "Preceramic Polymer Derived Si3N4 Composites with Continuous Fiber Reinforcement". *apability Brochures for: SwRI Mechanical and Materials Engineering.*

[26] Greil, P., 2000. "Polymer derived engineering ceramics". *Advanced Engineering Materials,* **2**(6), pp. 339–348.

[27] Riedel, R., Mera, G., Hauser, R., and Klonczynski, A., 2006. "Silicon-based polymer-derived ceramics: Synthesis properties and applications - A review". *Journal of the Ceramic Society of Japan,* **114**(1330), pp. 425–444.

[28] Lipowitx, J., 1991. "Polymer-Derived Ceramic Fibers". *American Ceramic Society Bulletin,* **70**(12), pp. 1888–1894.

[29] He, J., Scarlete, M., and Harrod, J., 1995. "Silicon-Nitride and Silicon Carbonitride by the Pyrolysis of Poly(Methylsiladiazane)". *Journal of the American Ceramic Society,* **78**(11), pp. 3009–3017.

[30] Laine, R., and Babonneau, F., 1993. "Preceramic Polymer routes to Silicon-Carbide". *Chemistry of Materials,* **5**(3), pp. 260–279.

[31] Wideman, T., Remsen, E., Cortez, E., Chlanda, V., and Sneddon, L., 1998. "Amine-modified polyborazylenes: Second-generation precursors to boron nitride". *Chemisty of Materials,* **10**(1), pp. 412–421.

[32] Sato, K., Tezuka, A., Funayama, O., Isoda, T., Terada, Y., Kato, S., and Iwata, M., 1999. "Fabrication and pressure testing of a gas-turbine component manufactured by a preceramic-polymer-impregnation method". *Composites Science and Technology,* **59**(6), pp. 853–859.

[33] Shah, S., and Raj, R., 2002. "Mechanical properties of a fully dense polymer derived ceramic made by a novel pressure casting process". *Acta Materialia,* **50**(16), pp. 4093–4103.

[34] Tredway, W., 1998. "Materials science - Toughened ceramics". *Science,* **282**(5392), pp. 1275–1275.

[35] Schick, H. L., 1966. "Thermodynamics of Certain Refractory Comounds". *Academic Press,* **1**, pp. 1–402.

[36] Munro, R., 1997. "Material properties of a sintered alpha-SiC". *Journal of Physical and Chemical Reference Data,* **26**(5), pp. 1195–1203.

[37] Hinoki, T., and Kohyama, A., 2005. "Current status of SiC/SiC composites for nuclear applications". *Annales de Chimie: Science des Materiaux,* **30**(6), pp. 659 – 671.

[38] Alkan, Z., Kugeler, K., Kaulbarsch, R., and Manter, C., 2001. "Silicon Carbide Encapsulated Fuel Pellets for Light Water Reactors". *Progress in Nuclear Energy,* **38**(3-4), pp. 411 – 414.

[39] Lee, Y. W., Lee, S., Kim, H., Joung, C., and Degueldre, C., 2003. "Study on the mechanical properties and thermal conductivity of silicon carbide-, zirconia- and magnesia aluminate-based simulated inert matrix nuclear fuel materials after cyclic thermal shock". *Journal of Nuclear Materials,* **319**, pp. 15 – 23.

[40] Lewinsohn, A. C., Jones, H. R., Colombo, P., and Riccardi, B., 2002. "Silicon carbide-based materials for joining silicon carbide composites for fusion energy applications". *Journal of Nuclear Materials,* **307-311**(2 SUPPL), pp. 1232 – 1236.

[41] Senor, D. J., Youngblood, G. E., Brimhall, J. L., Trimble, D. J., Newsome, G., and Woods, J., 1996. "Dimensional stability and strength of neutron-irradiated SiC-based fibers". *Fusion Technology,* **30**(3), pp. 956–968.

[42] Hollenberg, G. W., Henager, C. H., Youngblood, G. E., Trimble, D. J., Simonson, S. A., Newsome, G. A., and Lewis, E., 1995. "The effect of irradiation on the stability and properties of monolithic silicon-carbide and SiC_f/SiC composites up to 25 dpa". *Journal of Nuclear Materials,* **219**, pp. 70–86.

[43] Snead, L. L., Osborne, M., and More, K. L., 1995. "Effects of radiation on SiC-based Nicalon fibers". *Journal of materials research,* **10**(3), pp. 736–747.

[44] Snead, L. L., Katoh, Y., Kohyama, A., Bailey, J., Vaughn, N., and Lowden, R., 2000. "Evaluation of neutron irradiated near-stoichiometric silicon carbide fiber composites". *Journal of Nuclear Materials,* **283**, pp. 551–555.

[45] Newsome, G., Snead, L., Hinoki, T., Katoh, Y., and Peters, D., 2007. "Evaluation of neutron irradiated silicon carbide and silicon carbide composites". *Journal of Nuclear Materials,* **371**(1-3), pp. 76–89.

[46] Katoh, Y., Snead, L. L., Henager, C. H., Hasegawa, A., Kohyama, A., Riccardi, B., and Hegeman, H., 2007. "Current status and critical issues for development of SiC composites for fusion applications". *Journal of Nuclear Materials,* **367**, pp. 659–671.

[47] Singh, A. K., Zunjarrao, S. C., and Singh, R. P., 2008. "Processing of uranium oxide and silicon carbide based fuel using polymer infiltration and pyrolysis". *in review: Journal of Nuclear Materials.*

[48] Wan, J., Gasch, Matthew, J., and Mukherjee, Amiya, K., 2002. "Silicon nitride/silicon carbide nanocomposites from polymer precursor". *Ceramic Engineering and Science Proceedings,* **23**(4), pp. 665–672.

[49] Danko, G., Silberglitt, R., Colombo, P., Pippel, E., and Woltersdorf, J., 2000. "Comparison of microwave hybrid and conventional heating of preceramic polymers to form silicon carbide and silicon oxycarbide ceramics". *Journal of the American Ceramic Society,* **83**(7), pp. 1617–1625.

[50] Mitchell, Brian, S., Zhang, H., Maljkovic, N., Ade, M., Kurtenbach, D., and Muller, E., 1999. "Formation of nanocrystalline silicon carbide powder from chlorine-containing polycarbosilane precursors". *Journal of the American Ceramic Society,* **82**(8), pp. 2249–2251.

[51] Szlufarska, I., Nakano, A., and Vashishta, P., 2005. "A crossover in the mechanical response of nanocrystalline ceramics". *Science,* **309**(5736), pp. 911–914.

[52] Veprek, S., Nesladek, P., Niederhofer, A., Glatz, F., Jilek, M., and Sima, M., 1998. "Recent progress in the superhard nanocrystalline composites: towards their industrialization and understanding of the origin of the superhardness". *Surface & Coatings Technology,* **109**(1-3), pp. 138–147.

[53] Zhao, Y., Qian, J., Daemen, L., Pantea, C., Zhang, J., Voronin, G., and Zerda, T., 2004. "Enhancement of fracture toughness in nanostructured diamond-SiC composites". *Applied Physics Letters,* **84**(8), pp. 1356–1358.

[54] Liao, F., Girshick, S., Mook, W., Gerberich, W., and Zachariah, M., 2005. "Superhard nanocrystalline silicon carbide films". *Applied Physics Letters,* **86**(17).

[55] Madar, R., 2004. "Materials science - Silicon carbide in contention". *Nature,* **430**(7003), pp. 974–975.

[56] Vassen, R., and Stover, D., 1999. "Processing and properties of nanograin silicon carbide". *Journal of the American Ceramic Society,* **82**(10), pp. 2585–2593.

[57] Tymiak, N., Iordanoglou, D. I., Neumann, D., Gidwani, A., Fonzo, F. D., Fan, M. H., Rao, N., Gerberich, W. W., McMurry, P. H., Heberlein, J. V. R., and Girshick, S. L.", 1999.". *Proceedings of the 14th International Symposium on Plasma Chemistry,* **3**.

[58] Richter, V., and Von Ruthendorf, M., 1999. "On hardness and toughness of ultrafine and nanocrystalline hard materials". *Internaltion Journal of Refractory Metals & Hard Materials,* **17**(1-3), pp. 141–152.

[59] Kroll, P., 2005. "Modelling polymer-derived ceramics". *Journal of the European Ceramic Society,* **25**(2-3), pp. 163–174.

[60] Kulikovsky, V., Vorlicek, V., Bohac, P., Kurdyumov, A., and Jastrabik, L., 2004. "Mechanical properties of hydrogen-free a-C : Si films". *Diamond and Related Materials,* **13**(4-8), pp. 1350–1355.

[61] Amkreutz, M., and Frauenheim, T., 2002. "Understanding precursor-derived amorphous Si-C-N ceramics on the atomic scale". *Physical Review B,* **65**(13), p. 134113.

[62] Matsunaga, K., Iwamoto, Y., Fisher, C., and Matsubara, H., 1999. "Molecular dynamics study of atomic structures in amorphous Si-C-N ceramics". *Journal of the Ceramic Society of Japan,* **107**(11), pp. 1025–1031.

[63] Hall, E., 1951. "The Deformation and Ageing of Mild Steel. 3. Discussion of Results". *Proceedings of the Physical Society of London Section B,* **64**(381), pp. 747–753.

[64] Petch, N., 1953. "The Clevage Strength of Polycrystals". *Journal of the Iron and Steel Institute,* **174**(1), pp. 25–28.

[65] Lu, Y., and Liaw, P., 2001. "The mechanical properties of nanostructured materials". *JOM-Journal of the Minerals, Metals & Materials Society,* **53**(3), pp. 31–35.

[66] Chokshi, A., Rosen, A., Karch, J., and Gleiter, H., 1989. "On the Validity of the Hall-Petch Relationship in Nanocrystalline Materials". *Scripta Metallurgica,* **23**(10), pp. 1679–1683.

[67] Schiotz, J., Di Tolla, F., and Jacobsen, K., 1998. "Softening of nanocrystalline metals at very small grain sizes". *Nature,* **391**(6667), pp. 561–563.

[68] Carsley, J., Ning, J., Milligan, W., Hackney, S., and AIFANTIS, E., 1995. "A Simple, Mixtures-Based Model for the Grain-Size Dependence of Strength in Nanophase Metals". *Nanostructured Materials,* **5**(4), pp. 441–448.

[69] Elsherik, A., Erb, U., Palumbo, G., and Aust, K., 1992. "Deviations from Hall-Petch Behavior in As-Prepared Nanocrystalline Nickel". *Scripta Metallurgica ET Materialia,* **27**(9), pp. 1185–1188.

[70] Fourgere, G., Weertman, J., Siegel, R., and Kim, S., 1992. "Grain-Size Dependent Hardening and Softening of Nanocrystalline Cu and Pd". *Scripta Metallurgica ET Materialia,* **26**(12), pp. 1879–1883.

[71] Nieman, G., Weertman, J., and Siegel, R., 1991. "Mechanical-Behaviour of Nanocrystalline Cu and Pd". *Journal of Materials Research,* **6**(5), pp. 1012–1027.

[72] Sanders, P., Youngdahl, C., and Weertman, J., 1997. "The strength of nanocrystalline metals with and without flaws". *Materials Science and Engineering A-Structure Properties, Microstructure and Processing,* **234**, pp. 77–82.

[73] Siegel, R., 1994. "What do we really know about the atomic-scale structures of Nanophase Materials". *Journal of Physics and Chemistry of Solids,* **55**(10), pp. 1097–1106.

[74] Yip, S., 1998. "Nanocrystals - The strongest size". *Nature,* **391**(6667), pp. 532–533.

[75] Veprek, S., and Argon, A., 2002. "Towards the understanding of mechanical properties of super- and ultrahard nanocomposites". *Journal of Vaccum Science & Technology B,* **20**(2), pp. 650–664.

[76] Kroll, P., 2003. "Modelling and simulation of amorphous silicon oxycarbide". *Journal of Materials Chemistry,* **13**(7), pp. 1657–1668.

[77] Umesaki, N., Hirosaki, N., and Hirao, K., 1992. "Structural Characterization of Amorphous-Silicon Nitride by Molecular-Dymanics Simulation". *Journal of Non-Crystalline Solids,* **150**(1-3), pp. 120–125.

[78] de Brito Mota, F., Justo, J., and Fazzio, A., 1998. "Structural properties of amorphous silicon nitride". *Physical Review B,* **58**(13), pp. 8323–8328.

[79] Verbeek, W., 1973. *Ger. Pat. No. 2218960 (U.S. Pat. No. 38533567).*

[80] Verbeek, W., and Winter, G., 1974. *Ger. Pat. No. 2236078.*

[81] Yajima, S., Hayashi, J., and Omori, M., 1975. "Continuous Silicon-Carbide Fiber of High-Tensile Strength". *Journal of Physical Chemistry B*(9), pp. 931–934.

[82] Jones, R. H., and Henager Jr., C. H., 2005. "Subcritical crack growth processes in SiC/SiC ceramic matrix composites". *Journal of the European Ceramic Society,* **25**(10 SPEC ISS), pp. 1717 – 1722.

[83] Pouskouleli, G., 1989. "Metallorganic Compounds as Preceramic Materials.1. Non-Oxide Ceramics". *Ceramics International,* **15**(4), pp. 213–229.

[84] Peuckert, M., Vaahs, T., and Bruck, M., 1990. "Ceramics from Organomettalic Polymers". *Advanced Materials,* **2**(9), pp. 398–404.

[85] Procopio, L., and Berry, D., 1991. "Dehydrogenative Coupling of Trialkylsilanes Mediated by Ruthenium Phosphine Complexes - Catalytic Synthesis of Carbosilanes". *Journal of the American Ceramic Society,* **113**(10), pp. 4039–4040.

[86] Whitmarsh, C., and Interrante, L., 1991. "Synthesis and Structure of a Highly Branched Polycarbosilane Derived from (Chloromethyl)trichlorosilane". *Organometaillics,* **10**(5), pp. 1336–1344.

[87] Wu, H., and Interrante, L., 1992. "Preparation of Poly(dichlorosilaethylene) and Poly(silaethylene) via Ring-Opening Polymerization". *Macromolecules,* **25**(6), pp. 1840–1841.

[88] BIirot, M., Pillot, J., and Dunogues, J., 1995. "Comprehensive Chemistry of Polycarbosilanes, Polysilazanes and Polycarbosilazanes as Precursors of Ceramics". *Chemical Reviews,* **95**(5), pp. 1443–1477.

[89] Aldinger, F., Weinmann, M., and Bill, J., 1998. "Precursor-derived Si-B-C-N ceramics". *Puer and Applied Chemistry,* **70**(2), pp. 439–448.

[90] Kipping, F., 1924. "Organic derivatives of silicon Part XXX Complex silicohydrocarbons [SiPh2]n". *Journal of the Chemical Society,* **125**, pp. 2291–2297.

[91] Burkhard, C. A., 1949. "Polydimethylsilanes". *Journal of the American Chemical Society,* **71**(3), pp. 963–964.

[92] Seyferth, D., Wood, T., Tracy, H., and Robison, J., 1992. "Near- Stoichiometric Silicon-Carbide from an Economical Poysilane Precursor". *Journal of the American Ceramic Society,* **75**(5), pp. 1300–1302.

[93] Walker, B., Rice, R., Becher, P., Bender, B., and Coblenz, W., 1983. "Preparation and Properties of Monolithic and Composite Ceramics Produced by Polymer Pyrolysis". *American Ceramic Society Bulletin,* **62**(8), pp. 916–923.

[94] West, R., David, L., Djurovich, P., Yu, H., and Sinclair, R., 1983. "Polysiastyrene - Phenylmethylsilane - Dimethylsilane Co-Polymers as Precursors to Silicon-Carbide". *American Ceramic Society Bulletin,* **62**(8), pp. 899–903.

[95] Seyferth, D., and F., Y. Y., 1987. "Method for forming new preceramic polymers containing silicon". *Massachusetts Institute of Technology (Cambridge, MA)*.

[96] Interrante, L. V., Whitmarsh, C., Sherwood, W., Wu, H.-J., Lewis, R., and Maciel, G., 1994. "High yield polycarbosilane precursors to stoichiometric SiC. Synthesis, pyrolysis and application". *Proceedings of the 1994 MRS Spring Meeting, Apr 4-8 1994, San Francisco, CA, USA,* **346**, pp. 593–603.

[97] Berbon, Min, Z., Dietrich, Donald, R., Marshall, David, B., and Hasselman, D., 2001. "Transverse thermal conductivity of thin C/SiC composites fabricated by slurry infiltration and pyrolysis". *Journal of the American Ceramic Society,* **84**(10), pp. 2229–2234.

[98] Dong, S., Katoh, Y., Kohyama, A., Schwab, S., and Snead, L., 2002. "Microstructural evolution and mechanical performances of SiC/SiC composites by polymer impregnation/microwave pyrolysis (PIMP) process". *Ceramics International,* **28**(8), pp. 899–905.

[99] Interrante, L., Jacobs, J., Sherwood, W., and Whitmarsh, C., 1997. "Fabrication and properties of fiber- and particulate-reinforced SiC matrix composites obtained with (A)HPCS as the matrix source". *Key Engineering Materials,* **127-131**(Pt 1), pp. 271–278.

[100] Moraes, Kevin, V., and Interrante, Leonard, V., 2003. "Processing, fracture toughness, and vickers hardness of allylhydridopolycarbosilane-derived silicon carbide". *Journal of the American Ceramic Society,* **86**(2), pp. 342–346.

[101] Whitmarsh, C. K., and Interrante, L. V., 1992. "Carbosilane polymer precursors to silicon carbide ceramics". *Rensselaer Polytechnic Institute (Troy, NY)*.

[102] Rushkin, I., Shen, Q., Lehman, S., and Interrante, L., 1997. "Modification of a hyperbranched hydridopolycarbosilane as a route to new polycarbosilanes". *Macromolecules,* **30**(11), pp. 3141 – 3146.

[103] Interrante, L., Moraes, K., Liu, Q., Lu, N., Puerta, A., and Sneddon, L., 2002. "Silicon-based ceramics from polymer precursors". *Pure and Applied Chemistry,* **74**(11), pp. 2111–2117.

[104] Zheng, J., and Akinc, M., 2001. "Green state joining of SiC without applied pressure". *Journal of the American Ceramic Society,* **84**(11), pp. 2479–2483.

[105] Solomon, Alvin, A., Fourcade, J., Lee, S.-G., Kuchibhotla, S., Revankar, S., Latta, R., Holman, Peter, L., and McCoy, J. K., 2004. "The polymer impregnation and pyrolysis method for producing enhanced conductivity LWR fuels". *Proceedings of the 2004 International Meeting on LWR Fuel Performance, Orlando, Florida, September 19-22, 2004, American Nuclear Society, La Grange Park, IL 60526, United States, pp. 146155. Paper 1028.,* pp. 146–155.

[106] Ozcivici, E., and Singh, R., 2005. "Fabrication and characterization of ceramic foams based on silicon carbide matrix and hollow alumino-silicate spheres". *Journal of the American Ceramic Society,* **88**(12), pp. 3338–3345.

[107] Singh, A. K., Zunjarrao, S. C., and Singh, R. P., 2006. "Silicon Carbide and Uranium Oxide based Composite Fuel Preparation using Polymer Infiltration and Pyrolysis". *Proceedings of ICONE 14, 14th International Conference On Nuclear Engineering, Miami, USA, July 17-20, 2006.*

[108] VanLandingham, Mark, R., 2003. "Review of instrumented indentation". *Journal of Research of the National Institute of Standards and Technology,* **108**(4), pp. 249–265.

[109] Nechanicky, M., Chew, K., Sellinger, A., and Laine, R., 2000. "alpha-Silicon carbide/beta-silicon carbide particulate composites via polymer infiltration and pyrolysis (PIP) processing using polymethylsilane". *Journal of the European Ceramic Society,* **20**(4), pp. 441–451.

[110] Kerdiles, S., Rizk, R., Gourbilleau, F., Perez-Rodriguez, A., Garrido, B., Gonzalez-Varona, O., and Morante, J., 2000. "Low temperature direct growth of nanocrystalline silicon carbide films". *Materials Science and Engineering B-Solid State Materials for Advanced Technology,* **69**, pp. 530–535.

[111] Zhang, H., and Xu, Z., 2002. "Microstructure of nanocrystalline SiC films deposited by modified plasma-enhanced chemical vapor deposition". *Optical Materials,* **20**(3), pp. 177–181.

[112] Ying, Y., Gu, Y., Li, Z., Gu, H., Cheng, L., and Qian, Y., 2004. "A simple route to nanocrystalline silicon carbide". *Journal of Solid State Chemistry,* **177**(11), pp. 4163–4166.

[113] Kotani, M., Inoue, T., Kohyama, A., Katoh, Y., and Okamura, K., 2003. "Effect of SiC particle dispersion on microstructure and mechanical properties of polymer-derived SiC/SiC composite". *Materials Science and Engineering A,* **357**(1-2), pp. 376 – 385.

[114] "ASTM-C830-00". *American Society for Testing and Materials, West Conshohocken, PA.*

[115] Ovri, J. E. O., 2000. "A parametric study of the biaxial strength test for brittle materials". *Materials Chemistry and Physics,* **66**(1), pp. 1 – 5.

[116] Lee, M.-S., and Bent, S. F., 1997. "Bonding and thermal reactivity in thin a-SiC:H films grown by methylsilane CVD". *Journal of Physical Chemistry B,* **101**(45), pp. 9195 – 9205.

[117] Hurwitz, F. I., Kacik, T. A., Bu, X.-Y., Masnovi, J., Heimann, P. J., and Beyene, K., 1994. "Conversion of polymers of methyl- and vinylsilane to SiC ceramics". *Journal of Engineering and Applied Science,* **346**, pp. 623 – 628.

[118] Wang, X., Zunjarrao, S. C., Hui, Z., and P, S. R., 2006. "Advanced Process Model for Polymer Pyrolysis and Uranium Ceramic Material Processing". *14th International Conference on Nuclear Engineering.*

[119] Cullity, B. D., 1978. *Elements of X-ray Diffraction.* Addison-Wesley Publishing Co. Unc., London.

[120] Cheary, R. W., and Coelho, A. A., 1996. "Programs XFIT and FOURYA, deposited in CCP14 Powder Diffraction Library, Engineering and Physical Sciences Research Council, Daresbury Laboratory, Warrington, England.".

[121] Williams, D., and Carter, C. B., 1996. *Transmission Electron Microscopy: A Textbook for Materials Science.* Kluwer Academic / Plenum Publishers, New York.

[122] Meyers, M., Mishra, A., and Benson, D., 2006. "Mechanical properties of nanocrystalline materials". *Progress in Materials Science,* **51**(4), pp. 427–556.

[123] Fu, H., Benson, D., and Meyers, M., 2001. "Analytical and computational description of effect of grain size on yield stress of metals". *Acta Materialia,* **49**(13), pp. 2567–2582.

[124] Wei, Y., and Anand, L., 2004. "Grain-boundary sliding and separation in polycrystalline metals: application to nanocrystalline fcc metals". *Journal of the Mechanics and Physics of Solids,* **52**(11), pp. 2587–2616.

[125] Van Swygenhoven, H., Spaczer, M., and Caro, A., 1999. "Microscopic description of plasticity in computer generated metallic nanophase samples: A comparison between Cu and Ni". *Acta Materialia,* **47**(10), pp. 3117–3126.

[126] Van Swygenhoven, H., Caro, A., and Farkas, D., 2001. "A molecular dynamics study of polycrystalline fcc metals at the nanoscale: grain boundary structure and its influence on plastic deformation". *Materials Science and Engineering A - Structural Materials - Properties, Microstructure and Processing,* **309**, pp. 440–444.

[127] Van Swygenhoven, H., Caro, A., and Farkas, D., 2001. "Grain boundary structure and its influence on plastic deformation of polycrystalline FCC metals at the nanoscale: A molecular dynamics study". *Scripta Materialia,* **44**(8-9), pp. 1513–1516.

[128] Derlet, P., Hasnaoui, A., and Van Swygenhoven, H., 2003. "Atomistic simulations as guidance to experiments". *Scripta Materialia,* **49**(7), pp. 629–635.

[129] Hasnaoui, A., Derlet, P., and Van Swygenhoven, H., 2004. "Interaction between dislocations and grain boundaries under an indenter - a molecular dynamics simulation". *Acta Materialia,* **52**(8), pp. 2251–2258.

[130] Kim, H., Estrin, Y., and Bush, M., 2000. "Plastic deformation behaviour of fine-grained materials". *Acta Materialia,* **48**(2), pp. 493–504.

[131] Zhou, J., Li, Y., Zhu, R., and Zhang, Z., 2007. "The grain size and porosity dependent elastic moduli and yield strength of nanocrystalline ceramics". *Materials Science and Engineering A - Structural Materials - Properties, Microstructure and Processing,* **445**, pp. 717–724.

[132] Budianski,B., 1970. "Thermal and Thermoelastic Properties of Isotropic Composites". *Journal of Composite Materials,* **4**, pp. 286–295.

[133] Tadmor, E., Phillips, R., and Ortiz, M., 1996. "Mixed atomistic and continuum models of deformation in solids". *Langmuir,* **12**(19), pp. 4529–4534.

[134] Tadmor, E., Ortiz, M., and Phillips, R., 1996. "Quasicontinuum analysis of defects in solids". *Philosophical Magazine A - Physics of Condensed Matter Structure, Defects and Mechanical Properties,* **73**(6), pp. 1529–1563.

[135] Shenoy, V., Miller, R., Tadmor, E., Phillips, R., and Ortiz, M., 1998. "Quasicontinuum models of interfacial structure and deformation". *Physical Review Letters,* **80**(4), pp. 742–745.

[136] Shenoy, V., Miller, R., Tadmor, E., Rodney, D., Phillips, R., and Ortiz, M., 1999. "An adaptive finite element approach to atomic-scale mechanics - the quasicontinuum method". *Journal of the Mechanics and Physics of Solids,* **47**(3), pp. 611–642.

[137] Sansoz, F., and Molinari, J., 2004. "Incidence of atom shuffling on the shear and decohesion behavior of a symmetric tilt grain boundary in copper". *Scripta Materialia,* **50**(10), pp. 1283–1288.

[138] Bardenhagen, S., and Kober, E., 2004. "The generalized interpolation material point method". *CMES-Computer Modeling in Engineering& Sciences,* **5**(6), pp. 477–495.

[139] Lu, H., Daphalapurkar, N., Wang, B., Roy, S., and Komanduri, R., 2006. "Multiscale simulation from atomistic to continuum-coupling molecular dynamics (MD) with the material point method (MPM)". *Philosophical Magazine,* **86**(20), pp. 2971–2994.

[140] Ma, J., Liu, Y., Lu, H., and Komanduri, R., 2006. "Multiscale simulation of nanoindentation using the generalized interpolation material point (GIMP)

method, dislocation dynamics (DD) and molecular dynamics (MD)". *CMES-Computer Modeling in Engineering & Sciences,* **16**(1), pp. 41–55.

[141] Tan, H., 2001. "A Lattice Material Point Method that can Adaptively Link Continuum and Atomistic Simulations of Fracture in Nanocomposite Ceramic". *Sixth U.S. National Congress on Computational Mechanics.*

[142] Daphalapurkar, N., 2002. "Multiscale Simulation from Atomistic to Continuum – Coupling Molecular Dynamics (MD) with Material Point Method (MPM)". *Oklahoma State University - MS Thesis.*

[143] BOOTS, B., 1982. "The Arrangement of Cells in Random Networks". *Metallography,* **15**(1), pp. 53–62.

[144] Sfantos, G., and Aliabadi, M., 2007. "A boundary cohesive grain element formulation for modelling intergranular microfracture in polycrystalline brittle materials". *International Journal for Numerical Methods in Engieering,* **69**(8), pp. 1590–1626.

[145] Fu, H., Benson, D., and Meyers, M., 2004. "Computational description of nanocrystalline deformation based on crystal plasticity". *Acta Materialia,* **52**(15), pp. 4413–4425.

[146] Zhang, K., Zhang, D., Feng, R., and Wu, M., 2005. "Microdamage in polycrystalline ceramics under dynamic compression and tension". *Journal of Applied Physics,* **98**(2), p. 023505.

[147] Kumar, S., Kurtz, S., and Agarwala, V., 1996. "Micro-stress distribution within polycrystalline aggregate". *Acta Mechanica,* **114**(1-4), pp. 203–216.

[148] `http://people.scs.fsu.edu/~burkardt/m_src/cvt_demo/cvt_square_uniform.m`, Internet link retrieved on March 12, 2008.

[149] Du, Q., Faber, V., and Gunzburger, M., 1999. "Centroidal Voronoi tessellations: Applications and algorithms". *SIAM Review,* **41**(4), pp. 637–676.

[150] Munro, R., and Freiman, S., 1999. "Correlation of fracture toughness and strength". *Journal of the American Ceramic Society,* **82**(8), pp. 2246–2248.

[151] Zunjarrao, S. C., Singh, A. K., and Singh, R. P., 2006. "Structe- Property Relationships in Polymer Derived Amorphous/Nano-crystalline Silicon Carbide for Nuclear Applications". *Proceedings of ICONE 14, 14th International Conference On Nuclear Engineering.*

APPENDIX A

Matlab code to generate Voronoi diagram

```
function [p,t] = cvt_square_uniform(n, sample_num, delaunay_display)
%% CVT_SQUARE_UNIFORM demonstrates how a CVT
%    can be computed and displayed in MATLAB.
%     Discussion:
%    This simple example carries out an iterative CVT calculation
% in the  unit square, with a uniform density.
% The initial placement of the generators is random.
%
%  Modified:
%    22 May 2006
%  Author:
%    John Burkardt
% Source:
%     http://people.scs.fsu.edu/~burkardt/m_src/cvt_demo/cvt_square_uniform.m
%  Reference:
%    Qiang Du, Vance Faber, Max Gunzburger,
%    Centroidal Voronoi Tessellations: Applications and Algorithms,
%    SIAM Review,
%    Volume 41, 1999, pages 637-676.
%
%  Parameters:
%% Input, integer N, the number of generators.
%% Input, integer SAMPLE_NUM, the number of sample points.
%%  Input, logical DELAUNAY_DISPLAY, is TRUE (nonzero) if the
% Delaunay triangulation is to be displayed.
%%  Output, real P(N,2), the location of the generators.
%%  Output, integer T(NT,3), information defining the Delaunay
%     triangulation of the generators.  NT is the number of triangles,
%     which varies depending on the arrangement of the generators.
%
  fprintf ( 1, '\n' );
```

```
fprintf ( 1, 'CVT_SQUARE_UNIFORM:\n' );
fprintf ( 1, ' A simple demonstration of a CVT computation\n' );
fprintf ( 1, ' (Centroidal Voronoi Tessellation)\n' );
fprintf ( 1, ' in a square, with a uniform density.\n' );


if ( nargin < 1 )
  n =5;
  fprintf ( 1, '\n' );
  fprintf ( 1, 'CVT_SQUARE_UNIFORM - Note:\n' );
  fprintf ( 1, ' No value of N was supplied.\n' );
  fprintf ( 1, ' N is the number of generators.\n' );
  fprintf ( 1, ' A default value N = %d will be used.\n', n );
else
  fprintf ( 1, '\n' );
  fprintf ( 1, ' User specified number of generators = %d\n',  n );
end


if ( nargin < 2 )
  sample_num = 1000 * n;
  fprintf ( 1, '\n' );
  fprintf ( 1, 'CVT_SQUARE_UNIFORM - Note:\n' );
  fprintf ( 1, ' No value of SAMPLE_NUM was supplied.\n' );
  fprintf ( 1, ' SAMPLE_NUM is the number of sample points.\n' );
  fprintf ( 1, ' A default value SAMPLE_NUM = %d will be used.\n', ..
    sample_num );
else
  fprintf ( 1, '\n' );
  fprintf ( 1, ' User specified number of sample points = %d\n', ..
    sample_num );
end


if ( nargin < 3 )
  delaunay_display = 0;
  fprintf ( 1, '\n' );
  fprintf ( 1, 'CVT_SQUARE_UNIFORM - Note:\n' );
  fprintf ( 1, ' No value of DELAUNAY_DISPLAY was supplied.\n' );
  fprintf ( 1, ' DELAUNAY_DISPLAY is TRUE (nonzero) if the\n' );
  fprintf ( 1, ' Delaunay triangulation is also to be displayed.\n' );
  fprintf ( 1, ' A default value DELAUNAY_DISPLAY = %d will be used.\n', ..
    delaunay_display );
else
```

```
    fprintf ( 1, '\n' );

    fprintf ( 1, '  User specified DELAUNAY_DISPLAY = %d\n', ...
      delaunay_display );

  end
%
%  This switch is set to 1 (TRUE) if the ACCUMARRAY command is
%   available. That speeds up the calculation a lot.
%  If you don't have the ACCUMARRAY command, just set this to 0.
%
  fprintf ( 1, '\n' );
  fprintf ( 1, 'CVT_SQUARE_UNIFORM:\n' );
  fprintf ( 1, '  MATLAB''s ACCUMARRAY command can be used for faster\n' );
  fprintf ( 1, '  computation.  This command is not available in\n' );
  fprintf ( 1, '  some versions of MATLAB.  If ACCUMARRAY is available,\n' );
  fprintf ( 1, '  simply make sure that the ACCUMARAY_AVAILABLE variable\n' );
  fprintf ( 1, '  is set to 1!\n' );

  accumarray_available = 1;

  if ( accumarray_available )
    fprintf ( 1, '\n' );
    fprintf ( 1, '  The ACCUMARRAY command will be used.\n' );
  else
    fprintf ( 1, '\n' );
    fprintf ( 1, '  The ACCUMARRAY command will NOT be used.\n' );
  end
%
%  Clear the figure screen, if already open.
%
  clf
%
%  Randomize the initial locations of the generators
%  in the unit square. If another region is used,
%  then this initialization should be changed.
%
  p = rand ( n, 2 );

  it = 0;

  while ( 1 )
%
```

```
%  Compute the Delaunay triangle information
%  T for the current nodes.
%
   t = delaunay ( p(:,1), p(:,2) );
%
%  Display the Delaunay triangulation, if requested.
%
   if ( delaunay_display )
     subplot ( 1, 2, 2 )
     trimesh ( t, p(:,1), p(:,2), zeros(n,1) )
     axis ( [ -0.1, 1.1, -0.1, 1.1 ] )
     line ( [ 0.0, 1.0, 1.0, 0.0, 0.0 ], [ 0.0, 0.0, 1.0, 1.0, 0.0 ], ...
       'Color', 'r' );
     title_string = sprintf ( 'Delaunay, step %d', it );
     title ( title_string );
     axis equal
     view ( 2 )
   end
%
%  Display the CVT generators, and the associated Voronoi diagram.
%
   if ( delaunay_display )
     subplot ( 1, 2, 1 )
   end

   voronoi ( p(:,1), p(:,2), t );
   axis ( [ -0.1, 1.1, -0.1, 1.1 ] )
   line ( [ 0.0, 1.0, 1.0, 0.0, 0.0 ], [ 0.0, 0.0, 1.0, 1.0, 0.0 ], ...
     'Color', 'r' );
   title_string = sprintf ( 'Voronoi, step %d', it );
   title ( title_string );
   axis equal
   drawnow
%
%  Generate sample points.
%
%  These sample points implicitly define the geometry of the region.
%  If the region is not a unit square, then the range of the sample
%  data must be changed.
%
%  The data is sampled uniformly.  If a nonuniform density is desired,
```

```
%  then the sampling must be done in a biased way.
%
    xs = rand ( sample_num, 1 );
    ys = rand ( sample_num, 1 );
%
%  For each sample point, find K, the index of the nearest generator.
%  We do this efficiently by using the Delaunay information with
%  Matlab's DSEARCH command, rather than a brute force nearest neighbor
%  computation.
%
    k(1:sample_num,1) = dsearch ( p(:,1), p(:,2), t, xs, ys );
%
%  The centroid of the Voronoi region associated with each generator
%  is approximated by the average of the sample points it was closest to.
%
    if ( accumarray_available )

      count(1:n) = accumarray ( k, ones(sample_num,1) );
      centroid(1,1:n) = accumarray ( k, xs );
      centroid(2,1:n) = accumarray ( k, ys );

    else

      count(1:n) = 0;
      centroid(1,1:n) = 0;
      centroid(2,1:n) = 0;

      for i = 1 : sample_num
        j = k(i);
        count(j) = count(j) + 1;
        centroid(1,j) = centroid(1,j) + xs(i);
        centroid(2,j) = centroid(2,j) + ys(i);
      end

    end
%
%  Replace the generators by the centroids.
%
    p(1:n,1) = ( centroid(1,1:n) ./ count(1:n) )';
    p(1:n,2) = ( centroid(2,1:n) ./ count(1:n) )';
```

```
    string = input ( 'RETURN, or Q to quit: ', 's' );

  if ( string == 'q' | string == 'Q' )
      [vx,vy] = voronoi ( p(:,1), p(:,2), t )
      break
  end


  it = it + 1;


end


fprintf ( 1, '\n' );
fprintf ( 1, 'CVT_SQUARE_UNIFORM:\n' );
fprintf ( 1, '  Normal end of execution.\n' );
```

APPENDIX B

Code in C to create grains from seeds and vertices of voronoi diagram

```c
#include<stdio.h>
#include<math.h>
#include<stdlib.h>


// ******************VARIABLES USED*********************
// (x1, y1), (x2, y2): start and end coordinates of the edges
// (px, py): coordinates of seed points
// ne: total number of edges
// ng: total number of grains
// xl, xu, yl, yu: lower and upper limits of the region in x and y directions respectively
// nge: number of edges of a grain having coordinate (px,py)
// slp: sloape of a line joining a vertex and the respective seed point
// eps: cutoff = 0.000001 because of the float
// dist: disance between two points
// th: angle between two lines
// xgrarr, ygrarr: coordinates of all vertices in the required order
// fp: file pointer for input file, here it is input.txt
// ft: file pointer for output file, here it is output.txt
// *******************************************************



main(){
  float x1[1000], x2[1000], y1[1000], y2[1000], slp, xu, xl, yu, yl;
  float x3[1000], y3[1000], px[1000], py[1000], xv[1000], yv[1000];
  float eps = 0.000001, dist[1000], temp, xgr[1000], ygr[1000];
  float xgrarr[1000], ygrarr[1000], th[1000], xgr2[1000], ygr2[1000];
  int ne, ng, i, j, m1=0, m2=0, k, m, nge[1000], count=0, count2 = 0;
  FILE *fp, *ft;


  // Read input from file "input.txt"


  fp = fopen("input.txt", "r");
```

```c
    fscanf(fp, "%d %d %f %f %f %f", &ne, &ng, &xl, &xu, &yl, &yu);
    for(i = 0; i<ne; i++)
        fscanf(fp, "%f", &x1[i]);
    for(i = 0; i<ne; i++)
        fscanf(fp, "%f", &x2[i]);
    for(i = 0; i<ne; i++)
        fscanf(fp, "%f", &y1[i]);
    for(i = 0; i<ne; i++)
        fscanf(fp, "%f", &y2[i]);
    for (i=0; i<ng; i++)
        fscanf(fp, "%f %f %d", &px[i], &py[i], &nge[i]);
    fclose(fp);


    // Check if the lines are inside the required region
    // bounded by x1, xu, yl and yu.  If lines are outside
    // then discarding them.

    for (i=0; i<ne; i++){
        m1 = 0;
        m2 = 0;
        if(x1[i] < xl) m1 = 1;
        else if(x1[i] > xu) m1 = 1;
        else if(y1[i] < yl) m1 = 1;
        else if(y1[i] > yu) m1 = 1;
        if (x2[i] < xl) m2 = 1;
        else if (x2[i] > xu) m2 = 1;
        else if (y2[i] < yl) m2 = 1;
        else if (y2[i] > yu) m2 = 1;
        if (m1 && m2){
            for (j=i; j<ne-1; j++){
x1[j] = x1[j+1];
x2[j] = x2[j+1];
y1[j] = y1[j+1];
y2[j] = y2[j+1];
            }
            ne = ne-1;
            i--;
        }
    }


    // Take the intercept of the lines which are partially inside
```

```
// the bounded region with the boundary of the region. Discard
// that part of the lines which are falling outside the boundary.


 for(i = 0; i<ne; i++){
   slp = (y2[i] - y1[i])/(x2[i] - x1[i]);
  if (x1[i] < xl) {
    x1[i] = xl;
    y1[i] = y2[i] - slp*x2[i];
  }
  else if (x1[i] > xu){
    x1[i] = xu;
    y1[i] = y2[i] + slp*(x1[i] - x2[i]);
  }
  if (y1[i] < yl) {
    y1[i] = yl;
    x1[i] = x2[i] - y2[i]/slp;
  }
  else if (y1[i] > yu){
    y1[i] = yu;
    x1[i] = x2[i] + (y1[i] - y2[i])/slp;
  }
  if (x2[i] < xl) {
    x2[i] = xl;
    y2[i] = y1[i] - slp*x1[i];
  }
  else if (x2[i] > xu){
    x2[i] = xu;
    y2[i] = y1[i] + slp*(x2[i] - x1[i]);
  }
  if (y2[i] < yl) {
    y2[i] = yl;
    x2[i] = x1[i] - y1[i]/slp;
  }
  else if (y2[i] > yu){
    y2[i] = yu;
    x2[i] = x1[i] + (y2[i] - y1[i])/slp;
  }
  }


 // Grain formation starts from here.
```

```
    for (i=0; i<ne; i++){
      x3[i] = x2[i];
      y3[i] = y2[i];
      x2[i] = x1[i];
      y2[i] = y1[i];
    }
    k = 0;
    for (i=0; i<ne; i++){
      xv[k] = x2[i];
      yv[k] = y2[i];
      k++;
      xv[k] = x3[i];
      yv[k] = y3[i];
      k++;
    }
    for (i=0; i<k; i++){
      for (j=i+1; j<k; j++){
        if((fabs(xv[i]-xv[j]) < eps) && (fabs(yv[i]-yv[j]) < eps)){
for (m=j; m<(k-1); m++){
  xv[m] = xv[m+1];
  yv[m] = yv[m+1];
}
j = j-1;
k = k-1;
        }
      }
    }
    xv[k] = xl;
    yv[k] = yl;
    xv[k+1] = xu;
    yv[k+1] = yl;
    xv[k+2] = xu;
    yv[k+2] = yu;
    xv[k+3] = xl;
    yv[k+3] =yu;
    k = k+4;

    for (i=0; i<1000; i++){
        dist[i] = 0.00000000;
        xgrarr[i] = 0.0000000;
        ygrarr[i] = 0.0000000;
```

```
        th[i] = 0.0000000;

        xgr2[i] = 0.0000000;

        ygr2[i] = 0.0000000;

    }


    // Calculate distance of all vertices from all seed points

    // and arrange in accending order. This will help to find

    // vertices sorrounding the respective seed points


    for (i=0; i<ng; i++){

      for (j=0; j<k; j++)

        dist[j] = sqrt((px[i] - xv[j])*(px[i] - xv[j]) + (py[i] - yv[j])*(py[i] - yv[j]));

      for (j=0; j<k-1; j++){

        for (m=0; m<k-1-j; m++){

if(dist[m+1] < dist[m]){

  temp = dist[m];

  dist[m] = dist[m+1];

  dist[m+1] = temp;

  temp = xv[m];

  xv[m] = xv[m+1];

  xv[m+1] = temp;

  temp = yv[m];

  yv[m] = yv[m+1];

  yv[m+1] = temp;

}

        }

      }

      for (j=0; j<nge[i]; j++){

        xgr[count] = xv[j];

        ygr[count] = yv[j];

        count++;

      }

    }


    // Now we have all vertices of a grain together but they are

    // not in any order (clockwise/counterclockwise). So calculate

    // the angle between line joining the seed point and corresponding

    // vertices and the x-direction. Then according to these angles

    // arrange the vertices in clockwise manner.


    count = 0;
```

```c
  count2 = 0;
  for (i=0; i<ng; i++){
    for (j=0; j<nge[i]; j++){
      th[j] = atan(fabs(py[i]-ygr[count])/fabs(px[i]-xgr[count]));
      if((xgr[count] > px[i]) && (ygr[count] > py[i]))
th[j] = th[j];
      else if((xgr[count] < px[i]) && (ygr[count] > py[i]))
th[j] = 3.141593 - th[j];
      else if((xgr[count] < px[i]) && (ygr[count] < py[i]))
th[j] = th[j] + 3.141593;
      else if((xgr[count] > px[i]) && (ygr[count] < py[i]))
th[j] = 2.0*3.141593 - th[j];
      xgr2[j] = xgr[count];
      ygr2[j] = ygr[count];
      count++;
    }


    for (j=0; j<nge[i]-1; j++){
      for (m=0; m<nge[i]-1-j; m++){
if(th[m+1] < th[m]){
  temp = th[m];
  th[m] = th[m+1];
  th[m+1] = temp;
  temp = xgr2[m];
  xgr2[m] = xgr2[m+1];
  xgr2[m+1] = temp;
  temp = ygr2[m];
  ygr2[m] = ygr2[m+1];
  ygr2[m+1] = temp;
}
      }
    }
    for (j=0; j<nge[i]; j++){
      xgrarr[count2] = xgr2[j];
      ygrarr[count2] = ygr2[j];
      count2++;
    }
    xgrarr[count2] = xgr2[0];
    ygrarr[count2] = ygr2[0];
    count2++;
  }
```

```c
    // Write the arranged vertices in the file output.txt


    fp = fopen("output.txt", "w");

    ft = fopen("output_Excel.txt", "w");

    m = 0;

    m1 = 0;

    for (i=0; i<ng; i++){

      for (j=0; j<=nge[i]; j++){

        fprintf(ft, "%f\t%f\n", xgrarr[m1], ygrarr[m1]);

        m1++;

      }

      fprintf(ft, "\n\n");

      }

    fprintf(fp, "%d\tr\t%f\t%f\t%f\t%f\n\n", ng, xl, xu, yl, yu);

    for (i=0; i<ng; i++){

      fprintf(fp, "%d\n", nge[i]);

      for (j=0; j<=nge[i]; j++){

        fprintf(fp, "%f\t%f\n", xgrarr[m], ygrarr[m]);

        m++;

      }

      fprintf(fp, "\n\n");

      }


    fprintf(fp, "\n\n\n");

    for(i=0; i<ng; i++){

      fprintf(fp, "%f\t%f\n", px[i], py[i]);

    }


    fclose(fp);


}
```

APPENDIX C

Code in C to apply isotropic compression to Voronoi grains and calculate crystalline volume fraction

```c
#include<stdio.h>
#include<math.h>
#include<stdlib.h>


// ******************VARIABLES USED*********************
// (x, y):coordinates of all vertices
// (px, py): coordinates of seed points
// r: factor by which each vertices of the grains need to be compressed
// n: total number of grains
// xl, xu, yl, yu: lower and upper limits of the region in x and y directions respectively
// eps: cutoff = 0.000001 because of the float
// th: angle between two lines
// fp: file pointer for input and output files
// *******************************************************


main(){
  float x[1000], y[1000], px[1000], py[1000], xu, xl, yu, yl, r, R, th, eps = 0.000001;
  float area = 0.0, s, a, b, c, trix[3], triy[3];
  int n, fc[1000], i, j, k=0;
  FILE *fp;


  // Read all the input from file input.txt in the required format


  fp = fopen("input.txt","r");
  fscanf(fp, "%d %f %f %f %f %f", &n, &r, &xl, &xu, &yl, &yu);
  for(i=0; i<n; i++){
    fscanf(fp, "%d", &fc[i]);
    for(j=0; j<=fc[i]; j++){
      k = k + 1;
      fscanf(fp, "%f %f", &x[k-1], &y[k-1]);
    }
```

```
  }
  k = 0;
  for(i=0; i<n; i++)
    fscanf(fp, "%f %f", &px[i], &py[i]);
  fclose(fp);


  // Translate all the vertices of the respective grains towards the seed point
  // by the amount r.


  for(i=0; i<n; i++){
    for(j=0; j<=fc[i]; j++){
      k = k + 1;
      if(((fabs(x[k-1] - xl) < eps) && (fabs(y[k-1] - yl) < eps)));
      else if(((fabs(x[k-1] - xu) < eps) && (fabs(y[k-1] - yl) < eps)));
      else if(((fabs(x[k-1] - xu) < eps) && (fabs(y[k-1] - yu) < eps)));
      else if(((fabs(x[k-1] - xl) < eps) && (fabs(y[k-1] - yu) < eps)));
      else if((fabs(y[k-1] - yl) < eps) || (fabs(y[k-1] - yu) < eps)) {
if(x[k-1] > px[i])
  x[k-1] = x[k-1] - r;
else
  x[k-1] = x[k-1] + r;
      }
      else if((fabs(x[k-1] - xl) < eps) || (fabs(x[k-1] - xu) < eps)) {
if(y[k-1] > py[i])
  y[k-1] = y[k-1] - r;
else
  y[k-1] = y[k-1] + r;
      }
      else {
if((x[k-1] > px[i]) && (y[k-1] > py[i])){
  th = atanf((y[k-1] - py[i])/(x[k-1] - px[i]));
  x[k-1] = x[k-1] - r*cosf(th);
  y[k-1] = y[k-1] - r*sinf(th);
}
else if((x[k-1] < px[i]) && (y[k-1] > py[i])){
  th = atanf((y[k-1] - py[i])/(px[i] - x[k-1]));
  x[k-1] = x[k-1] + r*cosf(th);
  y[k-1] = y[k-1] - r*sinf(th);
}
else if((x[k-1] < px[i]) && (y[k-1] < py[i])){
  th = atanf((py[i] - y[k-1])/(px[i] - x[k-1]));
```

```c
    x[k-1] = x[k-1] + r*cosf(th);

    y[k-1] = y[k-1] + r*sinf(th);

}

else if((x[k-1] > px[i]) && (y[k-1] < py[i])){

    th = atanf((py[i] - y[k-1])/(x[k-1] - px[i]));

    x[k-1] = x[k-1] - r*cosf(th);

    y[k-1] = y[k-1] + r*sinf(th);

}
      }
    }
  }
  k = 0;


  // Calculate the area of all grains by joining all the vertices to
  // the respective seed points and evaluating the area of the triangles

  for(i=0; i<n; i++){
    trix[0] = px[i];
    triy[0] = py[i];
    for(j=0; j<fc[i]; j++){
      trix[1] = x[k];
      triy[1] = y[k];
      trix[2] = x[k+1];
      triy[2] = y[k+1];
      k = k+1;
      area = area + 0.5 * fabs((trix[2]*triy[0] - trix[0]*triy[2]) + (trix[1]*triy[2] - trix[2]*triy[1])
      + (trix[0]*triy[1] - trix[1]*triy[0]));
    }
    k = k+1;
  }


  k = 0;


  // Write the output in the required format in the file output.txt
  fp = fopen("output.txt", "w");
  for(i=0; i<n; i++){
    for(j=0; j<=fc[i]; j++){
      k = k+1;
      fprintf(fp, "%f, %f\n", x[k-1], y[k-1]);
    }
    fprintf(fp, "\n\n");
```

```
    }
    fprintf(fp, "Area of the Crystalline phase = %f\n", area);
    fprintf(fp, "Area of the Amorphous phase = %f\n", 1.0-area);
    fclose(fp);
}
```

APPENDIX D

Sample PYTHON code to create a model in ABAQUS with 1 grain and 1 grain boundary, developed as individual parts

```
'''
--------------------------------------------------------------------------
 Sample PYTHON code that creates 1 grains and 1 grain boundary using the coordinates
 included in the code. To create multiple grains (say, N) the same command given below must be
 repeated  N times with coordinates of each grain included. In addition the code for c
 reating the grain boundary must be repeated for N times with corresponding coordinates
 to create N grain boundary regions around N grains, respectively.
 At the end, instances are created for each grain and grain boundary.
--------------------------------------------------------------------------
'''
from abaqus import *
import testUtils
testUtils.setBackwardCompatibility()
from abaqusConstants import *

import part, material, section, assembly, step, interaction
import regionToolset, displayGroupMdbToolset as dgm, mesh, load, job
#--------------------------------------------------------------------------
# Create a model
Mdb()
modelName = 'PC_10g_88_12'
myModel = mdb.Model(name=modelName)
# Create a new viewport in which to display the model
# and the results of the analysis.
myViewport = session.Viewport(name=modelName)
myViewport.makeCurrent()
myViewport.maximize()
#-------------------------------------------------------------------------
# Create 1 grain
# Create a sketch for the base feature
#-----------------------------------------
```

```
mySketch = myModel.ConstrainedSketch(name='Sketch 1', sheetSize=1)

xyg1 = ((0.012249, 0.311764),

(0.297288, 0.294469),

(0.314673, 0.012124),

(0.012698, 0.012042),

(0.012249, 0.311764))

for i in range(len(xyg1)-1):

mySketch.Line(point1=xyg1[i],

point2=xyg1[i+1])

myPart = myModel.Part(name='grain1', dimensionality=TWO_D_PLANAR, type=DEFORMABLE_BODY)

myPart.BaseShell(sketch=mySketch)

mySketch.unsetPrimaryObject()


#----------------------------------------

#The above set must be repeated N times with corresponding coordinates to generate N grains.

#----------------------------------------


### END OF GRAINS, NOW TO CREATE GRAIN BOUNDARIES ------------------------------------------

# Create a sketch for the base feature

#----------------------------------------

mySketch = myModel.ConstrainedSketch(name='Sketch 11', sheetSize=1)

xyCoordsInner = ((0.012249, 0.311764),

(0.297288, 0.294469),

(0.314673, 0.012124),

(0.012698, 0.012042),

(0.012249, 0.311764))

xyCoordsOuter = ((0.000000, 0.324263),

(0.309400, 0.307100),

(0.327293, 0.000000),

(0.000000, 0.000000),

(0.000000, 0.324263))

for i in range(len(xyCoordsInner)-1):

mySketch.Line(point1=xyCoordsInner[i],

point2=xyCoordsInner[i+1])

for i in range(len(xyCoordsOuter)-1):

mySketch.Line(point1=xyCoordsOuter[i],

point2=xyCoordsOuter[i+1])

myPart = myModel.Part(name='GB1', dimensionality=TWO_D_PLANAR, type=DEFORMABLE_BODY)

myPart.BaseShell(sketch=mySketch)

mySketch.unsetPrimaryObject()

#----------------------------------------
```

```
#The above set must be repeated N times with corresponding coordinates to generate N grains.

#----------------------------------------


# Creating Instances. This will put all parts in one assembly

a = mdb.models['PC_10g_88_12'].rootAssembly


p = mdb.models['PC_10g_88_12'].parts['grain1']

a.Instance(name='grain10', part=p, dependent=OFF)


p = mdb.models['PC_10g_88_12'].parts['GB1']

a.Instance(name='GB1', part=p, dependent=OFF)


#----------------------------------------

#The above set must be repeated 2N times with corresponding names for N grains + N grain boundaries.

#----------------------------------------
```

APPENDIX E

Sample PYTHON code to create a 2 dimensional model in ABAQUS as single part with 10 grains in a unit square

```
,,,
---------------------------------------------------------------------------
 Sample PYTHON code that creates a 2 dimensional single part with (10) grains drawn in a unit square
 using coordinates for vertices of the grains included in the code.
 --------------------------------------------------------------------------
,,,
from abaqus import *
import testUtils
testUtils.setBackwardCompatibility()
from abaqusConstants import *
import part, material, section, assembly, step, interaction, partition
import regionToolset, displayGroupMdbToolset as dgm, mesh, load, job
#---------------------------------------------------------------------------
# Create a model
Mdb()
modelName = 'Model-1'
myModel = mdb.Model(name=modelName)


# Create a new viewport in which to display the model
# and the results of the analysis.


myViewport = session.Viewport(name=modelName)
myViewport.makeCurrent()
myViewport.maximize()
#---------------------------------------------------------------------------
# Create a sketch for the base feature
s1 = myModel.ConstrainedSketch(name='Sketch 1', sheetSize=1)
xyg1 = ((0.000000, 0),
(0,1),
(1, 1),
(1, 0),
```

```
(0, 0))
for i in range(len(xyg1)-1):
    s1.Line(point1=xyg1[i],
        point2=xyg1[i+1])
myPart = myModel.Part(name='Part-1', dimensionality=TWO_D_PLANAR, type=DEFORMABLE_BODY)
myPart.BaseShell(sketch=s1)
s1.unsetPrimaryObject()
#---------------------------------------------------------------------------
p = mdb.models['Model-1'].parts['Part-1']
session.viewports['Viewport: 1'].setValues(displayedObject=p)
p = mdb.models['Model-1'].parts['Part-1']
f, e, d1 = p.faces, p.edges, p.datums
g, v, d, c = s1.geometry, s1.vertices, s1.dimensions, s1.constraints


s1.setPrimaryObject(option=SUPERIMPOSE)
p = mdb.models['Model-1'].parts['Part-1']
p.projectReferencesOntoSketch(sketch=s1, filter=COPLANAR_EDGES)


s1.Line(point1=(0.000000, 0.294263),point2=(0.288636, 0.285447))
s1.Line(point1=(0.288636, 0.285447),point2=(0.297293, 0.000000))
s1.Line(point1=(0.297293, 0.000000),point2=(0.000000, 0.000000))
s1.Line(point1=(0.000000, 0.000000),point2=(0.000000, 0.294263))


s1.Line(point1=(0.332539, 0.288006),point2=(0.388058, 0.343339))
s1.Line(point1=(0.388058, 0.343339),point2=(0.625421, 0.256398))
s1.Line(point1=(0.625421, 0.256398),point2=(0.605043, 0.000000))
s1.Line(point1=(0.605043, 0.000000),point2=(0.357293, 0.000000))
s1.Line(point1=(0.357293, 0.000000),point2=(0.332539, 0.288006))


s1.Line(point1=(0.676431, 0.253231),point2=(0.734353, 0.298308))
s1.Line(point1=(0.734353, 0.298308),point2=(1.000000, 0.259342))
s1.Line(point1=(1.000000, 0.259342),point2=(1.000000, 0.000000))
s1.Line(point1=(1.000000, 0.000000),point2=(0.665043, 0.000000))
s1.Line(point1=(0.665043, 0.000000),point2=(0.676431, 0.253231))


s1.Line(point1=(1.000000, 0.319342),point2=(0.740232, 0.345593))
s1.Line(point1=(0.740232, 0.345593),point2=(0.732539, 0.610708))
s1.Line(point1=(0.732539, 0.610708),point2=(1.000000, 0.624524))
s1.Line(point1=(1.000000, 0.624524),point2=(1.000000, 0.319342))


s1.Line(point1=(1.000000, 0.684524),point2=(0.729002, 0.658549))
```

125

```
s1.Line(point1=(0.729002, 0.658549),point2=(0.703045, 0.677030))
s1.Line(point1=(0.703045, 0.677030),point2=(0.670634, 0.775627))
s1.Line(point1=(0.670634, 0.775627),point2=(0.732477, 1.000000))
s1.Line(point1=(0.732477, 1.000000),point2=(1.000000, 1.000000))
s1.Line(point1=(1.000000, 1.000000),point2=(1.000000, 0.684524))


s1.Line(point1=(0.672477, 1.000000),point2=(0.620434, 0.788770))
s1.Line(point1=(0.620434, 0.788770),point2=(0.363382, 0.834907))
s1.Line(point1=(0.363382, 0.834907),point2=(0.324880, 1.000000))
s1.Line(point1=(0.324880, 1.000000),point2=(0.672477, 1.000000))


s1.Line(point1=(0.264880, 1.000000),point2=(0.306807, 0.821665))
s1.Line(point1=(0.306807, 0.821665),point2=(0.246159, 0.682328))
s1.Line(point1=(0.246159, 0.682328),point2=(0.000000, 0.664629))
s1.Line(point1=(0.000000, 0.664629),point2=(0.000000, 1.000000))
s1.Line(point1=(0.000000, 1.000000),point2=(0.264880, 1.000000))


s1.Line(point1=(0.000000, 0.604629),point2=(0.250692, 0.629808))
s1.Line(point1=(0.250692, 0.629808),point2=(0.349551, 0.498825))
s1.Line(point1=(0.349551, 0.498825),point2=(0.348425, 0.384410))
s1.Line(point1=(0.348425, 0.384410),point2=(0.291146, 0.330907))
s1.Line(point1=(0.291146, 0.330907),point2=(0.000000, 0.354263))
s1.Line(point1=(0.000000, 0.354263),point2=(0.000000, 0.604629))


s1.Line(point1=(0.292420, 0.661386),point2=(0.391663, 0.530689))
s1.Line(point1=(0.391663, 0.530689),point2=(0.653171, 0.658824))
s1.Line(point1=(0.653171, 0.658824),point2=(0.614465, 0.755121))
s1.Line(point1=(0.614465, 0.755121),point2=(0.357094, 0.798906))
s1.Line(point1=(0.357094, 0.798906),point2=(0.292420, 0.661386))


s1.Line(point1=(0.408493, 0.496927),point2=(0.668218, 0.628638))
s1.Line(point1=(0.668218, 0.628638),point2=(0.694003, 0.609919))
s1.Line(point1=(0.694003, 0.609919),point2=(0.697305, 0.344709))
s1.Line(point1=(0.697305, 0.344709),point2=(0.640489, 0.298245))
s1.Line(point1=(0.640489, 0.298245),point2=(0.402227, 0.382679))
s1.Line(point1=(0.402227, 0.382679),point2=(0.408493, 0.496927))


p = mdb.models['Model-1'].parts['Part-1']
f = p.faces
pickedFaces = f.getSequenceFromMask(mask=('[#1 ]', ), )
e1, d2 = p.edges, p.datums
```

```
p.PartitionFaceBySketch(faces=pickedFaces, sketch=s1)
s1.unsetPrimaryObject()
```

VITA

Suraj C. Zunjarrao

Candidate for the Degree of

Doctor of Philosophy

Dissertation: Polymer Derived Ceramics: Novel Processing and Structure–Property Relationships

Major Field: Mechanical and Aerospace Engineering

Biographical:

Personal Data: Born in Pune, Maharashtra, India on September 08, 1979.

Education:
Received the B.S. degree from University of Pune, Pune, Maharashtra, India, 2001, in Mechanical Engineering
Received the M.S. degree from State University of New York at Stony Brook, Stony Brook, New York, USA, 2003, in Mechanical Engineering
Completed the requirements for the degree of Doctor of Philosophy with a major in Mechanical and Aerospace Engineering in Oklahoma State University in May, 2008.

Name: Suraj C. Zunjarrao   Date of Degree: May, 2008

Institution: Oklahoma State University   Location: Stillwater, Oklahoma

Title of Study: Polymer Derived Ceramics: Novel Processing and Structure–
                 Property Relationships

Pages in Study: 127   Candidate for the Degree of Doctor of Philosophy

Major Field: Mechanical Engineering

Silicon carbide (SiC) is an important ceramic, most commonly used because of its excellent properties such as high strength, high modulus, excellent creep resistance and its high temperature stability. Moreover, it is attracting wide attention as a promising candidate for several applications in nuclear reactors owing to its high thermal conductivity, high melting temperature, good chemical stability, and resistance to swelling under heavy ion bombardment. However, fabricating SiC by traditional powder processing route generally requires very high temperatures for pressureless sintering. Alternatively, polymer derived ceramic materials offer unique advantages such as ability to fabricate net shaped components, incorporate reinforcements, along with lower processing temperatures and relatively easy control over the microstructure. In this study, fabrication of polymer derived amorphous and nano-grained SiC, by controlled pyrolysis of allylhydridopolycarbosilane (AHPCS) under inert atmosphere, is presented. Final processing temperatures and hold times were varied to study the influence of processing parameters on the structure and resulting properties. Chemical changes, phase transformations and microstructural changes occurring during the pyrolysis process are studied as a function of the processing temperatures. Polymer crosslinking and polymer to ceramic conversion is studied using infrared spectroscopy (FTIR). Thermogravimetric analysis (TGA) and differential thermal analysis (DTA) are performed to monitor the mass loss and phase change as a function of temperature. X-ray diffraction studies are done to study the intermediate phases and microstructural changes. Variation in density is carefully monitored as a function of processing temperature. Hardness and modulus measurements are carried out using instrumented nanoindentation to establish processing–property–structure relationship for SiC derived from the polymer precursor. It is seen that the presence of nanocrystalline domains in amorphous SiC significantly influences the modulus and hardness. A non-linear relationship is observed in these properties with optimal mechanical properties for SiC processed to 1150 °C for 1 hour hold duration, having average grain size of ~ 3 nm. In addition, bulk mechanical characterization, in terms of biaxial flexure strength, was done for SiC–SiC particulate composites purely derived from the polymer precursor. Finally, a simple finite element model is developed for nanocrystalline SiC.

ADVISOR'S APPROVAL: _____